

ACTIVE POWER CONTROL OF PHOTOVOLTAIC SYSTEMS
AND
ELECTRIC VEHICLE CHARGE OPTIMIZATION INCLUDING THE COSTS OF BATTERY
DEGRADATION

by

ANDERSON FOSTER HOKE

B.A., Dartmouth College, 2001

M.S., University of Colorado, 2013

A thesis submitted to the
Faculty of the Graduate School of the
University of Colorado in partial fulfillment
of the requirement for the degree of
Doctor of Philosophy
Department of Electrical, Computer, and Energy Engineering

2016

This thesis entitled:
Active Power Control of Photovoltaic Systems,
and Electric Vehicle Charge Optimization Including the Costs of Battery Degradation
written by Anderson Hoke
has been approved for the Department of Electrical, Computer, and Energy Engineering

Professor Dragan Maksimović

Mariko Shirazi, Ph.D.

Date _____

The final copy of this thesis has been examined by the signatories, and we find that both the content and the form meet acceptable presentation standards of scholarly work in the above mentioned discipline.

Hoke, Anderson Foster (Ph.D., Electrical, Computer, and Energy Engineering)

Active Power Control of Photovoltaic Systems, and
Electric Vehicle Charge Optimization Including the Costs of Battery Degradation

Thesis directed by Professor Dragan Maksimović

Abstract

This thesis consists of two parts. The first describes new methods for use in the active power control of photovoltaic (PV) inverters without the need for energy storage. As increasing numbers of PV power systems are interconnected with the electric power system, those PV systems displace some of the conventional generators that currently balance generation and load and stabilize the grid frequency by modulating their active power output. At very high levels of PV penetration, it may be desired or required that PV generators contribute to the stabilization and regulation of grid frequency by modulating their output power. This work proposes a novel method of estimating the maximum power available from a PV array, allowing an inverter to minimize the opportunity cost of providing any required reserve power for up-regulation. It also proposes a novel method of increasing the speed at which a PV inverter can reach a new power set point in response to a frequency event, which increases the effectiveness of the inverter's active power response. Both of these methods are validated experimentally using a prototype inverter.

The second component of this thesis describes a method for optimizing the charging of electric vehicles taking into account both a time-varying cost of

electricity and the impact of the charge profile on Lithium-ion battery lifetime using a simplified Lithium-ion battery lifetime model. The simple battery lifetime model, also developed and presented here, estimates both energy capacity fade and power fade and includes effects due to temperature, state of charge profile, and daily depth of discharge. Resulting vehicle charge profiles show a compromise among four trends: charging during low-electricity cost intervals, charging slowly, charging towards the end of the available charge time, and suppression of vehicle-to-grid power exportation. Simulations based on experimental Prius PHEV usage data predict that batteries charged using optimized charging last significantly longer than those charged using typical charging methods, potentially allowing smaller batteries to meet vehicle lifetime requirements. These trends are shown to hold across a wide range of battery sizes and hence are applicable to both pure electric vehicles and plug-in hybrid electric vehicles.

Dedication

This thesis is dedicated to my family: Jodie, Benjy, Henry, and Bear. Thank you for your love and patience.

Acknowledgments

First of all, I very gratefully acknowledge the guidance of my advisor, Dragan Maksimovic. His clarity of thought and ability to clearly explain complex topics are inspiring. A heartfelt “thank you” as well to my thesis committee, Bob Erickson, Lucy Pao, Mari Shirazi, and Sudipta Chakraborty, for their guidance and patience.

I would also like to thank Annabelle Pratt for her technical and financial support of the portion of this work dealing with Lithium-ion battery degradation in her former capacity at Intel Labs. Fellow CU Boulder Ph.D. student Alexander Brissette also collaborated on that work.

At the National Renewable Energy Laboratory (NREL), many of my coworkers have supported this work in one way or another, and I am very grateful for that. Sudipta Chakraborty and Mari Shirazi provided the inverter hardware and software on which much of this work was based. Both were also invaluable in helping me get my start at NREL. Ed Muljadi allowed me to conduct some of this research under his NREL project funding. Ed, Vahan Gevorgian, and Erik Ela provided advice and guidance on active power control and grid frequency modeling. Mari Shirazi, Austin Nelson, Pete Gotseff, and Kumaraguru Prabakar each helped troubleshoot or answer questions. Mari, Greg Martin, Mike Simpson, Caroline Elam, Ismael Mendoza, Darin Smith, Nate Mitchell, and Jen Wingard all helped allow me to continue this work at NREL’s Distributed Energy Resource Test Facility well past the day when perhaps it should have been left to the mice. Kandler Smith provided invaluable technical guidance on battery lifetime modeling, as well as the use of his unique battery lifetime predictive model. Others at NREL have also contributed in various ways, and I am sincerely grateful.

Last but not least, the American Public Power Association generously supported portions of this work related to active power control of photovoltaic systems through their Demonstration of Energy and Efficiency Developments scholarship program.

Contents

1	Introduction	1
	Part I: Active power control of photovoltaic systems	3
2	Background and overview of PV active power control (APC).....	4
2.1	Frequency regulation background.....	6
2.2	Potential benefits of APC of PV.....	9
2.3	State of the art of APC of PV.....	10
3	Real-time PV maximum power-point estimation (MPPE)	17
3.1	MPPE method.....	19
3.1.1	Estimating P_{mp} from Irradiance and Temperature	20
3.1.2	Offline Parameter Estimation	23
3.1.3	Effect of irradiance variability.....	28
3.2	Droop control	30
3.3	PV APC simulation.....	31
3.4	MPPE experimental demonstration.....	36
4	Rapid active power of control PV systems	47
4.1	Candidate active power control methods	50
4.2	Rapid APC (RAPC) method	54
4.3	Experimental demonstration of MPPE and rapid APC.....	65
	Part II: Degradation-aware electric vehicle charge optimization.....	77
5	Overview of degradation-aware charging (DAC) of electric vehicle batteries .	78
6	Degradation-aware charging method.....	82
6.1	Simple battery degradation model.....	82
6.1.1	Overview.....	82

6.1.2	Temperature-related degradation: $c_{Q,T}$ and $c_{P,T}$	84
6.1.3	SOC-related degradation: $c_{Q,SOC}$	86
6.1.4	Depth of discharge related degradation: $c_{Q,DOD}$	87
6.1.5	Model tuning and verification.....	88
6.2	Charge optimization algorithm	88
7	Degradation-aware charging results	91
7.1	Optimized charge profiles.....	91
7.2	Battery lifetime comparisons	96
8	Conclusion.....	104
8.1	Contributions	104
8.2	Future work	107
8.2.1	Active power control of PV	107
8.2.2	Degradation-aware battery charging	112
	References	114

List of Tables

Table 1. Solarex 110S PV module data sheet parameters at standard test conditions (STC)	23
Table 2. Regression fit parameters for equation (2) for Solarex PV module example	27
Table 3. Parameters for EPS frequency model	34
Table 4. Baseline frequency transient simulation parameters.....	35
Table 5. Charge profile descriptions	97
Table 6. Comparison of charge optimization methods	101

List of Figures

Figure 1. Inertial, primary and secondary frequency control following a frequency disturbance at time zero. X-axis not to scale. (Adapted from [20].)	6
Figure 2. Sample power-frequency droop output characteristics. Extended from EPRI [25]. Such droop curves could be implemented for PV-based frequency regulation.....	8
Figure 3. Demonstration of a PV plant performing AGC, from [64].	14
Figure 4. Demonstration of a PV plant performing FFR, from [64]......	15
Figure 5. Demonstration of a PV plant performing FFR, expanded time range, from [64].....	16
Figure 6. The power-voltage curve of a PV array illustrating an operating point P_{setPV} below the maximum power point.	19
Figure 7. Flowchart for offline calculation of MPPE parameters in equation (2).	22
Figure 8. The five-parameter model of a PV cell.....	24
Figure 9. Estimating maximum available PV power from measured irradiance and temperature in real time. N is the number of PV modules in the array, η is the conversion efficiency of the PV plant, and the first-order cutoff frequency ω_c is described in Section 3.1.3.....	27
Figure 10. Inverter power-frequency droop controller (without deadband).	31
Figure 11. Line-frequency response model of grid and PV inverter.....	32
Figure 12. Governor and turbine transfer functions for grid dynamic model	33
Figure 13. Left: Baseline frequency transient event: no PV-based primary frequency regulation. Right: Frequency transient event with PV-based primary frequency regulation enabled with 20 MW power reserve.	36
Figure 14. Preliminary experimental validation of the MPPE method. The top two plots show measured irradiance and PV cell temperature. The bottom plot shows the predicted output power and the measured output power of a commercial inverter operating in MPPT mode.....	37
Figure 15. Experimental setup for hardware validation of MPPE method.	39
Figure 16. Experimental setup for hardware validation of MPPE method.	42
Figure 17. The two identical PV arrays used for experimental validation of MPPE and RAPC. One array is in the left foreground, and the second is to the right and slightly behind it. The inverter and test equipment are located in the DERTF building behind the right array.....	43
Figure 18. Demonstration of a prototype inverter operating in MPPE mode with a reserve power of 500 W while a second inverter operates in standard MPPT mode.	44
Figure 19. Prototype inverter operating in MPPE mode with a reserve power of 500 W while a second inverter operates in standard MPPT mode, with measured irradiance and temperature recorded.....	46
Figure 20. Comparison of the MPPE method proposed here to a simpler method of PV maximum power point estimation based on measured irradiance only.	47
Figure 21. The power-voltage curve of a PV array illustrating a single operating point, P_{SET} , and the voltage V_{cmd} need to achieve that operating point. The local slope of the curve at V_{cmd} is also illustrated.....	49
Figure 22. Power-voltage curves of the Solarex 110S PV module as a function of PV cell temperature, at nominal irradiance (1000 W/m^2).....	52
Figure 23. Histogram of residuals (errors between polynomial regression model and actual nonlinear PV model) for the lowest RMS error variant of equation (10).	53
Figure 24. PV power as a function of irradiance and voltage at constant cell temperature (left), and as a function of cell temperature and voltage at constant irradiance (right).	55
Figure 25. PV module voltage needed to produce a desired power (yellow trace), at a fixed cell temperature and irradiance.....	56
Figure 26. Desired lookup table output (red Xs), and PV module voltage-power relationship (blue dots).57	57

Figure 27. Desired lookup table output (red Xs), and PV module voltage-power relationship (blue dots) at very low irradiance.....	58
Figure 28. Process for generating a lookup table for use in rapid active power control of PV systems.	60
Figure 29. Selecting $V_{PV}(P_{PV}, G, T)$ LUT resolution in irradiance dimension. The top plot includes 10 irradiance data points, and the bottom plot contains 50. Both are plotted a constant temperature of 47 °C.	62
Figure 30. Selecting $V_{PV}(P_{PV}, G, T)$ LUT resolution in temperature dimension. The top plot includes 10 temperature data points, and the bottom plot contains 30. Both are plotted a constant irradiance of 843 W/m ²	64
Figure 31. Control overview showing MPPE and lookup table for rapid active power control.	65
Figure 32. Rapid active power control experimental setup.....	66
Figure 33. Response of the prototype inverter to a frequency event with a nadir of 59 Hz and a 2 Hz/s ROCOF.	68
Figure 34. Zoomed in response of the prototype inverter to a frequency event with a nadir of 59 Hz and a 2 Hz/s ROCOF.	69
Figure 35. Response of the prototype inverter to an overfrequency event peaking at 61 Hz with a 2 Hz/s ROCOF.	70
Figure 36. Zoomed in response of the prototype inverter to an overfrequency event peaking at 61 Hz with a 2 Hz/s ROCOF.	71
Figure 37. Response of the prototype inverter to a frequency event with a nadir of 59 Hz and a 6 Hz/s ROCOF.	72
Figure 38. Zoomed in response of the prototype inverter to a frequency event with a nadir of 59 Hz and a very fast 6 Hz/s ROCOF.	73
Figure 39. Response of the prototype inverter to a frequency event with a lower nadir of 58 Hz and a 1 Hz/s ROCOF.	74
Figure 40. Zoomed in response of the prototype inverter to a frequency event with a lower nadir of 58 Hz and a 1 Hz/s ROCOF.	75
Figure 41. EV/PHEV charge optimization diagram. The charge optimization algorithm can be implemented on the controller of the on-board EVSE.	79
Figure 42. Finding energy capacity lifetime, L_Q , from NREL’s model.	84
Figure 43. Optimized charging with constant energy cost.	92
Figure 44. Optimized charging simple two-level energy cost.	93
Figure 45. Optimized charging with historical MIDC price on a typical day.	94
Figure 46. Optimized charging with historical MIDC price showing an unusual spike.	95
Figure 47. Optimized charging showing a small amount of V2G.	96
Figure 48. Weekly SOC profiles for three battery sizes under various charging scenarios.	98
Figure 49. Prius battery lifetime under various charge scenarios.	99
Figure 50. Nineteen kWh battery lifetime under various charge scenarios. Power lifetimes truncated as indicated by arrows.	100
Figure 51. Thirty-five kWh battery lifetime under various charge scenarios. Power lifetimes truncated as indicated by arrows.	100
Figure 52. Histogram of recent frequency events in the U.S. Western Interconnection. While small events are common, larger events become increasingly rare. Annotations on the figure show one possible strategy for providing PV-based frequency event response.....	110

List of Acronyms

AC	Alternating current
ADC	Analog to digital converter
AGC	Automatic generation control
APC	Active power control
CSV	Comma-separated value
DAC	Degradation-aware charging
DC	Direct current
DER	Distributed energy resource
DERTF	Distributed Energy Resource Test Facility
DOD	Depth of discharge
EOL	End of life
EPRI	Electric power research institute
EPS	Electric power system
ERCOT	Electric Reliability Council of Texas
EV	Electric vehicle
EVSE	Electric vehicle service equipment
FERC	Federal Energy Regulatory Commission
FFR	Fast frequency response
FPGA	Field-programmable gate array
I-V	Current-voltage
IGBT	Insulated gate bipolar transistor
ISO	Independent system operator
IEEE	Institute of Electrical and Electronics Engineers
kWh	Kilowatt-hour
Li-ion	Lithium-ion
LUT	Lookup table
MB	Megabyte
MIDC	Mid-Columbia
MOSFET	Metal oxide semiconductor field effect transistor
MPP	Maximum power point
MPPE	Maximum power point estimation
MPPT	Maximum power point tracking
MWh	Megawatt-hour
NCA	Nickel Cobalt Aluminum
NI	National Instruments
NREL	National Renewable Energy Laboratory
P-f	Power-frequency
P-V	Power-voltage
PHEV	Plug-in hybrid electric vehicle
PHIL	Power hardware in the loop
PID	Proportional-integral-derivative
PFR	Primary frequency regulation
PLL	Phase-locked loop

pu	per unit
PV	Photovoltaic
PWM	Pulse-width modulation
RAPC	Rapid active power control
RMS	Root mean square
ROCOF	Rate of change of frequency
ROI	Rest of interconnection
SAE	Society of Automotive Engineers
sbRIO	Single-board RIO
SiC	Silicon carbide
SOC	State of charge
STC	Standard test conditions
U.S.	United States
V2G	Vehicle to grid
VI	Virtual instrument

1 Introduction

This thesis is composed of two parts, both related to the control of active power of distributed energy resources to improve the grid integration of those resources. The first part describes methods for use in controlling the active power of photovoltaic (PV) systems without energy storage to assist with the closely-related tasks of controlling frequency and balancing load and generation on a bulk power system. The second part describes a method of optimizing the charge profile of Lithium-ion (Li-ion) batteries used in electric vehicles (EVs) and plug-in hybrid electric vehicles (PHEVs). The two parts are related in that they both start by acknowledging that energy storage is subject to significant cost considerations and related concerns about the lifetime of storage batteries. In the case of PV active power control (APC), the solution proposed here avoids storage altogether and instead takes advantage of the components already present in a typical grid interactive PV system, with some added sensors, to provide bi-directional, fast, and reliable active power support to the electric power system (EPS). In the case of degradation-aware charging (DAC) of vehicle traction batteries, Li-ion battery lifetime degradation concerns are quantified in an approximate manner and integrated into a battery charging optimization algorithm.

Aside from the commonalities mentioned in the preceding paragraph, Part I and Part II of this thesis are largely independent and can be considered separately.

Part I begins with background material on the applications and motivation for APC of PV systems in Chapter 2. It then introduces two new control methods for use in active power control of PV systems in Chapters 3 and 4. The first control method recognizes that to provide bi-directional APC from a PV system without

storage, the PV system must operate below its maximum power point (MPP), and that there is a significant opportunity cost to doing so. For this reason, and to provide a reliable and accurate power reserve for up-regulation while minimizing opportunity cost, a method of PV maximum power point estimation (MPPE) is proposed in Chapter 3 . Then in Chapter 4, a method for rapidly moving from one power operating point to another is presented. Both Chapter 3 and Chapter 4 include experimental results demonstrating the use of the proposed control methods in a prototype PV inverter connected to a real PV array.

Part II begins by presenting background material and motivation for the charging vehicle traction batteries in a manner that takes into account the effective costs of battery degradation, in Chapter 5. It then presents a methodology for degradation-aware battery charging, including a simplified model for predicting the impact of a given charge profile on the lifetime of a Li-ion battery in Chapter 6. In this DAC methodology, the estimated cost of lifetime degradation and the cost to charge the battery given an electricity cost profile are co-optimized. Simulated charge profiles based on experimental Toyota Prius PHEV driving data are used to evaluate the effectiveness of the charge optimization method in Chapter 7.

Finally, the contributions of this thesis and proposed future work in the development of both PV active power controls and degradation-aware charging are presented in Chapter 8.

Part I: Active power control of photovoltaic systems

2 Background and overview of PV active power control (APC)

Active power control of PV systems is at an early technology readiness level, but it is progressing rapidly and generating increased interest for reasons described here [1].

As the portion of electricity that is produced by solar photovoltaic (PV) systems increases, it is important for PV systems to help provide many of the grid support functions that are traditionally performed by conventional rotating machines. It is becoming standard for PV inverters to be capable of exporting or importing reactive power, to ride through transient voltage and frequency events, and to be capable of curtailing power during times of high grid frequency. While these inverter capabilities allow higher penetration levels of PV onto the grid, they do not address one of the fundamental complaints against PV – its lack of active power dispatchability [2]. Energy storage systems are often proposed as a solution to this problem. However, current storage technologies have much shorter lifetimes than other PV system components. In addition, while battery costs are falling, they have not seen the dramatic reductions that PV modules have [3].

Through APC of PV inverters, it is technically feasible to remove this drawback and replace it with a new asset: distributed, economical, and fast PV-based frequency regulation. Just as the provision of reactive power from distributed resources is currently transforming the way intelligent power grids control voltage

[4], [5], APC of PV has the potential to transform frequency regulation, while also offering power reference tracking and bi-directional ramp-rate control.

Wind power systems, also intermittent, are already required to be capable of APC in some jurisdictions with higher levels of wind on the grid [6]–[12]. As penetration levels of intermittent resources such as wind and PV increase, power from conventional plants is displaced, increasing the frequency regulation burden on the remaining conventional plants. If the intermittent resource itself can reliably provide frequency regulation, higher levels of that resource can be attained without compromising stability. Indeed, frequency stability can potentially be *improved* through inverter-based frequency regulation because it is inherently faster than mechanical governor based regulation. The U.S. Federal Energy Regulatory Commission (FERC) recognized “the inherently greater amount of frequency regulation service being provided by faster-ramping resources,” issuing Orders 755 and 819 requiring transmission operators to compensate fast ramping frequency regulation sources accordingly [13], [14].

Active power control of PV plants will require sacrificing significant energy production by operating below the maximum power point (MPP). While that may seem counter-intuitive, and may indeed be un-economical in many situations, this thesis describes three increasingly common situations when it may be advantageous to do so.

Photovoltaic inverters with full APC capability have not been commercially developed, and related research is in an early stage. This chapter summarizes the theory behind grid frequency regulation (Section 2.1), describes the motivation for and potential applications of APC of PV inverters (Section 2.2), and reviews existing research related to the topic (Section 2.3);

2.1 Frequency regulation background

The fast-varying power output of conventional grid-connected PV systems increases the moment-to-moment mismatch between load and supply, resulting in fluctuations in grid frequency and increasing the need for frequency regulation services [15]–[17]. One benefit of APC-capable PV inverters is that they could provide frequency regulation.

The electric power industry typically considers frequency regulation to consist of two subcategories: *primary* (on the time scale of a few seconds and below), and *secondary* (on time scales ranging from a few seconds to several minutes) [18], [19], as illustrated in Figure 1.

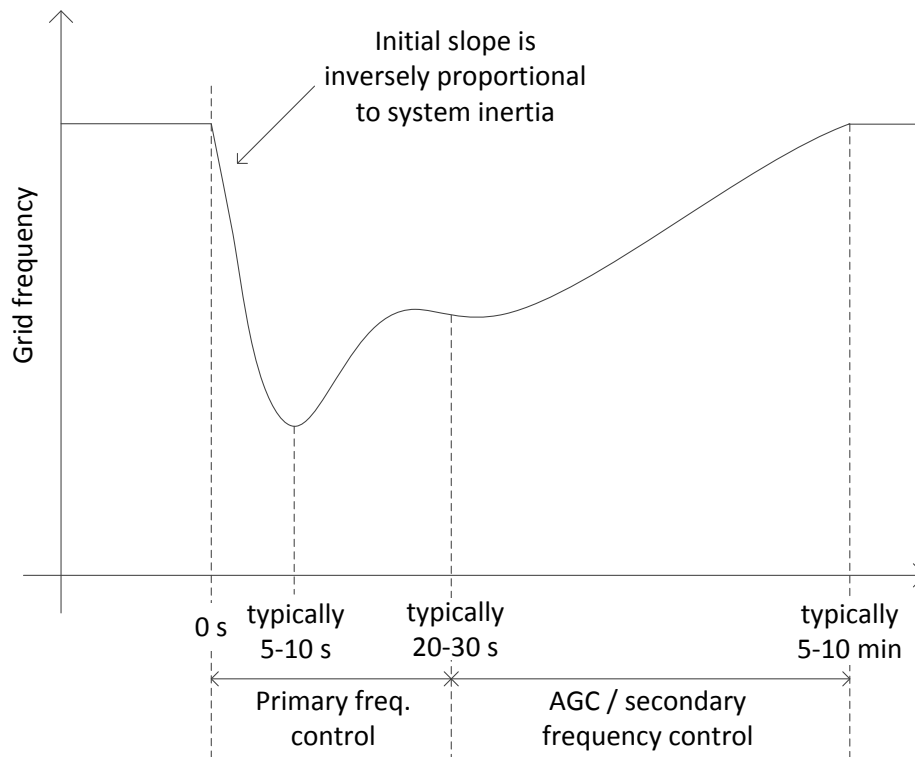


Figure 1. Inertial, primary and secondary frequency control following a frequency disturbance at time zero. X-axis not to scale. (Adapted from [20].)

Primary frequency regulation consists of the inertial response and mechanical governor control of rotating electric generators (or power electronic devices controlled to act like rotating machines). Because inertial response is nearly immediate (occurring on a sub-cycle time scale) it is sometimes considered a category separate from primary response. This distinction is less relevant in relation to inverter-based frequency response because inverter-interfaced sources do not have physical inertia connected to the EPS, and inverter controls respond much faster than mechanical governors [20], [21].

Secondary frequency response is controlled centrally; commands are sent to various generators via an automatic generation control (AGC) signal [18], [19]. The generators adjust their real power setpoints based on the AGC signal, thereby bringing the grid frequency back towards its nominal value. Conventional frequency regulation from rotating machines ramps slowly, responding to AGC signals on a time scale of several minutes [17]. Inverter-based frequency regulation can respond on sub-second time scales, putting it into the valuable category of fast regulation recognized by FERC Order 755.

Fundamental to both primary and secondary frequency response is the concept of power-frequency (P-f) droop, in which generator output power is increased in response to falling grid frequency, and vice-versa [22]–[24]. Because falling frequency is caused by a loss of generation (or increase in load), a droop response acts to re-balance generation and load and stabilize grid frequency. An inverter with a P-f droop output characteristic inherently emulates the frequency response and primary governor control of conventional generators. The inverter can participate in secondary AGC response by adjusting the power set point of its droop

controller. In addition, advanced techniques can be used to adjust droop parameters in real time, improving the speed and accuracy of the droop response. Figure 2(a) shows an example of a simple P-f droop output characteristic for frequency regulation, where P_{set} is the inverter power set point and f_{nom} is the nominal grid frequency. Figure 2(b) shows a P-f characteristic with a dead band and hysteresis, extended from a high-frequency power curtailment specification in [25]. Nonlinear, dynamic, and adaptive droop characteristics can also be employed.

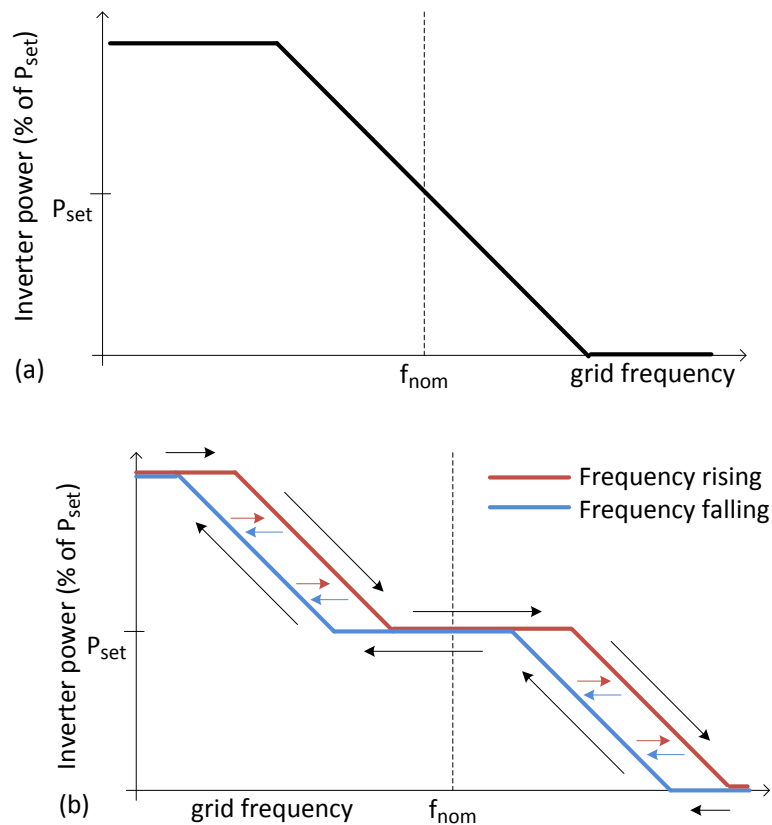


Figure 2. Sample power-frequency droop output characteristics. Extended from EPRI [25]. Such droop curves could be implemented for PV-based frequency regulation.

2.2 Potential benefits of APC of PV

PV-based APC may find application in at least three scenarios:

(1) *Islands:* In remote, island, or islanded microgrid power systems, the variability of renewable generation is particularly problematic since it is not possible to export or import power from neighboring grids [12], [26], [27]. For example, the island of Puerto Rico currently requires new large PV generation facilities to provide primary frequency regulation and controlled power ramp-rates (both up and down) [28]. The PV industry is responding to this requirement by including battery systems with PV plants [29], which significantly increases capital and maintenance costs [3]. Frequency regulation from PV systems can reduce the amount of storage required and/or reduce the cycling of the battery [26], potentially extending its life [30].

(2) *Very high penetration of inverter-coupled generation:* As levels of renewable generation rise, the need for ancillary services including frequency regulation rises even on large national and continental power systems [31]–[34]. As of 2012, Ireland, Canada, Denmark, and Spain have all instituted requirements for some form of frequency regulation from wind [7]–[11]. Many U.S. transmission operators are considering instituting similar rules for wind [35] and eventually for PV [36].

(3) *Regulation markets:* In liberalized electricity markets, whenever the value per MW-hour of frequency regulation exceeds the value of power from a PV plant in MWh, it may make economic sense for privately owned PV plant operators to provide frequency regulation services rather than operating in MPPT (maximum power point tracking) mode. As the need for frequency regulation rises, the value per MW-hour of frequency regulation is expected to rise [37]. In addition, the total value of the market for frequency regulation is expected to rise between 38% and

191% over the coming decade, reaching up to \$56.8 billion per year by 2022 due to economic growth, increases in renewable energy, and electricity market liberalization [34]. Frequency regulation values are currently in the range of \$18 to \$60 per MW-hour in California, New York, and the PJM Interconnection [38], [39]. While this range is below the typical retail cost per MWh of residential electricity, it overlaps with retail commercial and industrial electricity prices, which were \$39.7-\$158.3 per MWh in the continental U.S. in 2011 [40]. Therefore, if regulations and contracts allowed, it may make economic sense at times for commercial and industrial owners of PV systems to bid into frequency regulation markets rather than operating in MPPT mode.

2.3 State of the art of APC of PV

Much current research on APC of PV systems involves incorporating energy storage in the PV plant [41]–[48]. Using storage in stand-alone applications or in conjunction with other generation sources for active power control purposes is also done in the field and treated by researchers [49]–[54]. Controlling a storage inverter’s active power is similar in some ways to controlling a PV inverter’s active power, but is different in that most storage devices can be treated like voltage sources in that a range of currents are available from the source at a fixed voltage. In contrast, PV inverters must account for the current-voltage (I-V) curve of the PV array to which they are connected when regulating output power. Much of the work presented in the next two chapters deals with how to best regulate a PV inverter’s output power given that the I-V curve (and resulting power-voltage curve) are constantly changing and are not exactly known (or easily calculated) at any given time.

Some authors have also noted that frequency regulation could be provided from variable renewable sources without storage by operating below the maximum power output [55], [56]. These authors have simply assumed that the inverter operates sufficiently below the maximum power available from the input source (wind or solar) to allow sufficient power margin for frequency regulation needs without delving into the details of how that would be achieved.

Significant research covers APC of wind turbines for frequency regulation and other purposes, as summarized in [20]. PV-based frequency regulation will share some characteristics with wind-based frequency regulation but will also differ in important ways. Both are subject to the opportunity cost of not producing at full power, and both will depend on weather conditions. Unlike wind-based regulation, PV-based regulation will not be available outside of daylight hours. Both wind- and PV-based APC will be capable of very fast control responses. However, wind-based primary response is limited by the need not to draw down the kinetic energy of the turbine so much that it stalls and the need to allow blades to re-accelerate afterwards [20], whereas PV is not subject to this limit. Likewise, PV inverters need not be concerned with mechanical loads. The lack of mechanical dynamics in PV systems is the most fundamental difference between APC of wind and PV. APC of wind plants has been implemented commercially, whereas research into storage-free APC of PV plants is in a very early stage, and it has not been implemented commercially (aside from high-frequency power curtailment control).

Several authors have proposed incorporating electrochemical double layer capacitors (supercapacitors) into PV inverters to provide small amounts of energy storage, allowing limited bi-directional ramp-rate control and primary/inertial frequency regulation. For example, in [57] it is shown that a supercapacitor installed on the DC side of a PV inverter H-bridge can allow small-amplitude

modulation of inverter output power in response to short-duration frequency deviations. This provides primary frequency response, constrained by supercapacitor energy. In [58], a supercapacitor with a dedicated DC-DC converter is used to smooth photovoltaic power ramp rates.

Three papers are described below that describe various methods or partial methods of controlling the output of a PV system to operate below MPP, potentially allowing frequency regulation without storage.

In [26], a method is proposed to regulate the frequency of a PV-diesel-battery island power system. This method uses a fuzzy logic controller with inputs of solar irradiance, change in irradiance, and frequency deviation to produce a power command for the PV-battery inverter. It is also noted that the method can be used without energy storage if the PV is operated below its MPP. This paper notes the difficulty of operating some predetermined amount below a varying MPP, a challenge that is addressed in Chapter 3 of this thesis.

In [59], a method of controlling PV inverters to operate below MPP is described and simulated. This method assumes that the instantaneous open circuit voltage (V_{oc}) of the PV array is known and controls the PV array to operate at a constant proportion of V_{oc} (e.g. 95%), resulting in operation some amount below MPP. The paper does not address how the constantly-changing V_{oc} can be determined while the system is operating.

In [60], a control method is proposed that allows a PV inverter to track an absolute power reference below the PV array's maximum power. Low power experimental results are presented using an open-loop synchronous generator and a resistive load. The results show smaller steady-state frequency error when using a PV system controlled in the proposed manner in parallel with a generator than

when the generator powers the load alone. Frequency regulation dynamics are not analyzed. For any frequency below nominal, the control method described in [60] will simply operate the inverter at MPP.

In [61], a droop control based method of providing primary frequency regulation from a PV plant is presented. A reference power for the PV plant below its maximum power is assumed to be available; it is not discussed how this reference would be produced given changing irradiance. Frequency droop slope is controlled adaptively and non-linearly when the grid frequency falls outside a dead zone. Grid voltage is regulated simultaneously such that the PV inverter behaves similarly to a rotating generator. A simulated result is presented showing decreased frequency deviation following a single load step when the proposed control is enabled.

In [62], [63], a method is presented for providing primary frequency regulation from a PV plant by operating it in a “deloaded” condition, meaning the PV array voltage is controlled to be above the array’s MPP voltage. It is proposed that MPP voltage be estimated by feeding irradiance and temperature measurements into a PV array model; this estimation method is not tested or simulated. A simulated result is presented showing inertial response of the PV plant in a microgrid following a load step; a decreased grid frequency deviation is noted.

In [64], a large-scale demonstration is presented in which the controls of PV commercially available PV inverters are modified to enable APC in a Puerto Rico PV plant. Solar irradiance is used as an input to the controller to estimate the available PV power using equation (1):

$$P_a = A \cdot G_{avg} \cdot \frac{X}{40} - B \quad (1)$$

Here, P_a is the estimated maximum power available from the PV plant, A is the constant scaling factor based on historical performance, G_{avg} is the average irradiance from five meteorological stations, X is the number of inverters in operation, and B is a constant accounting for internal power consumption. Using the estimate P_a of available power, the PV plant was able to successfully provide AGC and primary frequency regulation. However, as shown in Figure 3, there is significant error between the estimated P_a (green trace) and the actual power available (where the blue trace peaks around 18.5 MW). This error occurs despite the use of historical data to tune the equation for P_a , and it results in the plant not following the AGC signal when the signal peaks.

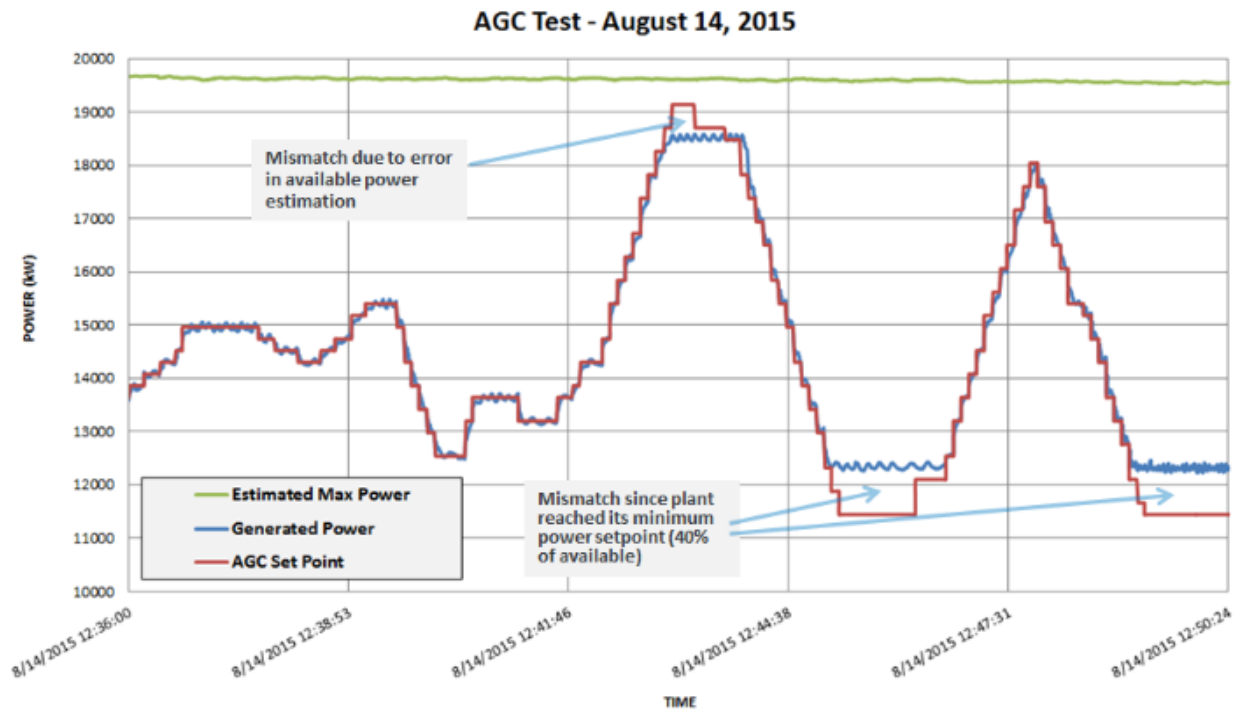


Figure 3. Demonstration of a PV plant performing AGC, from [64].

In addition, [64] presents tests of PV-based fast frequency response (FFR) service. FFR calls for a generator to transition from a curtailed state to full output power as quickly as possible in response to a simulated underfrequency event created by injecting a false frequency signal into the plant. An example FFR event is shown in Figure 4. The response is good in that the PV plant responds much faster than a conventional generator would, but could be improved upon in both speed and accuracy, as noted in [64]. There is a delay of about 100 ms before the response begins, and the response takes about 3 seconds to reach a maximum power (Figure 5). Again the maximum power reached is significantly below the estimated maximum power, as in Figure 3.

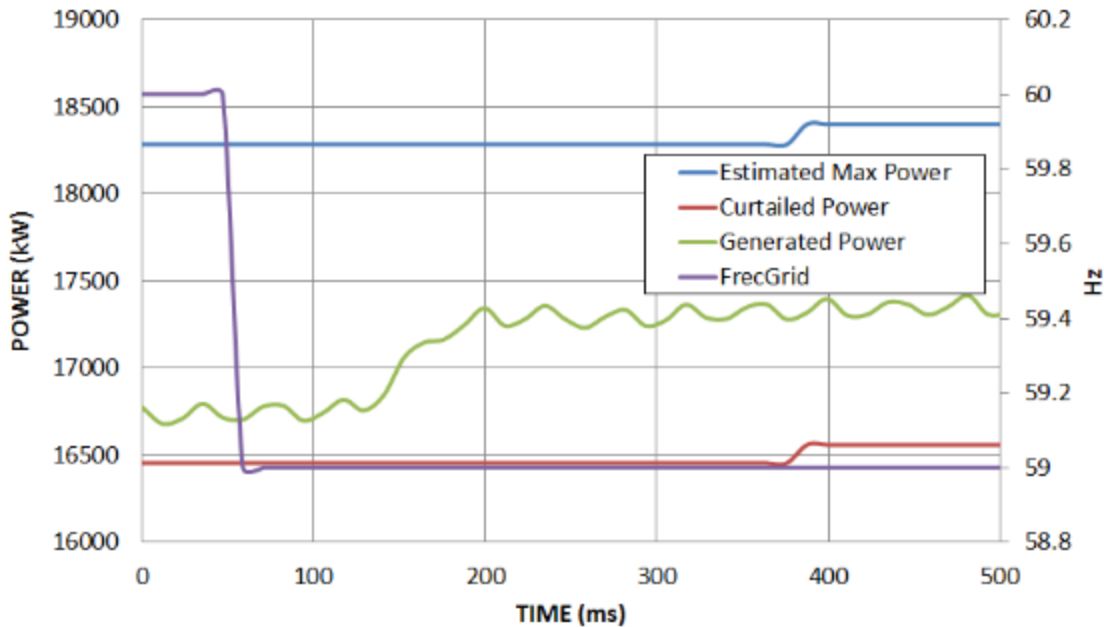


Figure 4. Demonstration of a PV plant performing FFR, from [64].

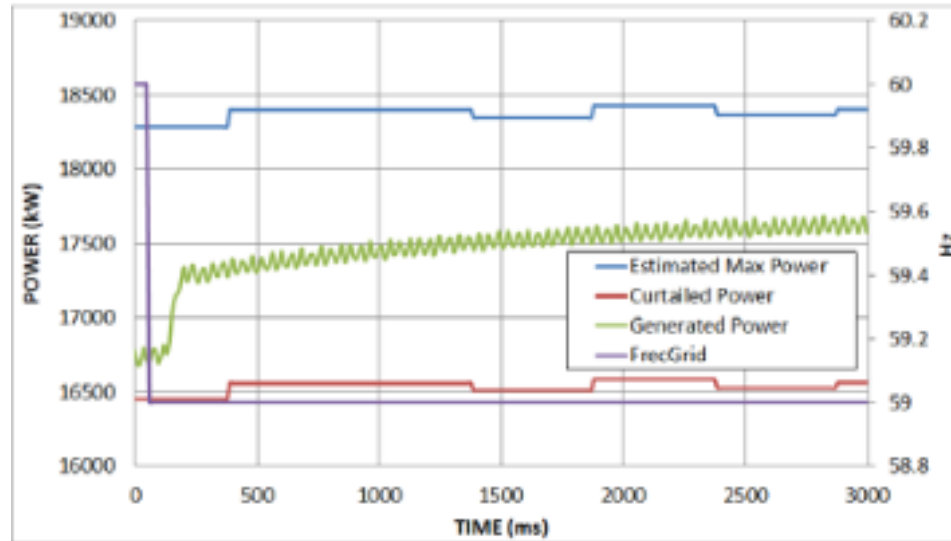


Figure 5. Demonstration of a PV plant performing FFR, expanded time range, from [64]

While these works have made important steps towards controlling a PV inverter's power output, significant research remains to be done. Specifically, methods are needed for:

1. Accurately estimating the maximum power available from a PV system
2. Quickly and accurately moving between operating points on a PV I-V curve.

Methods addressing items 1 and 2 above are presented in Chapters 3 and 4, respectively.

3 Real-time PV maximum power-point estimation (MPPE)

A method for real-time PV maximum power point estimation was introduced by the author and his collaborators in [65] and [66]. This chapter describes that MPPE method and presents newly-generated experimental data validating it.

A typical PV plant has no rotational inertia and has negligible energy storage. Therefore to perform primary frequency regulation (PFR), synthetic inertia, or other APC functions, it must operate below its maximum power point, P_{mp} , creating a power reserve margin that can be automatically dispatched during frequency transients [1], [62]. Typical PV inverters attempt to constantly operate at the maximum power available from the PV array using one of many MPPT methods, such as those summarized in [67]. The maximum power point of a PV array changes continuously over a wide range based on irradiance incident on the array and the temperature of the PV cells. If the maximum power is not being actively tracked by the PV inverter because the inverter is operating below P_{mp} , it is not trivial to know the value of P_{mp} . Put another way, typical MPPT methods rely on actually operating near P_{mp} to determine P_{mp} . This chapter presents a novel and experimentally validated maximum power point estimation (MPPE) method that is independent of the operating point of the inverter on the I-V curve. The proposed method operates in real time using irradiance and PV cell temperature measurements to ensure that sufficient reserve power is available.

Some previously proposed MPPE methods are intended for offline prediction of PV power for planning purposes, often employing regression analysis or neural networks [68], [69]. These methods can be quite accurate, but may require more

processing power than what is typically available in a PV inverter's embedded processor. Other methods intended for real-time calculation make assumptions that reduce the accuracy of the PV model [70]–[72] or require knowledge that is not typically available on PV module data sheets [70], [73]. The MPPE method proposed here uses a combination of

1. Offline calculation to estimate the parameters of a detailed PV cell model from data sheet values, and
2. Online, real-time computation of a second-order polynomial to estimate P_{mp} from irradiance and temperature.

This allows fast, accurate online estimation of P_{mp} .

Section 3.1 describes the proposed MPPE method, analyzes effects of irradiance variations on active power controls, and presents an experimental validation of the MPPE method. Section 3.2 describes one type of active power control that can be used in conjunction with MPPE. Section 3.3 presents simulations of electric power system frequency dynamics following a significant loss of generation both with and without PFR from PV, demonstrating one application of the MPPE method. The MPPE method is demonstrated experimentally in Section 3.4 by comparing the output power of an inverter controlled using MPPE to that of a commercially available inverter in MPPT mode. The MPPE method is again used in Section 4.3 to experimentally demonstrate the prototype inverter's response to frequency events.

3.1 MPPE method

Bi-directional active power control of PV systems without energy storage requires the ability to increase output power on demand. The minimum amount of power held in reserve for this purpose is determined by the specific application. In this work we assume that the required power reserve, P_{RES} , for the PV system is provided as an input to the system, for example by power system-level or market-level controls. The task of the inverter-level control proposed here is to estimate the instantaneous maximum power available, P_{mp} , and control the inverter to ensure that it operates around a power set point $P_{setPV} = P_{mp} - P_{RES}$, as shown in Figure 6. This allows the inverter to respond to changes in grid frequency by increasing or decreasing output power.

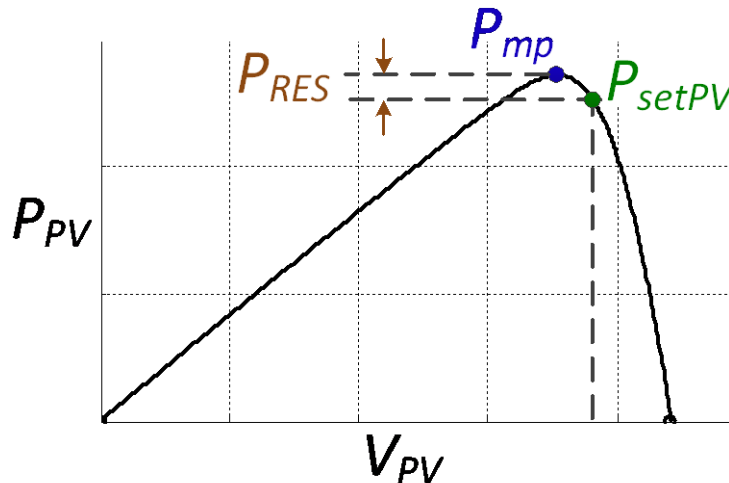


Figure 6. The power-voltage curve of a PV array illustrating an operating point P_{setPV} below the maximum power point.

Operating a PV system below P_{mp} incurs an opportunity cost associated with the power that is not produced. To minimize this opportunity cost it is desirable to operate as close to P_{mp} as possible while still ensuring that sufficient reserve power

P_{RES} is available for up-regulation. However, P_{mp} is constantly changing: it is a function not just of the physical characteristics of the PV array but also of the solar irradiance incident on the array, G , and the temperature of the PV cells, T . Therefore to minimize opportunity cost a real-time estimate of P_{mp} is needed.

3.1.1 *Estimating P_{mp} from Irradiance and Temperature*

The complete current-voltage (I-V) operating curve of a PV cell can be estimated from G , T , and the characteristics of the PV cell using one of the published models [67], [74], [75]. A PV module is made up of many cells connected in series and in parallel, with each series string having equal length. Likewise, a PV array is made up of many PV modules connected in series and in parallel, again with each series string having equal length. Hence, assuming that the array is not partially shaded, its I-V curve can also be estimated in the same manner, with voltages and currents scaled according to the total number of cells in series and in parallel, respectively. However, accurate PV cell I-V models require parameters not available in module data sheets, and they cannot be solved in closed form, so they do not lend themselves to rapid solution in embedded processors. We instead propose to use a second degree polynomial expression, $P_{mp1} \approx f(G, T)$, shown in equation (2), to estimate the maximum power of a PV module from measured irradiance and temperature. In steady-state, $P_{mp1} = P_{mp}/(\eta N)$, where η is the plant conversion efficiency and N is the number of PV modules in the plant. The coefficients in equation (2) can be derived through linear regression of P_{mp1} , G , and T data generated from PV module data sheet values as described in Subsection 3.1.2.

$$P_{mp1} = d + a_1T + a_2T^2 + b_1G + b_2G^2 + cTG \quad (2)$$

All lowercase letters in (2) are regression coefficients. Figure 7 shows a flowchart of the process used to find the regression coefficients in (2). The procedure described in this flowchart is performed once, at the time of PV system installation. Each step of this process and the process variables are described below, with an example calculation. The example calculation uses a PV array consisting of 26 Solarex 110S PV modules in two parallel strings of 13 modules each, which was available for experimental validation. The data sheet parameters of the Solarex PV module are shown in Table 1. These parameters are typically published for all commercially available PV modules; no additional inputs are needed to calculate the coefficients of equation (2). The calculation process only needs to be performed once for each PV system, and it is performed offline on a standard computer. The regression coefficients are then stored in the PV inverter controller's on-board memory for use in real-time MPPE.

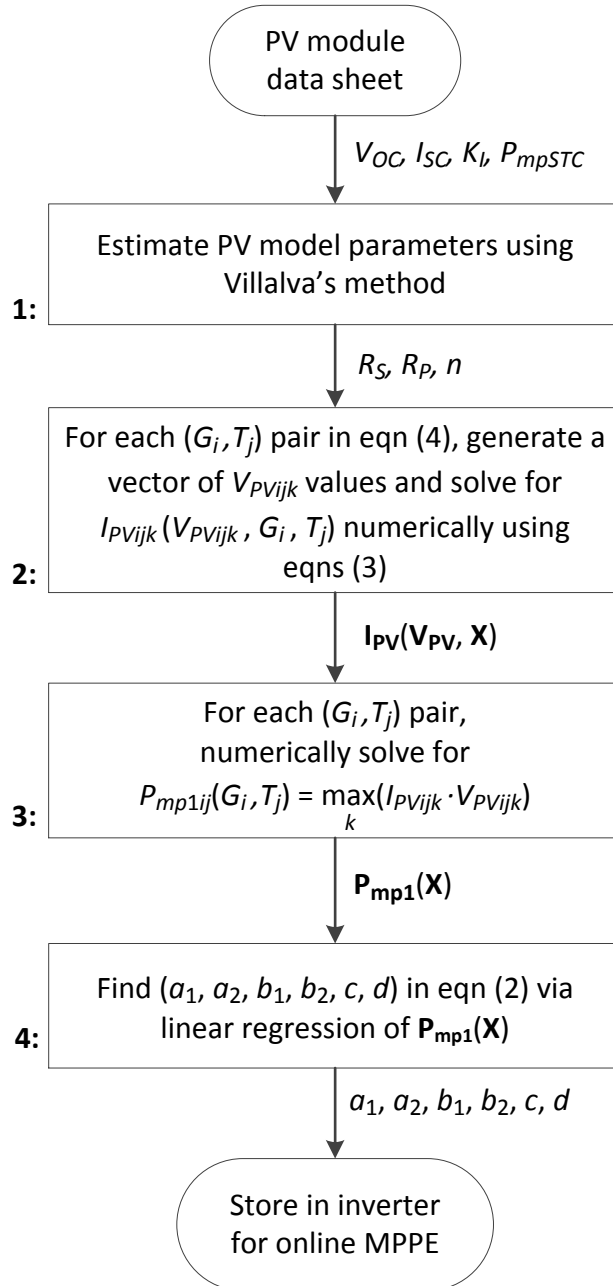


Figure 7. Flowchart for offline calculation of MPPE parameters in equation (2).

Table 1. Solarex 110S PV module data sheet parameters at standard test conditions (STC)

Parameter	Value	Units	Description
P_{mpSTC}	110	W	Maximum power
V_{mpSTC}	16.4	V	Voltage at maximum power
I_{mpSTC}	6.68	A	Current at maximum power
$I_{SC,STC}$	7.38	A	Short-circuit current
$V_{OC,STC}$	20.6	V	Open-circuit voltage
$C_{T,I}$	0.065	%/°C	Temperature coefficient of $I_{SC,STC}$

3.1.2 Offline Parameter Estimation

This subsection provides the details of each step of the flowchart in Figure 7. But first, the five-parameter PV cell model is introduced.

PV I-V curves can be modeled using a five-parameter model as shown in Figure 8 and described in equations (3).

$$\begin{aligned}
 I_{PV} &= I_{Ph}(G, T) - I_0(G, T) \left(e^{\left(\frac{q(V_{PV} + R_S I_{PV})}{knT} \right)} - 1 \right) - \frac{V_{PV} + R_S I_{PV}}{R_P} \\
 I_{Ph} &= \frac{G}{G_{STC}} I_{SC} \left(\frac{R_S + R_P}{R_P} \right) (1 + K_I(T - T_{STC})) \\
 I_0 &= \frac{I_{Ph} - V_{OC} / R_P}{e^{\left(\frac{qV_{OC}}{knT} \right)} - 1}
 \end{aligned} \tag{ 3 }$$

Here, I_{PV} is the net PV cell current, I_{Ph} is the light-generated photocurrent, I_0 is the diode saturation current of the PV cell p-n junction, q is the electron charge, V_{PV} is the PV cell voltage, R_S is the modeled series resistance, k is Boltzmann's constant, n is the diode ideality constant (assumed to be $n = 1$, as in [75]), R_P is the modeled shunt resistance, $G_{STC} = 1000 \text{ W/m}^2$ is the irradiance at standard test conditions (STC), I_{SC} is the data sheet short-circuit current (at STC), K_I is the data sheet

temperature coefficient of I_{SC} , $T_{STC} = 25$ C is the temperature at STC, and V_{OC} is the data sheet open-circuit voltage (at STC).

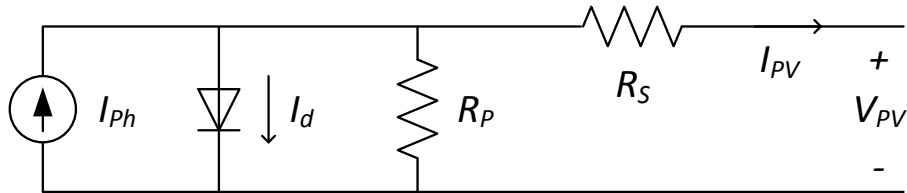


Figure 8. The five-parameter model of a PV cell.

The parameters of (3) are not all given in PV module or cell data sheets; specifically, R_S , R_P , and n must be determined. In addition, even if all parameters are known, equations (3) have no closed form solution for $I_{PV}(V_{PV}, G, T)$; note that I_{PV} and V_{PV} both occur in various places within (3), including inside exponentials. Thus, solving (3) rapidly in real time in an embedded processor is a difficult task, as is finding the maximum power point $P_{mp1} = \max(I_{PV}(G, T) * V_{PV}(G, T))$. The MPPE method presented here avoids that task by solving the entire operating space $P_{mp1} = f(G, T)$ beforehand and storing the results in (2).

Step 1 of the flowchart in Figure 7 uses a numerical method presented in [75] to find R_S and R_P from values given in typical PV cell and module data sheets including V_{OC} , I_{SC} , K_I , and P_{mpSTC} , the maximum output power at STC.

Using Matlab scripts to solve for R_S and R_P for our example Solarex PV module via the method described in [75], we find $R_P = 52.202 \Omega$ and $R_S = 0.2282 \Omega$.

Step 2 in the flowchart starts by generating a matrix \mathbf{X} of (G_i, T_j) pairs that covers the entire range of temperature and irradiance values expected to be encountered in the field:

$$\mathbf{X} = \begin{bmatrix} (G_{min}, T_{min}), & (G_2, T_{min}), & \dots & (G_i, T_{min}), & \dots & (G_{max}, T_{min}) \\ (G_{min}, T_2), & (G_2, T_2), & \dots & & & (G_{max}, T_2) \\ \dots & & & & & \dots \\ (G_{min}, T_j), & & \dots & (G_i, T_j), & \dots & (G_{max}, T_j) \\ \dots & & & & & \dots \\ (G_{min}, T_{max}), & (G_2, T_{max}), & \dots & (G_i, T_{max}), & \dots & (G_{max}, T_{max}) \end{bmatrix} \quad (4)$$

G_{min} and G_{max} are the minimum and maximum expected irradiance, 0 W/m² and 1200 W/m² in the example, respectively. T_{min} and T_{max} are the minimum and maximum expected cell temperatures, -30 C and 90 C in the example, respectively. The minimum and maximum values chosen for G and T have little impact on the outcome of the calculation as long as they cover the range of expected operating conditions. Intermediate values $[G_2, G_3, \dots, G_i, \dots]$ and $[T_2, T_3, \dots, T_j, \dots]$ are chosen so that there are enough data points to accurately represent the module characteristic and avoid creating artifacts in the 2nd order linear fit. In the example considered, 10 irradiance data points and 10 temperature data points are used, both evenly spaced, so \mathbf{X} is a 10 by 10 matrix.

Continuing with step 2, for each (G_i, T_j) pair in (4), a vector $\mathbf{V}_{PVij} = [V_{PVij1}, V_{PVij2}, \dots, V_{PVijk}, \dots, V_{PVijm}]$ is generated. This vector of m voltages should cover the range from zero volts to the highest PV module voltage expected. Note that this is typically somewhat higher than the open circuit voltage V_{OC} given in the data sheet because the PV cell voltages rise as temperatures fall. The range of voltages for the example system using the Solarex module goes from zero to 1.05* V_{OC} . Five hundred evenly spaced voltage points are selected. For each V_{PVijk} , equations (3) are used to solve numerically for $I_{PVijk} = I_{PVijk}(V_{PVijk}, G_i, T_j)$. The result is a three-dimensional

matrix $\mathbf{I}_{PV} = \mathbf{I}_{PV}(\mathbf{V}_{PV}, \mathbf{X})$ representing the I-V curves of the PV module at discrete points covering the entire range of possible operating conditions.

In step 3, the maximum power of each I-V curve at each operating point (G_i, T_j) in \mathbf{X} is numerically solved:

$$P_{mp1ij}(G_i, T_j) = \max_k (I_{PVijk} \cdot V_{PVijk}) \quad (5)$$

The result of step 3 is a two-dimensional matrix $\mathbf{P}_{mp1}(\mathbf{X})$ containing the unique maximum power points P_{mp1ij} for each (G_i, T_j) pair.

In the fourth and final step of the offline process, the fit parameters of (2) are found by solving for $\boldsymbol{\beta}$ in the linear regression problem $\mathbf{P}_{mp1} = \mathbf{X}_1 \boldsymbol{\beta}$. Here $\boldsymbol{\beta}^T = [d, a_1, a_2, b_1, b_2, c]$ is the vector of regression coefficients from (2), and \mathbf{X}_1 is a matrix of irradiance and temperature values and second-order combinations thereof:

$$\mathbf{X}_1 = \begin{bmatrix} 1 & T_{min} & T_{min}^2 & G_{min} & G_{min}^2 & T_{min} G_{min} \\ 1 & T_{min} & T_{min}^2 & G_2 & G_2^2 & T_{min} G_2 \\ \vdots & \vdots & \vdots & \vdots & \vdots & \vdots \\ 1 & T_j & T_j^2 & G_i & G_i^2 & T_j G_i \\ \vdots & \vdots & \vdots & \vdots & \vdots & \vdots \\ 1 & T_{max} & T_{max}^2 & G_{max} & G_{max}^2 & G_{max} T_{max} \end{bmatrix} \quad (6)$$

\mathbf{X}_1 contains one row for each element of \mathbf{X} (i.e. each unique combination of temperature and irradiance) and one column for each element of $\boldsymbol{\beta}$. For the example, \mathbf{X} is 10 by 10 and $\boldsymbol{\beta}$ has 6 elements, so \mathbf{X}_1 has 100 rows and 6 columns.

In the example, solving for $\boldsymbol{\beta}$ using Matlab's Curve Fitting Toolbox produces the parameters listed in Table 1 for the Solarex 110S module. The coefficient of

determination (“R squared”) of the fit is 0.999, indicating that the polynomial is a nearly perfect fit to the nonlinear function $P_{mp1}(G, T)$.

Table 2. Regression fit parameters for equation (2) for Solarex PV module example

Parameter	Value
d	-5.685
a ₁	0.04971
b ₁	0.1293
a ₂	-2.291e-4
b ₂	-2.086e-6
c	-5.377e-4

With the coefficients in (2) found, this simple second-order polynomial can be used to estimate P_{mp} in real-time from measured G and T , as shown in Figure 9. The filter corner frequency, w_c , in Figure 9 is a function of the PV array size and is defined and explained in Subsection 3.1.3.

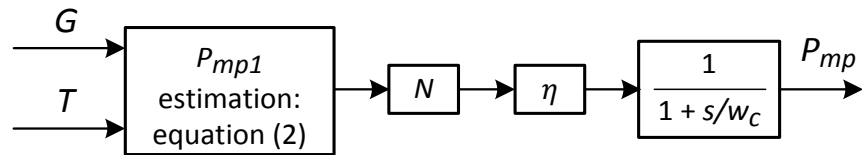


Figure 9. Estimating maximum available PV power from measured irradiance and temperature in real time. N is the number of PV modules in the array, η is the conversion efficiency of the PV plant, and the first-order cutoff frequency w_c is described in Subsection 3.1.3.

Note that irradiance and temperature are not entirely uniform across a PV array, so some P_{mp} error will exist. When implementing an active power control

scheme, this error can be accounted for by increasing the reserve power by a small margin to ensure that the desired reserve power P_{RES} is available under worst-case expected error conditions.

The output power of PV modules degrades over their lifetime. This degradation is fairly linear with time and typically proceeds at a rate of less than 1% per year [76]. This degradation rate can be accounted for in MPPE by incorporating it into the system conversion efficiency, η , as a function of time, t , in days since the system was installed:

$$\eta = \eta_0 \cdot \left(1 - \frac{r \cdot t}{365}\right) \quad (7)$$

Here r is the annual rate of degradation of P_{mp} and η_0 is the total conversion efficiency of the PV system at the time of installation, which can be determined experimentally during commissioning or estimated from system component specifications.

The Solarex modules in the example were installed in February 2003 and hence are about 13 years old. Using a typical degradation rate, r , of 0.5% per year [76], these modules are expected to operate at about 93% of their initial maximum power for a given irradiance and temperature. Assuming an initial system-level DC-AC efficiency of $\eta_0 = 94\%$ (including inverter losses and wiring losses), a value of $\eta = 0.88$ is calculated at this point in the Solarex system life.

3.1.3 Effect of irradiance variability

In addition to reducing the amount of conventional inertia available on an EPS, conventionally operated PV plants also contribute to frequency and voltage deviations through their own inherent variability as clouds pass. However, because frequency deviations are system-wide, geographic dispersal of PV plants serves to

mitigate this effect [77], [78]. Even considering a worst-case scenario of a single large PV plant, the physical size of the PV plant also reduces the maximum rate of cloud-induced power ramps, effectively acting as a first order low-pass filter with a cutoff frequency of w_c [79], [80]:

$$w_c = 2\pi \cdot \frac{0.02}{\sqrt{4.6 \cdot P_{rat}}} \quad (8)$$

Here P_{rat} is the rated PV plant power in MW.

From equation (8) it can be shown that over the five to 15 crucial seconds at the start of a frequency transient, the aggregate available PV output power changes very little as long as the total PV capacity is in the tens of MW or above. Therefore, when considering the frequency impacts of the aggregate power output of one or more PV plants totaling 10 MW or more, it is reasonable to assume that the maximum available PV power does not change significantly over the crucial initial part of a frequency transient event.

This is of course only helpful if the PV plants continue to operate during the frequency event, which may not be the case for some older inverters complying to frequency trip settings in IEEE Standard 1547-2003 [81]. Fortunately, IEEE 1547 has been amended to allow DERs to “ride through” a wider range of frequency and voltage events [82], and is in the process of being fully revised [83]. Many U.S. utilities with high levels of PV are requiring frequency ride-through from DERs [84], [85], helping pave the way for PV active power controls to mitigate frequency events.

3.2 Droop control

The MPPE method described above can be used to ensure a given power reserve P_{RES} is available at minimum opportunity cost. This power reserve can be used in a variety of ways to stabilize grid frequency. This section (and the subsequent experimental results) focus on one particular autonomous APC function: power-frequency droop response. By taking advantage of the fast response of power electronics, such a droop response can provide not just primary frequency regulation, but also something similar to the stabilizing effect of synchronous machine inertia. While a very fast droop response can reduce the severity of frequency events in a manner similar to physical inertia, it differs from physical inertia in several key ways:

1. Droop reacts to the deviation of measured grid frequency from its nominal value, whereas physical inertia responds to the first time derivative of frequency.
2. Physical inertia responds to local frequency instantaneously, whereas droop response will always have some short delay due to the time for the phase-locked loop (PLL) to detect the frequency change and the inverter controls to take action.
3. Physical inertia is an inherent property of rotating machines and cannot be easily changed, whereas droop parameters can be easily adjusted at any time.

Using a simple averaged-switch model [86], a PV inverter can be modeled as a controlled three-phase current source with an output filter. Such a model can be used for power system simulation of inverter droop response; a switching-level inverter model is not needed because dynamics faster than a few hundred Hz are

much faster than EPS frequency dynamics. The power-frequency droop control providing the reference output current for PFR is shown in Figure 10. P_{setPV} is the droop power set point and is equal to $P_{mp} - P_{RES}$. R_{PV} is the inverter droop slope, P_{cmd} is the active power command, V_{AC} is the rms AC voltage at the inverter terminals, and i_d is the direct current command in the synchronous dq0 reference frame. P_{setPV} is the power set point at which the inverter operates when in droop mode at nominal frequency. PV inverter control dynamics occur much faster than the mechanical control time-scale of grid frequency transients and hence are neglected for the purposes of the simulations presented in the next section.

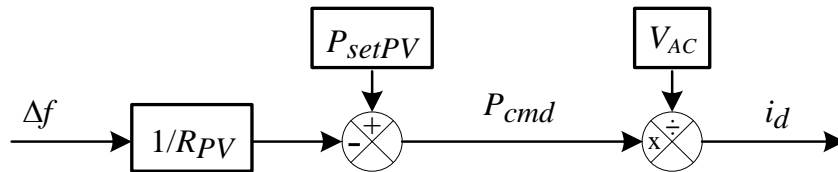


Figure 10. Inverter power-frequency droop controller (without deadband).

In Chapter 4, additional control details are provided for tracking P_{cmd} using a different method from the one shown in Figure 10 in which inverter control dynamics are accounted for.

3.3 PV APC simulation

This section presents dynamic simulations of a PV inverter providing droop response enabled by MPPE in a power system. The electric power system dynamic model is a simple one that captures frequency dynamics but not voltage dynamics.

Figure 11 presents an overview of the EPS line-frequency response model used here, including grid frequency dynamics. The EPS frequency dynamic model is based on the model presented in [87], which is in turn based on a model presented in [88] of the U.S. Western Interconnection. The grid frequency dynamics are modeled based on a reheat steam turbine – a common type in the U.S. – and include inertia, load damping, and governor droop, as derived in [89]. This model has been adapted for this study by reducing the total grid power and total interconnection inertia, J , though the inertia constant, H , remains the same because it is calculated in per-MW terms. In addition to the large steam turbine representing the “rest of the interconnection” (ROI), the model also contains a single 43 MW steam turbine, which can be taken offline to simulate a large frequency drop.

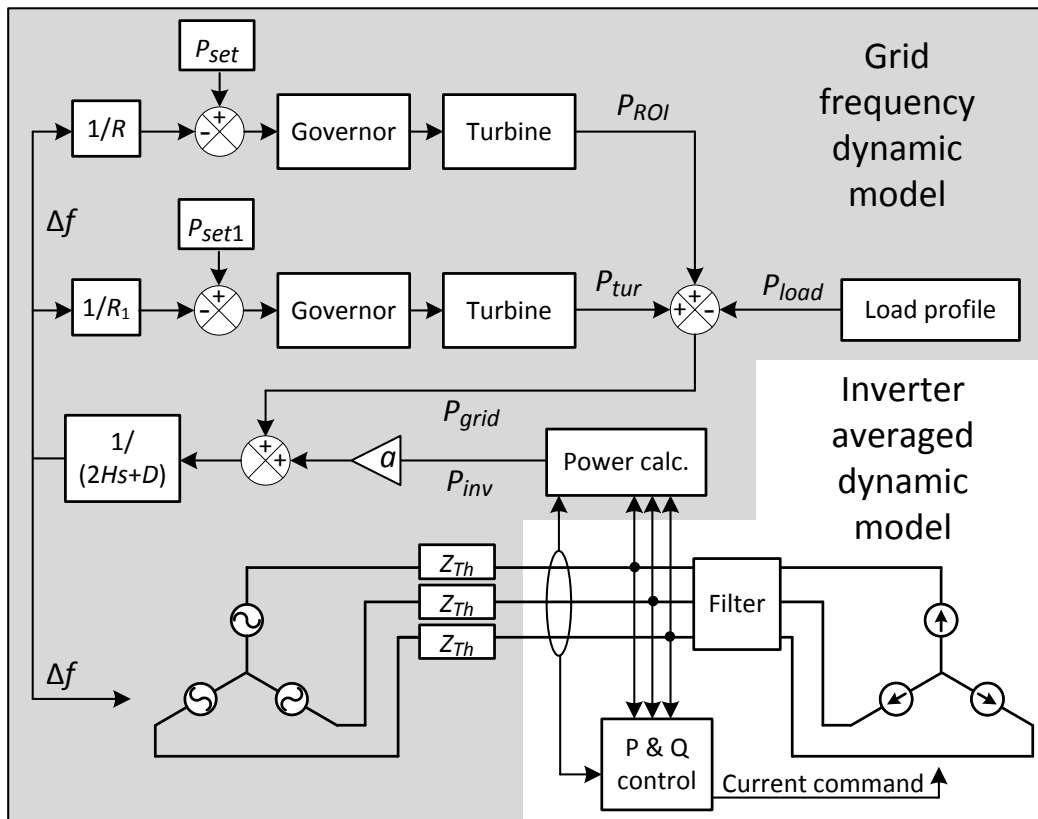


Figure 11. Line-frequency response model of grid and PV inverter.

The output of the model in Figure 11 is Δf , the per-unit change in frequency away from nominal. P_{inv} , P_{load} , and P_{grid} are the power from the inverter, the load power, and the power from all other generators in the interconnection, respectively. P_{tur} is the power from the 43 MW turbine, and P_{ROI} is the power from the rest of the interconnection. The gain α is unity if modeling a single inverter, but can be made larger to model multiple identical PV plants. The droop slope, R , is the composite droop from all generator speed governors in the ROI. The inertia constant, H , represents the total inertia of all generators and loads on the system. The load damping constant, D , represents the change in total load for a given change in frequency. The power set point, P_{set} , represents the composite power set point for the system. The 43 MW turbine has droop slope R_1 and power set point P_{set1} ; its governor and turbine dynamics are identical (on a per-unit basis) to those of the ROI. The load profile represents the total system load. The governor and turbine transfer functions for the ROI are shown in Figure 12. This figure applies to the 43 MW turbine as well, substituting R_1 for R , P_{set1} for P_{set} , and P_{tur} for P_{ROI} .

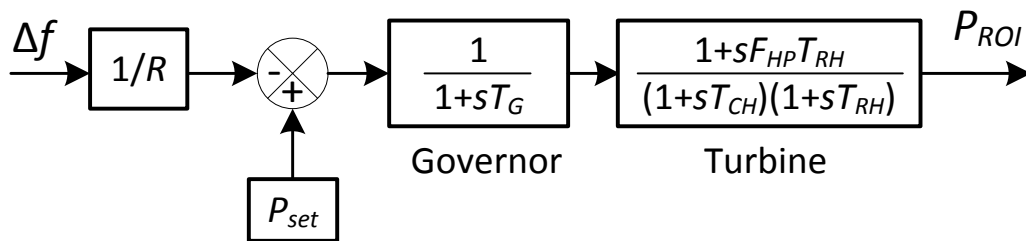


Figure 12. Governor and turbine transfer functions for grid dynamic model

In Figure 12, T_G is the governor time constant, F_{HP} is the fraction of turbine power from the high pressure section, T_{RH} is the reheater time constant, T_{CH} is the charging time of the high pressure section, and s is the Laplace frequency variable. Typical values of the variables as given in [89] are shown in Table 3. Unless otherwise indicated, these are the values used in the tests described below.

Table 3. Parameters for EPS frequency model

Variable	Typical value	Units
R	0.05	pu Hz / pu W
H	5	s
D	1	pu W / pu Hz
T_G	0.2	s
F_{HP}	0.3	-
T_{RH}	7	s
T_{CH}	0.3	s

This model does not incorporate longer time-scale controls such as secondary frequency regulation; it is appropriate for frequency transient studies lasting a few tens of seconds and is not designed for simulations lasting minutes or longer.

The grid model was implemented in Simulink/SimPowerSystems. Two scenarios are shown: a baseline scenario without PV-based PFR, and a scenario with 200 MW of PV providing PFR with $P_{RES} = 20$ MW. Table 4 shows the baseline simulation parameters. In each scenario, a 43 MW steam turbine drops offline at time $t = 105$ s, initiating a frequency transient event. The R value for the ROI is higher than the typical value of 0.05 because it represents the effective droop constant of the entire interconnection, including external load damping [88]. The

minimum frequency f_{min} to avoid load-shedding, generator tripping, or instability is taken to be 59.8 Hz. As input to the PV system, both scenarios use measured irradiance and temperature from June 5, 2014, at 11:00 am, filtered for a 200 MW PV system using equation (8).

Table 4. Baseline frequency transient simulation parameters

Variable	Value	Units
P_{set}	1855	MW
R	0.22	pu Hz / pu MW
P_{set1}	43	MW
R_1	0.05	pu Hz / pu MW
P_{max_PV}	200	MW
P_{load}	2062	MW
f_{min}	59.8	Hz

Figure 13 shows simulations of two frequency events. The baseline event with no PV active power controls is at left and the event with PV-based frequency response is at right. Both events show the grid frequency and the output power from each of the generators before, during, and after the frequency transient triggered by the tripping of the 43 MW steam plant. In the baseline event, the frequency nadir is 59.68 Hz, well below the assumed value of f_{min} , likely triggering load shedding. In the second event, PFR from the PV system was enabled using $P_{setPV} = P_{mp} - P_{RES}$, with $P_{RES} = 20$ MW and $R_{PV} = 0.05$. P_{set} , the ROI power set point, was adjusted up to 1957 MW so that the grid frequency would be stable at 60 Hz at the time of the frequency transient event. All other parameters remained the same. As shown in Figure 13, the contribution of the PV plant helps keep the frequency from falling below f_{min} , sufficient to avoid load-shedding and instability. Thus this dynamic

simulation provides a simple example of the use of MPPE and PV-based primary frequency response to reduce the magnitude of a grid frequency transient on a low-inertia grid.

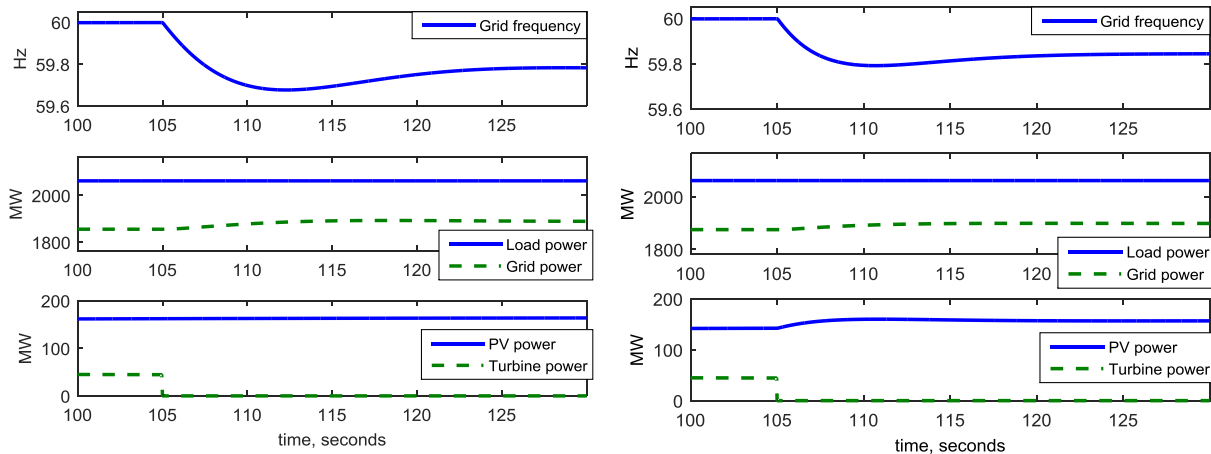


Figure 13. Left: Baseline frequency transient event: no PV-based primary frequency regulation. Right: Frequency transient event with PV-based primary frequency regulation enabled with 20 MW power reserve.

3.4 MPPE experimental demonstration

Figure 14 presents an experimental validation of the P_{mp} prediction method. The method was validated by comparing the measured output power of a 3 kW commercially available PV inverter in MPPT mode to the maximum power, P_{mp} , as predicted using (2) from measured irradiance and temperature on June 5, 2014, at NREL's Distributed Energy Resource Test Facility (DERTF) near Boulder, CO. The PV inverter was fed by a PV array consisting of 26 Solarex 110S modules. These are the same PV modules used in the example calculation above. The DC-AC conversion efficiency, η_0 , was taken to be 0.95. The predicted power (blue trace)

matches very well to the measured power (red trace), except during some fast cloud transients when it appears the inverter's MPPT algorithm fails temporarily. Note that the effect of low-pass filter effect discussed in Subsection 3.1.3 is negligible on the time scale shown in Figure 14 for such a small PV system.

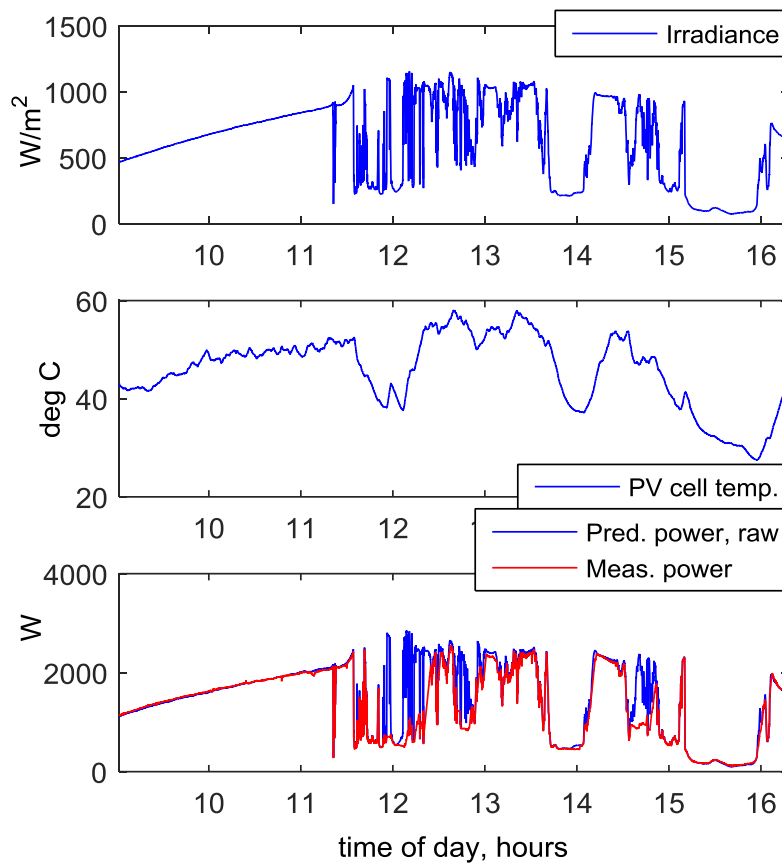


Figure 14. Preliminary experimental validation of the MPPE method. The top two plots show measured irradiance and PV cell temperature. The bottom plot shows the predicted output power and the measured output power of a commercial inverter operating in MPPT mode.

The day selected for Figure 14 was chosen because of its large variations in irradiance and temperature. The match between predicted PV power and measured

PV power on other days examined is as good as or better than what is shown in Figure 14. In the absence of large cloud transients the predicted power is nearly coincident with the measured power because the PV inverter is able to successfully track peak power at all times. As mentioned in Subsection 3.1.3, large cloud transients will not have such a noticeable effect when larger PV arrays or collections of geographically diverse PV arrays are considered.

After this preliminary validation of the MPPE method, it was implemented in a prototype inverter developed at NREL [90], [91]. This single-stage, three-phase, 50 kVA inverter uses a three-phase bridge power stage and has an inductive-capacitive (LC) output filter, as shown in Figure 15. It was designed to connect DERs such as battery or PV systems to the electric grid. The inverter is controlled by a National Instruments single-board RIO (9606 sbRIO), which combines a real-time processor with a field-programmable gate array (FPGA). The lower-level controls had been implemented on the FPGA by others prior to the start of this thesis research [91]. A general overview of those controls is provided here for reference. The FPGA controls include rotating synchronous reference frame (d-q) current control using sinusoidal pulse-width modulation (PWM), a phase-locked loop (PLL) for grid synchronization, and DC bus voltage control. The PWM switching frequency is adjustable and was set to 10 kHz. The direct (d) current control, quadrature (q) current control, and DC voltage control loops use proportional-integral-derivative PID controllers with adjustable gains. All derivative (D) gains were set to zero. The low-level controls can be operated either in current control mode, in which direct current i_d is commanded, or in DC voltage control mode, in which DC voltage v_{dc} is commanded. In either case, the current phase angle ϕ can also be commanded. These controls were implemented in a

National Instruments LabView virtual instrument (VI) and compiled onto the Xilinx Spartan 6 LX45 FPGA embedded in the sbRIO.

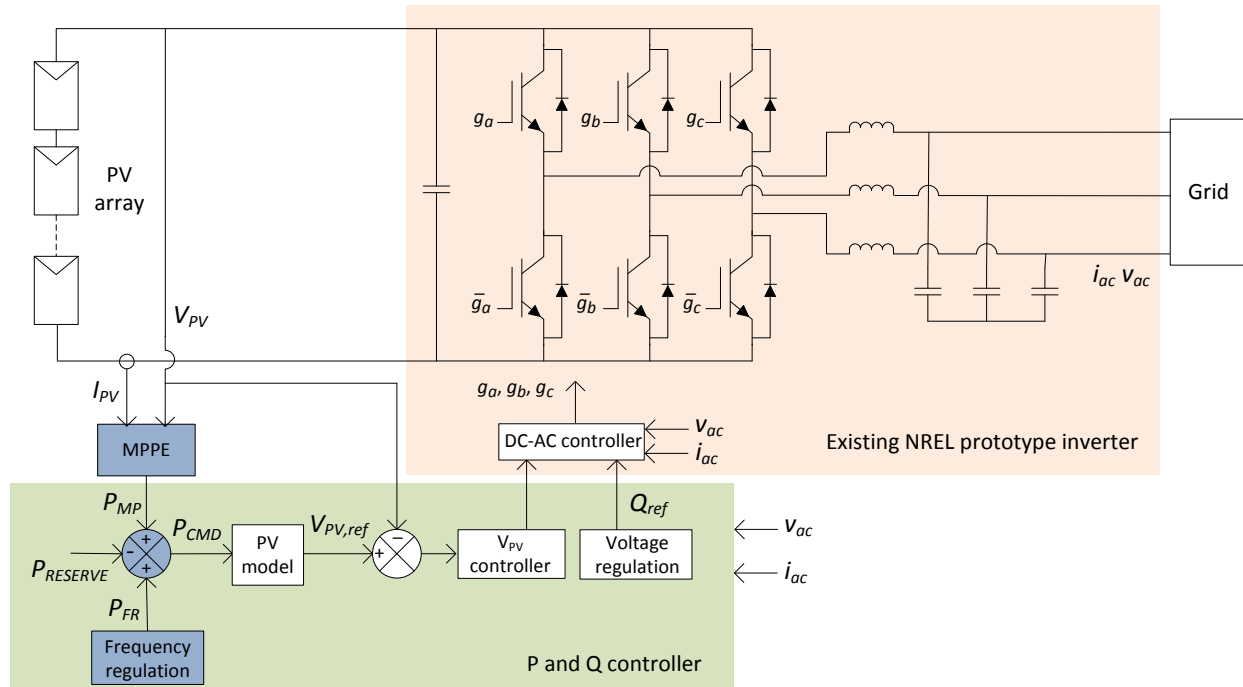


Figure 15. Experimental setup for hardware validation of MPPE method.

The active power controls were implemented on the real-time processor of the sbRIO. Control code was written using LabView's Real-Time graphical programming language. The real-time processor communicates with the low-level code on the FPGA, receiving information on frequency, RMS AC voltage and current on each phase, DC voltage and current, and other parameters. In APC mode, the DC bus voltage is controlled to the desired location on the PV array's I-V curve to modulate active power. Thus the low level controls are operated in DC voltage control mode and the active power control code on the real-time processor sends DC voltage commands to the FPGA. The FPGA interfaces with several analog to digital

converters (ADCs) on the sbRIO. Solar irradiance and PV module temperature signals were connected into two unused ADCs, processed in the FPGA, and passed on to the real-time code.

Two LabView timed loops were implemented in the real-time processor. A slower loop running at a 1-second update rate estimates the maximum power point of the PV array using the MPPE method described above. It also receives reserve power P_{RES} commands and control mode commands from the VI's graphical user interface (GUI) and calculates the operating power set point, P_{SET} .

A faster timed loop operating at a rate of 50 ms receives P_{SET} commands from the slower loop. When operating in primary frequency regulation mode, a frequency regulation power P_{FR} is added to P_{SET} to produce a power command, P_{cmd} . P_{FR} is calculated based on a power-frequency droop curve with an adjustable slope entered via the GUI. The desired operating power is converted into a DC voltage command via a method described in Chapter 4. For the PV APC demonstration, the inverter sbRIO controller was also programmed to record internal control signals during operation.

A test setup was constructed to compare the prototype inverter's operation to that of a common commercially available grid-interactive PV inverter operating in MPPT mode. The test setup for the prototype inverter is shown in Figure 16. The inverter input was supplied by one of the two identical Solarex 110S PV arrays at NREL's DERTF, shown in Figure 17. Each array consists of 48 modules, for a total power rating of 5.28 kW. The array connected to the prototype inverter was configured in two parallel strings of 24 modules each. On the AC side, the prototype inverter was connected to a three-phase AC grid simulator. A load bank was also

connected in parallel with the grid simulator because the grid simulator used here can only source power.

One of the two DERTF PV arrays was instrumented with an Ingenieurburo Si-420-TC-T reference cell irradiance sensor and an Ingenieurburo Tmodul420 temperature sensor. It was assumed that because the two PV arrays use identical modules and mounting methods, have identical azimuth and orientation, and are only about 10 meters apart, they will experience nearly identical irradiance and temperature profiles. The irradiance sensor was mounted in the same plane as the PV array, as shown in the photograph inset into Figure 16. The temperature sensor is designed to adhere to a surface (such as the back of a PV module) and measure the temperature of that surface. Like most PV modules, the Solarex modules have only a thin plastic backsheet covering the backs of the PV cells, so the temperature sensor is able to provide an accurate estimate of the temperature of the PV cells themselves.

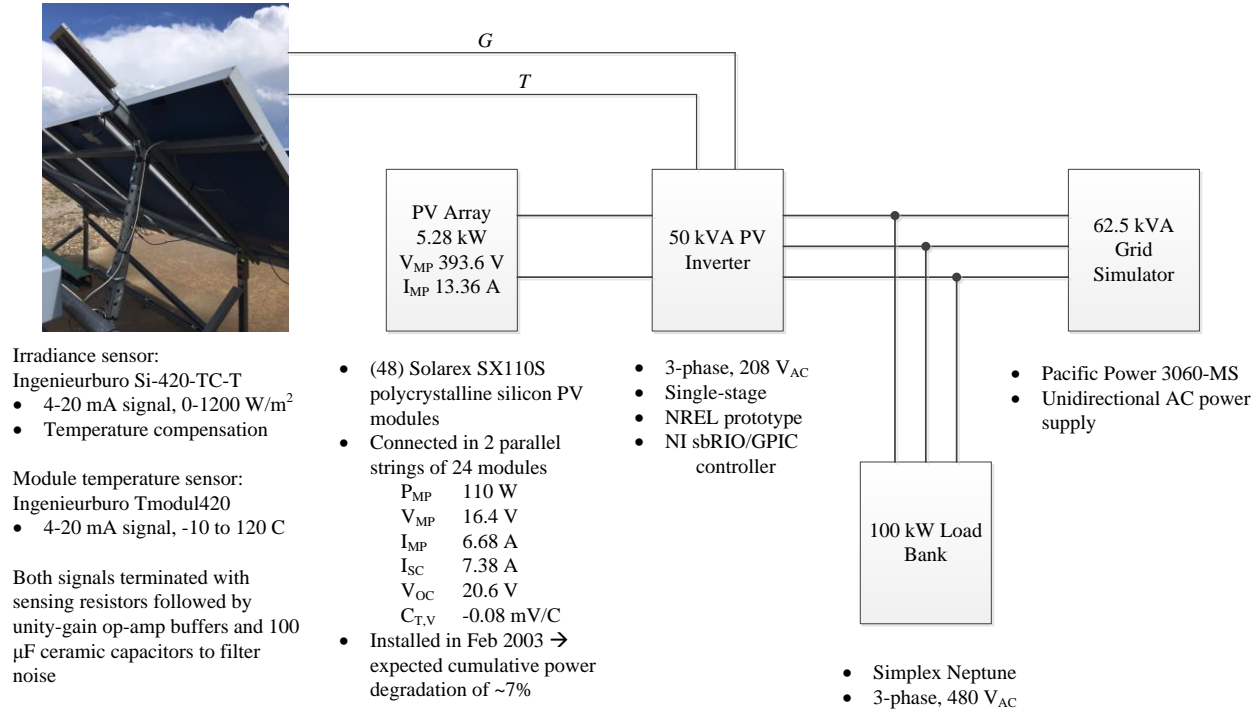


Figure 16. Experimental setup for hardware validation of MPPE method.

The second PV array was connected to an SMA SB3000TL-US-22 PV inverter, which has a power rating of 3.0 kW. To ensure the SMA inverter always operated in MPPT mode, the PV array connected to it was configured in two parallel strings of 13 modules each, for a power rating of 2.86 kW. The remaining 22 modules in that array were left disconnected. On the AC side, the SMA inverter was connected to the local electrical grid.



Figure 17. The two identical PV arrays used for experimental validation of MPPE and RAPC. One array is in the left foreground, and the second is to the right and slightly behind it. The inverter and test equipment are located in the DERTF building behind the right hand array.

Figure 18 shows recorded powers from the two inverters over a 3.6-hour period on a partly cloudy day. The prototype inverter (Inverter 1) operated in MPPE mode with a reserve power of 500 W (1.1 pu), and the SMA inverter (Inverter 2) operated in MPPT mode. The blue trace shows the maximum power estimate, P_{MPPE} ; the red trace shows P_{cmd} ; and the yellow trace shows P_{AC1} , the output power of the prototype inverter, all recorded in the sbRIO. The purple trace shows the output power of the SMA inverter, measured on a separate data logging system. Because the SMA inverter is powered by fewer Solarex PV modules than the prototype inverter, the power traces in Figure 18 are all shown on a per-unit basis with the nominal power levels of the respective PV arrays as the power bases. Thus P_{MPPE} and P_{AC2} can be directly compared to validate the MPPE method.

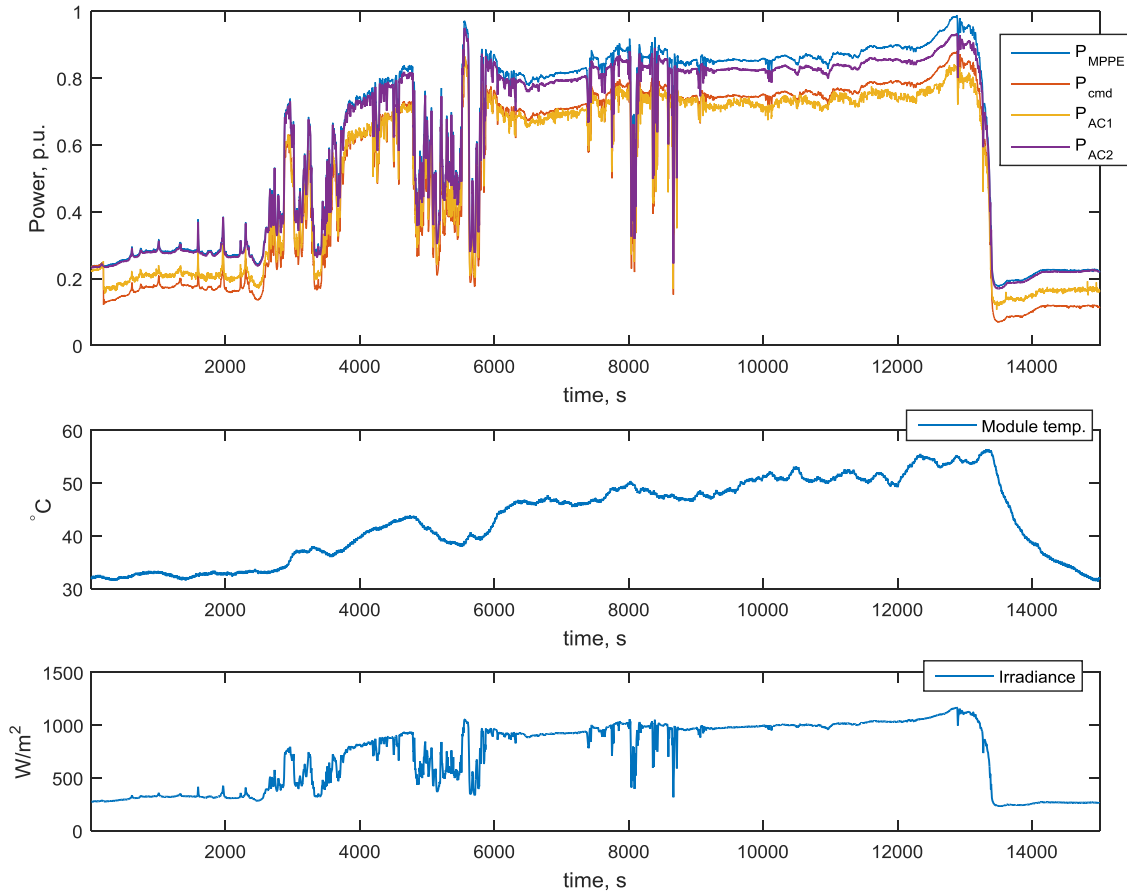


Figure 18. Demonstration of a prototype inverter operating in MPPE mode with a reserve power of 500 W while a second inverter operates in standard MPPT mode.

At lower power levels, P_{MPPE} , the real-time maximum power estimate in the prototype inverter, and P_{AC2} , the output power of the SMA inverter, are nearly equal in Figure 18, as desired. At higher power levels, P_{AC2} tracks slightly below P_{MPPE} . This error in the MPPE method is likely due to a mismatch between the expected system AC-DC conversion efficiency and the actual efficiency. Some methods to mitigate this error are discussed in Section 8.2. The commanded power output of the prototype inverter, P_{cmd} , tracks about 1.1 pu below P_{MPPE} , as expected. The measured output power of the prototype inverter, P_{AC1} , is slightly lower than

P_{cmd} at higher power levels and somewhat higher at lower power levels. The discrepancy at lower power levels is likely largely due to measurement error: the prototype inverter's power was calculated from RMS AC current and voltage and phase angle of current, and the RMS calculations implemented in the FPGA are true RMS, rather than fundamental frequency RMS. Thus all noise and any DC component of the voltages and currents gets coupled into the power measurement and throws off the measurement significantly at lower power levels. The discrepancy between P_{cmd} and P_{AC1} at higher power levels is likely due to error in the active power controller, which will be discussed in the next chapter. Despite these various sources of error, the MPPE method works well overall, maintaining the desired reserve power available for up-regulation.

A second example of MPPE operation is shown in Figure 19, with temperature and irradiance also shown to illustrate the effectiveness of the MPPE method over a wide range of operating conditions. This example was recorded just after a rainstorm on June 25, 2016, cooling the PV modules significantly. Thus the temperature rises by nearly 30 °C over the course of the demonstration. In addition, scattered clouds passed between the PV arrays and the sun the course of the 4.9-hour recording window, causing the irradiance to vary between about 600 and 1100 W/m² repeatedly. The estimated maximum power, P_{MPPE} , tracks close to the measured output power of the SMA inverter, P_{AC2} , as desired. In addition, the measured power of the prototype inverter, P_{AC1} , tracks about 1.1 pu below P_{MPPE} , as desired. As in Figure 18, P_{AC1} is somewhat higher than desired when at lower power levels. This is largely attributed to measurement error due to coupling of harmonics into the AC power measurement; the actual output power of the prototype inverter is closer to the commanded value.

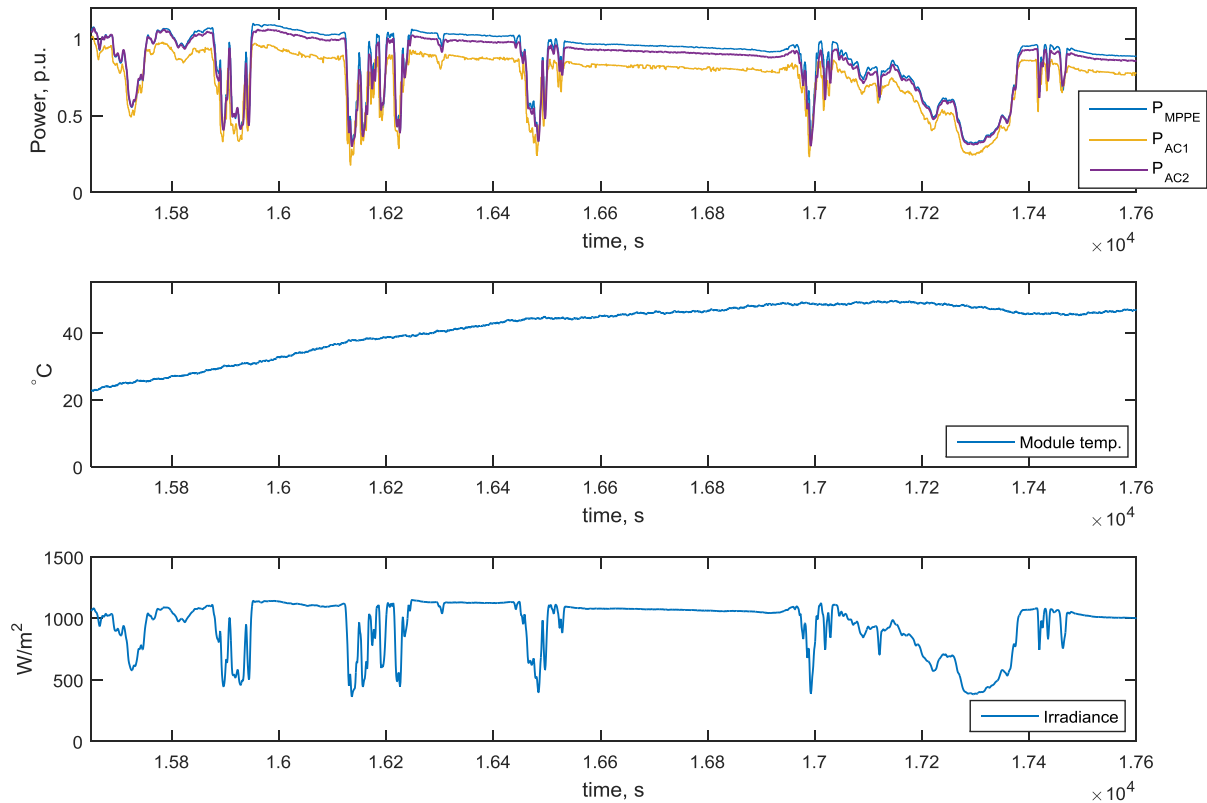


Figure 19. Prototype inverter operating in MPPE mode with a reserve power of 500 W while a second inverter operates in standard MPPT mode, with measured irradiance and temperature recorded.

Figure 20 shows a comparison of the MPPE method proposed here to a simpler method using only irradiance and not temperature. Again the baseline for comparison is the measured output power of an SMA inverter operating in MPPT mode, P_{AC2} , shown in the yellow trace. The estimated maximum power from the MPPE method proposed here, P_{MPPE} , is shown in blue, and an estimate with the PV module temperature measurement fixed at 30 °C, P_{constT} , is shown in red. It is evident that the full MPPE method is significantly more accurate than the constant-temperature method.

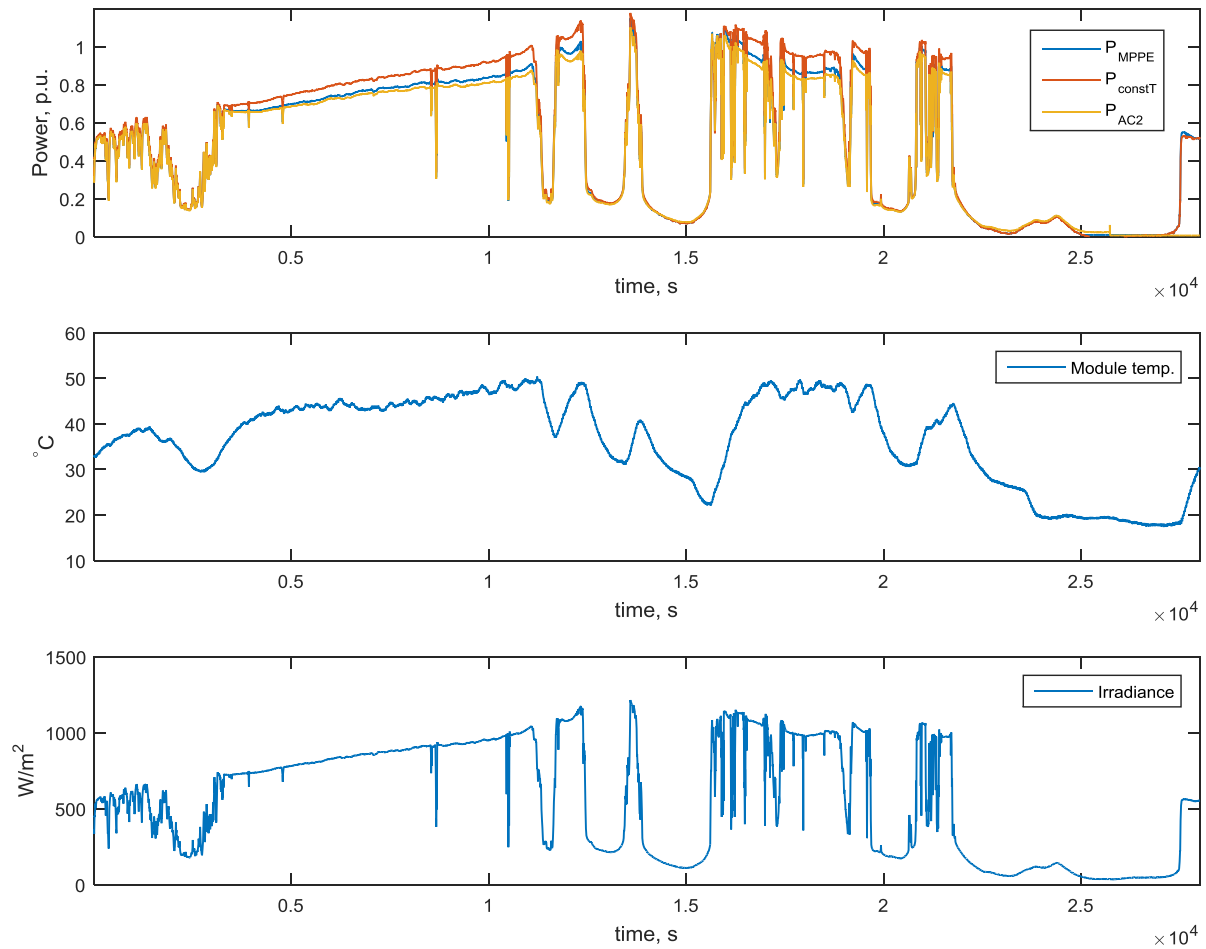


Figure 20. Comparison of the MPPE method proposed here to a simpler method of PV maximum power point estimation based on measured irradiance only.

4 Rapid active power of control PV systems

The previous chapter described a method for estimating the maximum power point of a PV array that can be used in conjunction with any of a number of active power control methods to help regulate or stabilize grid frequency. This chapter presents a novel method of very quickly translating an active power command into a

DC voltage command [92]. That DC voltage command can be passed to a DC voltage controller such as the one implemented in the prototype inverter used here [90], [91].

In many applications of PV active power control, speed of response is crucial. For example, in low-inertia grids such as droop-controlled islanded microgrids and bulk power systems with high proportions of inverter-coupled generation, a PV inverter participating in frequency response must respond as quickly as possible to changes in frequency maintain the frequency within the operating range of the connected devices. Exactly how fast the response must occur will vary from system to system and from event to event, and is a subject of future research discussed in Section 8.2. As an example, the Hawaiian Electric Companies request that resources providing the fastest level of frequency support respond within seven line cycles (117 ms) of an event.

Because a typical PV inverter does not incorporate stored energy above that required to maintain stable operation over a single line cycle (or less), to modulate output power it must regulate its DC input voltage to an appropriate point on the PV array's power voltage (P-V) curve, illustrated in Figure 21. The P-V curve changes continuously with solar irradiance and PV module temperature. In addition, the inverter controller typically has no way of knowing exactly where it is operating on the P-V curve relative to the maximum power point or the open-circuit voltage. The goal of conventional PV inverter design is simply to continuously maximize the instantaneous output power of the system to maximize energy production, a process known as maximum power point tracking (MPPT). For this reason, most of the widely-used methods of controlling output power are heuristic methods such as "perturb and observe", where a the PV array voltage (or current) is perturbed from its operating point, the new operating point is allowed to stabilize,

the change in power is measured, and the operating point is then perturbed again in a direction that depends on whether the power went up or down. This is an inherently slow process, and hence is not appropriate for quickly regulating the output power to a new operating point for fast frequency support.

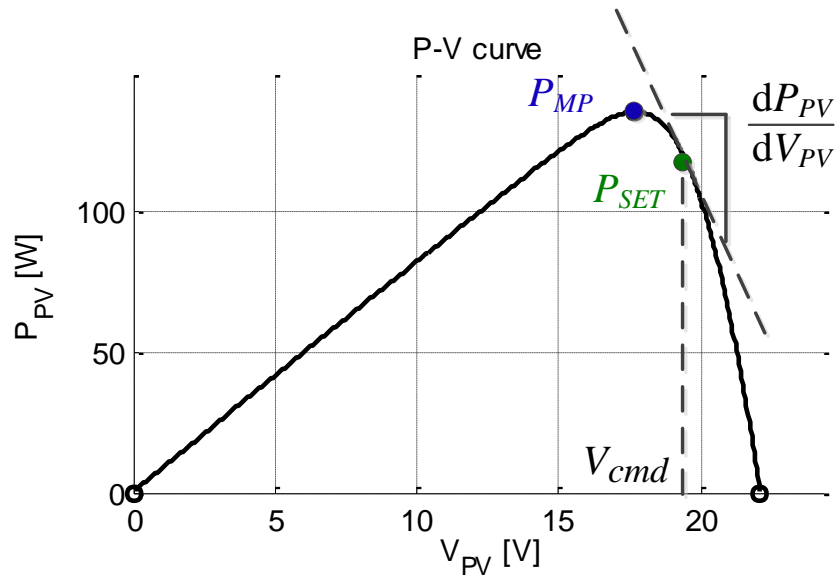


Figure 21. The power-voltage curve of a PV array illustrating a single operating point, P_{SET} , and the voltage V_{cmd} need to achieve that operating point. The local slope of the curve at V_{cmd} is also illustrated.

Several methods to quickly achieve a desired power P_{cmd} were considered. Three methods that were considered and rejected are briefly described in Section 4.1. A fourth method, referred to here as rapid active power control (RAPC), was implemented and is described in Section 4.2. Experimental results demonstrating the use of RAPC in a prototype inverter connected to a PV array are presented in Section 4.3. All four methods operate on the right (high voltage) portion of the P-V curve because this portion of the curve allows all possible power levels to be achieved within a range of voltages that are accessible to most inverter topologies.

The left portion of the P-V curve includes very low voltages (down to zero) that cannot be used by typical single-stage inverters and would be difficult to access even for dual-stage topologies.

Throughout this chapter, as in the previous chapter related to MPPE, a basic underlying assumption is that a PV array is made up of many identical PV modules connected in multiple series strings of equal length. This is true of nearly all PV arrays in the field. It is also assumed that irradiance and temperature are nearly uniform throughout the PV array (or at least the portion of a large PV array that supplies a single inverter). This second assumption is true for most PV arrays larger than a few kilowatts, where shading is not typically present. These assumptions allow PV array power to be calculated by scaling the power of a single PV module by the number of modules in the array. Similarly, PV array voltage can be calculated by scaling the module voltage by the number of modules in each series string. Thus plots of PV module characteristics shown here are indicative of the characteristics of an array made up of similar modules, subject to scaling of voltage and power.

4.1 Candidate active power control methods

The first method of active power control considered here would use the instantaneous slope of the P-V curve, illustrated in Figure 21, to derive a voltage command from a desired power command using the equation

$$V_{cmd} = V_{PV} + \frac{P_{cmd} - P_{PV}}{dP_{PV}/dV_{PV}}. \quad (9)$$

The slope dP_{PV}/dV_{PV} would be estimated periodically by the inverter controller from small perturbations in the operating voltage V_{PV} . This method may be effective in

responding to smaller frequency events that require only a small change in output power, such that the new operating point is in the region where $P_{PV}(V_{PV})$ is well-approximated by its tangent. However, the most crucial frequency events are the largest ones where the inverter would be required to provide all or nearly all of its reserve power to the grid. These are events where a response based on a small-signal approximation of the P-V curve will be highly inaccurate, significantly underestimating required change in voltage for underfrequency events, and overestimating for overfrequency events.

The next method considered for converting a power command quickly and accurately into a voltage command is similar to the MPPE method from Section 3.1 in that linear regression is used to derive a second-order polynomial to simplify the control task. Visually, it appears from Figure 22 that the right (high voltage) portion of the P-V curve could be well-approximated by a second-order polynomial (i.e. a concave-down parabola).

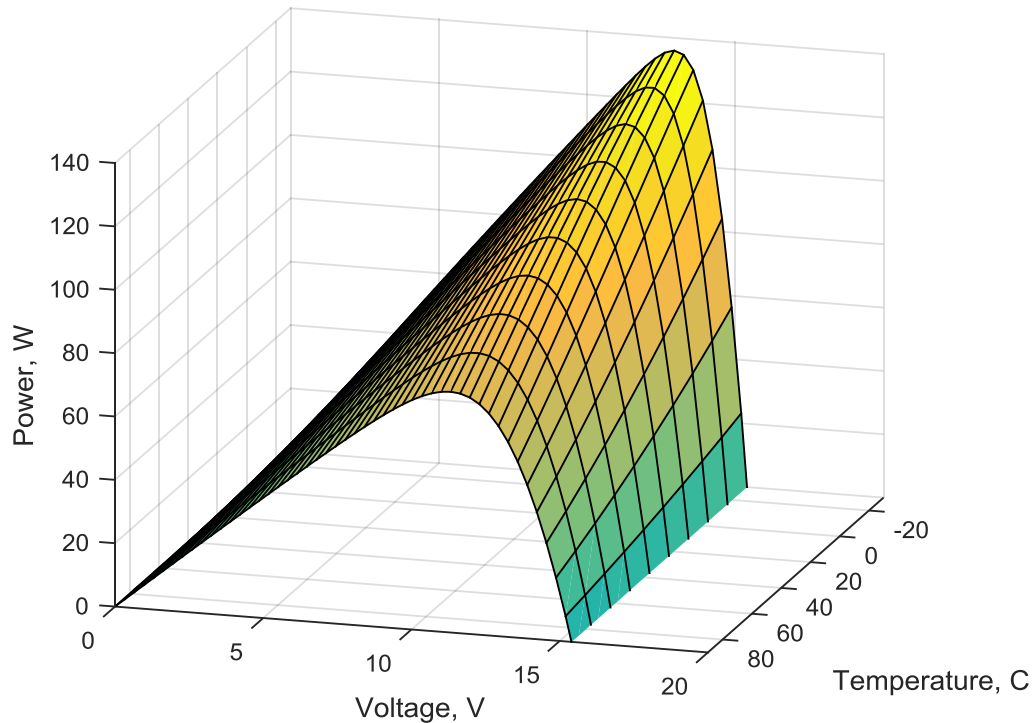


Figure 22. Power-voltage curves of the Solarex 110S PV module as a function of PV cell temperature, at nominal irradiance (1000 W/m^2).

Thus it was desired to find a polynomial g_2 such that $g_2(V_{PV}, G, T) \approx P_{PV}(V_{PV}, G, T)$ and store that polynomial in the inverter controller to allow online estimation of the power P_{PV} that would result from a given voltage V_{PV} , based on measured irradiance and temperature. It would then be possible to solve a quadratic equation to find the desired voltage operating point. Using a model of the Solarex 110S PV module derived from data sheet parameters using Villalva's numerical method [75], [93], P_{PV} was calculated for discrete values of T , G , and V_{PV} equally spaced throughout the operating range of a PV module in the field: $T = \{-20 \dots 80\} \text{ }^\circ\text{C}$, $G = \{50 \dots 1200\} \text{ W/m}^2$, $V_{PV} = \{V_{mp}(T, G) \dots V_{oc}(T, G)\}$. Equation (10) was defined (where all lower-case letters are regression coefficients), and linear regression was used to solve for the coefficients, using the Solarex model data.

$$P_{PV} = a + b_1T + b_2G + b_3V_{PV} + b_4T^2 + b_5G^2 + b_6V_{PV}^2 + b_7TG + b_8TV_{PV} + b_9GV_{PV} \quad (10)$$

Variants of equation (10) with a subset of the terms were also investigated. For all linear regression solutions for equation (10) and its variants, the lowest RMS error between the model and the input data was 7.3 W, or 6.6% for the 110 W PV module. This error was deemed too large to result in acceptable performance. In attempt to obtain a better fit, the size of the (T, G) operating region was reduced to eliminate regions that would rarely occur in practice: the ranges $T = \{10...70\}$ °C and $G = \{100...1000\}$ W/m² were used. This indeed reduced the RMS error of the model, to 1.68 W for the best variant of equation (10). However, the low RMS error masked unacceptably high error in certain cases; as shown in Figure 23, the residual error is over 6 W in a significant number of cases. Thus this method was set aside.

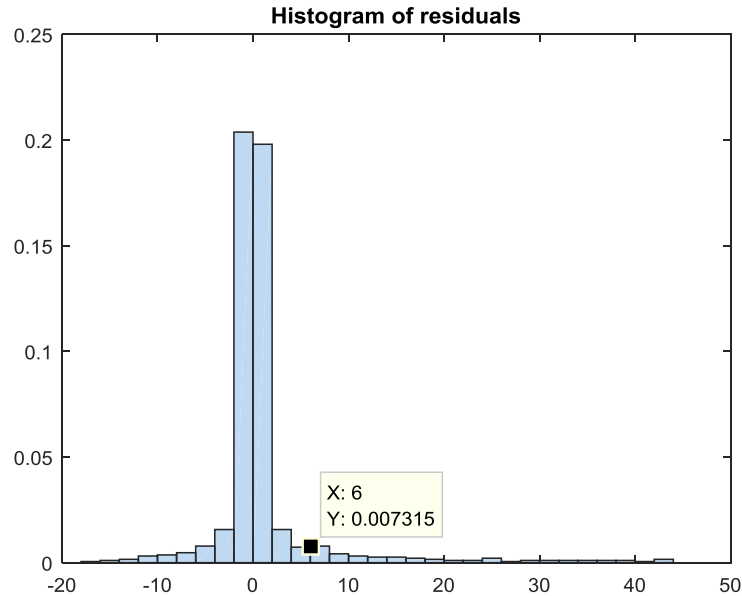


Figure 23. Histogram of residuals (errors between polynomial regression model and actual nonlinear PV model) for the lowest RMS error variant of equation (10).

Another regression-based method was also investigated. This method involved finding an equation g_3 such that $V_{PV} \approx g_3(P_{PV}, G, T)$ throughout the expected operating space. Because g_3 could be used to convert a desired power P_{cmd} directly into a voltage command V_{cmd} for a given measured G and T , higher order polynomials could potentially be used for g_3 than could be used for g_2 in equation (10). Various candidate polynomials were created, again using linear regression of input data produced numerically from a 5-parameter PV model of the Solarex 110S module. The candidate polynomials ranged in order from 3rd to 7th. The best RMS error obtained was 0.59 V, or 3.6% of the nominal Solarex PV module maximum power voltage. This error was again deemed too large to result in acceptable performance, especially given that the resulting percentage error in power output will be larger than the error in voltage given the steep slope of voltage across much of the operating region, and the fact that regression model error will be one of several sources of error in a functioning inverter. Thus this method was also set aside.

4.2 Rapid APC (RAPC) method

Given the challenges encountered with other methods, it was decided to instead produce a three-dimensional lookup table (LUT) to be stored in the inverter and used to estimate the value of V_{cmd} that will produce a desired power output: $V_{PV} = g_3(P_{PV}, G, T)$. This LUT should cover the entire expected operating range of power, module temperature, and irradiance. The LUT can be interpolated using trilinear interpolation to reduce the size of table needed to give a desired accuracy. Even so, the size of the LUT in each dimension was carefully considered with a goal of producing an accurate table with a tractable size. Because the LUT is three-dimensional, it can easily become very large.

In the temperature and irradiance dimensions, the granularity of the LUT can be somewhat coarse because the gradients dV_{PV}/dT and dV_{PV}/dG are relatively smooth throughout the operating space. This can be observed in Figure 24, and is also somewhat intuitive: as module temperature or irradiance increases, one would not expect highly non-uniform changes in a PV module's P-V curve.

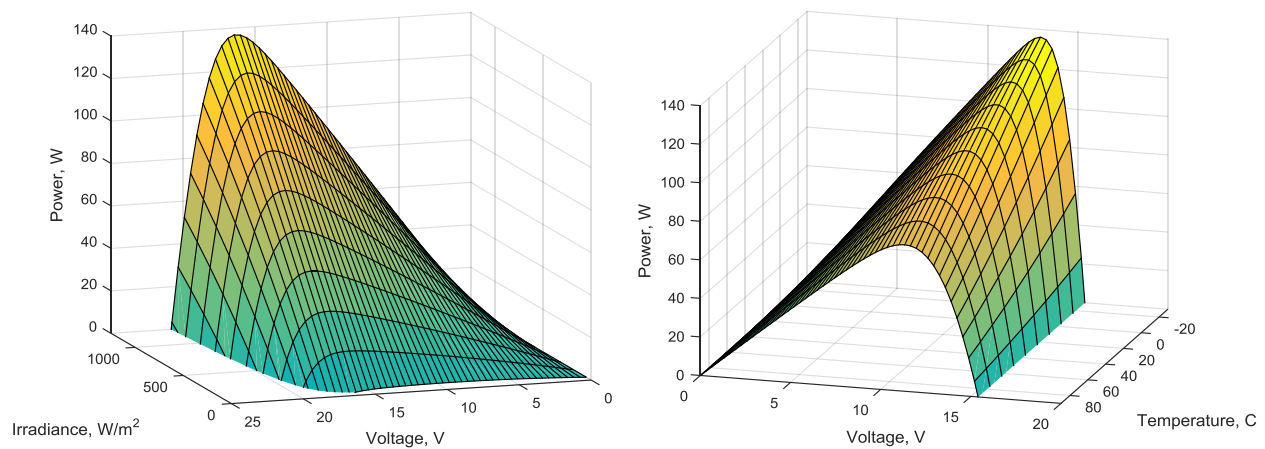


Figure 24. PV power as a function of irradiance and voltage at constant cell temperature (left), and as a function of cell temperature and voltage at constant irradiance (right).

In contrast, the gradient dV_{PV}/dP_{PV} is at times fairly small and approaches (negative) infinity as V_{PV} approaches the maximum power voltage V_{mp} . This is illustrated in Figure 25, again based on the Solarex 110 S module. Thus the LUT requires a higher granularity in the P_{PV} dimension.

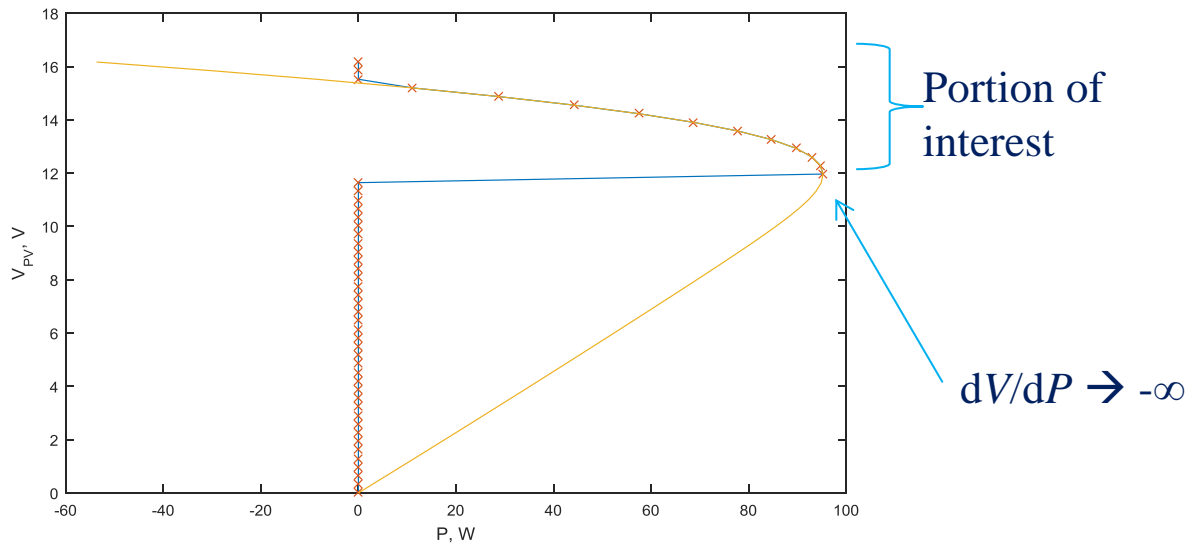


Figure 25. PV module voltage needed to produce a desired power (yellow trace), at a fixed cell temperature and irradiance.

For any commanded power level greater than $P_{mp}(G, T)$, the LUT should return V_{mp} , the voltage that will produce the highest power available from the PV array. This desired behavior is illustrated by the red Xs in Figure 26. The red Xs also provide a visual indication of the LUT resolution needed in the P_{PV} dimension to accurately represent the PV array voltage-power characteristic: Figure 26 uses 100 evenly spaced power data points.

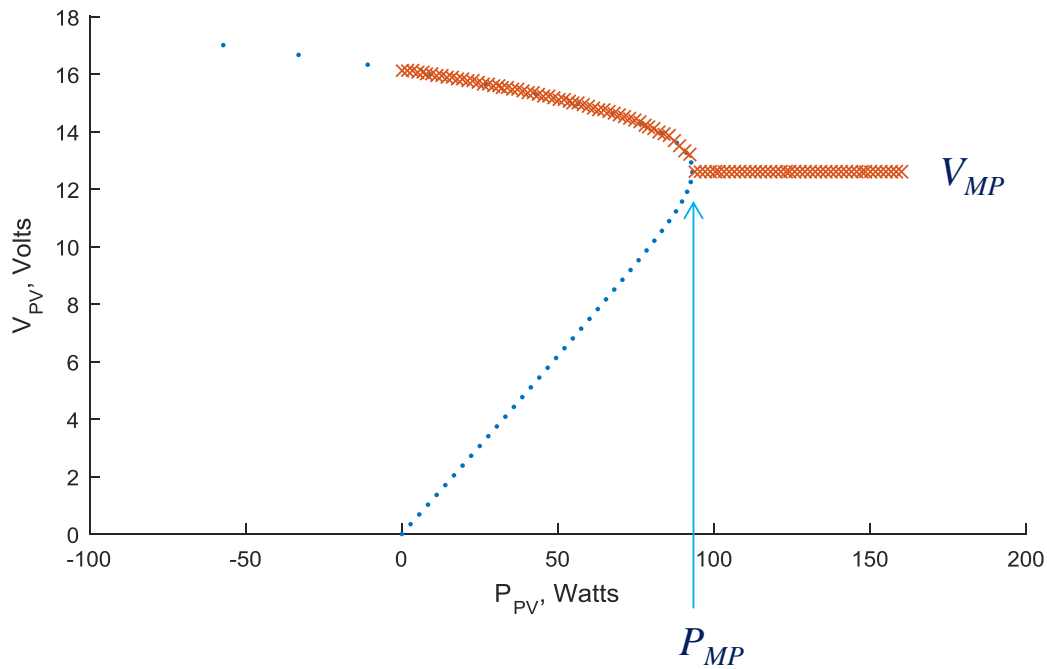


Figure 26. Desired lookup table output (red Xs), and PV module voltage-power relationship (blue dots).

One might conclude from Figure 26 that the LUT could be designed to have high resolution only near the maximum power point, with lower resolution other operating points. However, as irradiance and temperature change, the location of the maximum power point varies widely. For example, Figure 27 shows an extreme case of very low irradiance. Thus the LUT should have fairly high granularity across all power operating points.

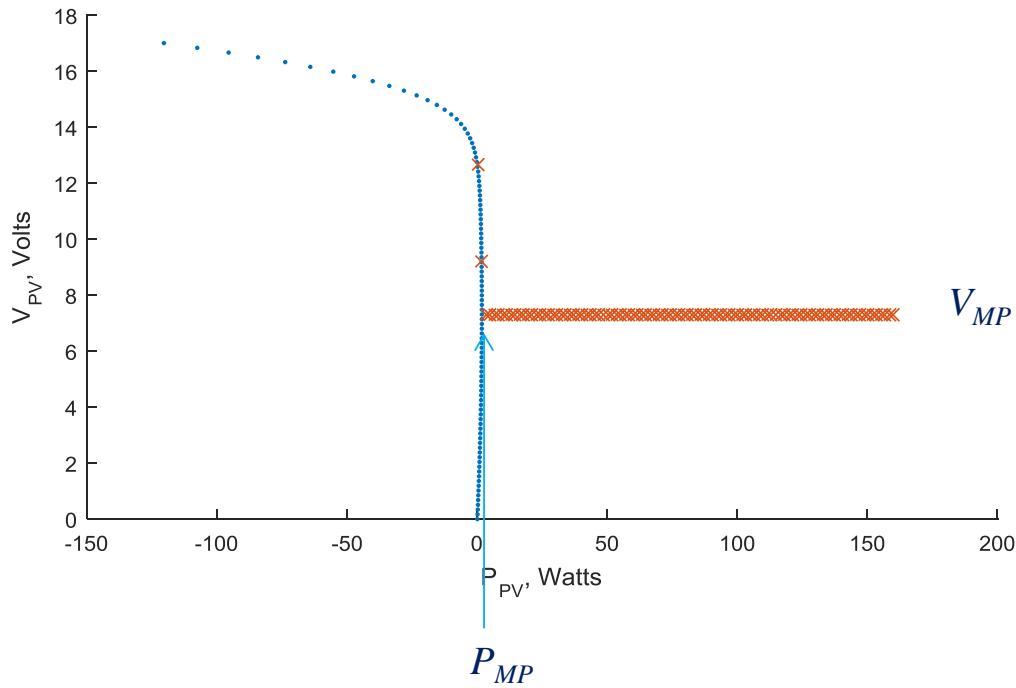


Figure 27. Desired lookup table output (red Xs), and PV module voltage-power relationship (blue dots) at very low irradiance.

The lookup table data is generated by solving a five-parameter PV array model at various operating points. The process for generating the LUT is summarized in Figure 28. Like the MPPE equation generation process, the process for generating a LUT for rapid active power control is performed once offline starting from PV module data sheet values, and the LUT is stored in the inverter controller for online use. The process contains four steps:

The first two steps in the LUT generation process are identical to the first two steps of the process for finding the regression coefficients for MPPE, as described in Section 3.1. To summarize, PV module data sheet parameters are used as input to a numerical method ([75]) to calculate the parameters of a five-parameter PV cell model. The five-parameter model (shown in equation (3) and

Figure 8) and is then numerically solved to find the PV current I_{PV} at each voltage V_{PV} for an array of (G, T) pairs \mathbf{X} representing the operating region of the PV system.

In the third step of the LUT generation process, the power P_{PV} at each operating point is calculated by multiplying I_{PV} by V_{PV} . The result of this process is a three dimensional array of powers P_{PV} for any given irradiance, module temperature, and voltage.

In the fourth step, the $P_{PV}(V_{PV}, G, T)$ data from step 3 is interpolated using cubic splines to produce $V_{PV}(P_{PV}, G, T)$ values. Only the data for voltages greater than or equal to the maximum power voltage V_{MP} are used in the cubic spline interpolation. For all power commands greater than the maximum power for a given irradiance and temperature, the LUT returns V_{MP} . This is expressed mathematically in equation (11).

$$\mathbf{V}_{\text{PV,LUT}} = \left\{ \begin{array}{ll} \max_k (I_{PVijk} \cdot V_{PVijk}) & \forall P_{PVijk} \geq P_{MPij} \\ V_{PV,spline}(P_{PVijk}, G_i, T_j) & \forall P_{PVijk} < P_{MPij} \end{array} \right\} \quad (11)$$

As in Section 3.1, the subscripts i , j , and k represent the indices of vectors of irradiance, module temperature, and voltage, respectively. $V_{PV,spline}$ is generated from cubic spline interpolation of the \mathbf{P}_{PV} array onto 100 evenly spaced voltage points. Matlab's `spline()` function was used to perform the interpolation. The result is a three-dimensional array $\mathbf{V}_{\text{PV,LUT}}$ spanning all possible values of power, irradiance, and module temperature in the operating space.

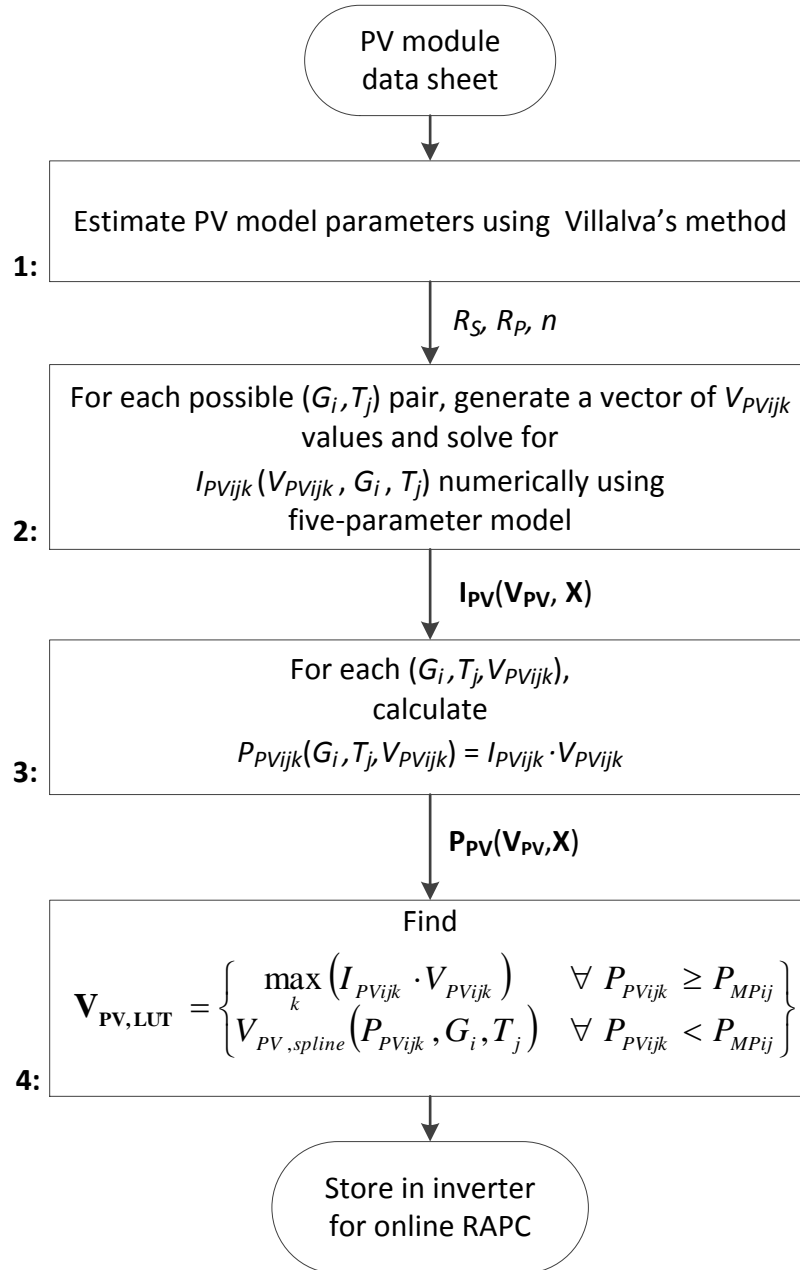


Figure 28. Process for generating a lookup table for use in rapid active power control of PV systems.

An initial LUT was generated containing 100 points in the P_{PV} dimension and 10 points each in the G and T dimensions. A “slice” of the LUT at constant temperature is shown on the top plot in Figure 29. Some artifacts are present near

the maximum power region (the crease of the surface), so the resolution in G was increased by five times. The bottom plot in Figure 29 shows a new LUT with 50 data points in the G dimension.

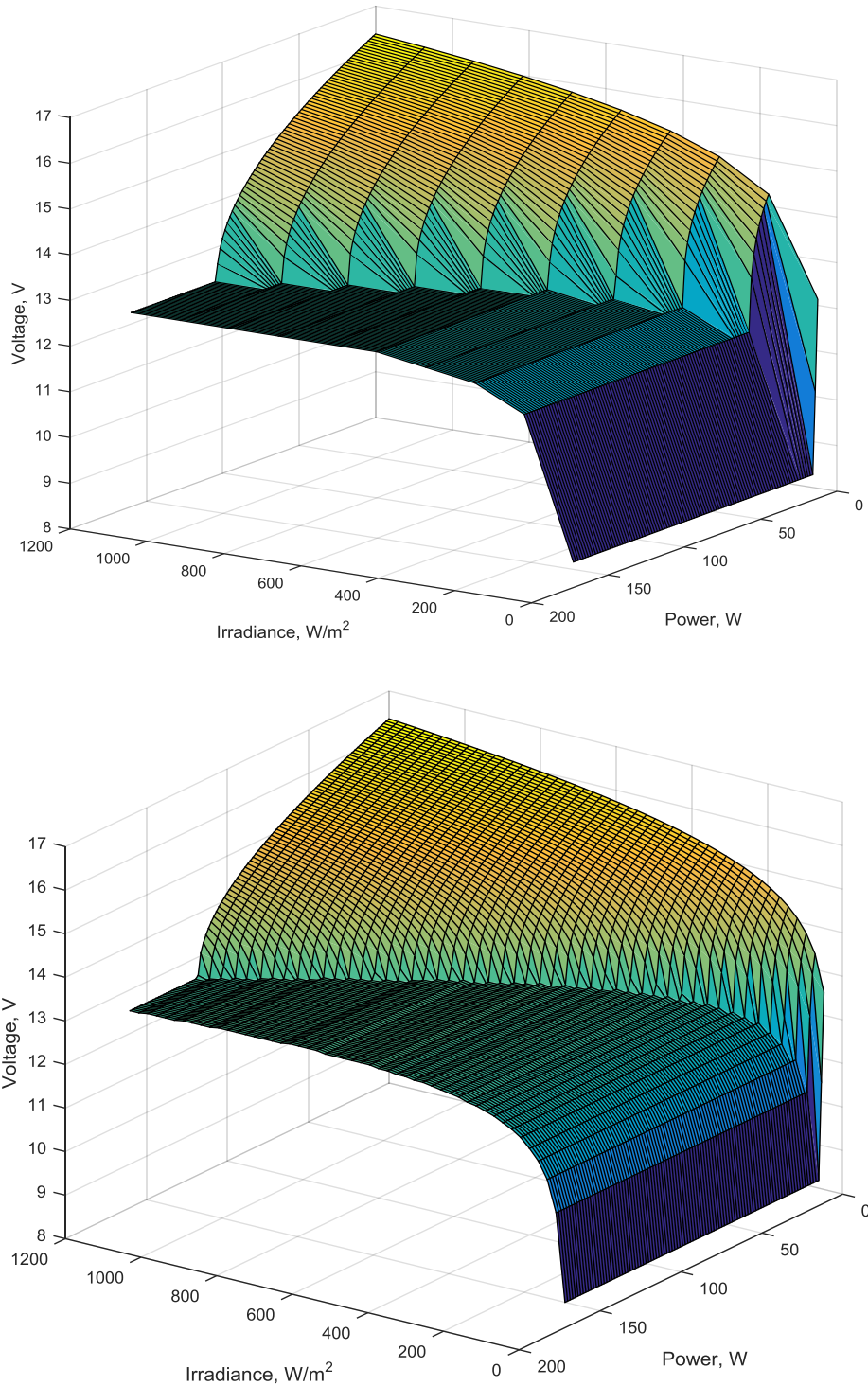


Figure 29. Selecting $V_{PV}(P_{PV}, G, T)$ LUT resolution in irradiance dimension. The top plot includes 10 irradiance data points, and the bottom plot contains 50. Both are plotted a constant temperature of 47 °C.

A similar process was used to size the LUT in the T dimension. The top portion of Figure 30 shows a “slice” of the LUT at constant irradiance with 10 temperature data points. Again, some artifacts are present in the crease of the surface near the maximum power region. The number of temperature data points was increased to 30 for the plot in the bottom portion of Figure 30, resulting in a smoother surface, especially near the maximum power region.

The final LUT, as implemented, was $100 \times 50 \times 30$ ($P_{PV} \times G \times T$), for a total of 150,000 values. When stored as double precision floats in the LUT takes 1.1 MB of space. Lower precision could be used without sacrificing accuracy. However, the sbRIO controller used here has plenty of storage memory, so the full 1.1 MB LUT file was used. The LUT was generated for the Solarex 110S PV module previously described because a PV array consisting of such modules was available for experimental demonstration. The values were calculated in Matlab, stored as 30 CSV files, and imported into a LabView VI. The VI was programmed to store the LUT data in a LabView binary file (which still had a size of 1.1 MB), and the binary file was loaded onto the sbRIO.

The LUT interpolation and surrounding logic and controls were implemented in LabView Real-Time in a 50 ms timed loop. It is likely that a faster loop could be used for increased response time, though a loop faster than about one AC line period (17 ms) would not increase response time further. A LabView implementation of trilinear interpolation [94] was used in the sbRIO to provide increased accuracy between LUT data points. The input power command to the LUT was scaled down from the measured power by dividing by the number of PV modules in the array, and the output voltage from the LUT was scaled up by multiplying by the number of modules in each series string.

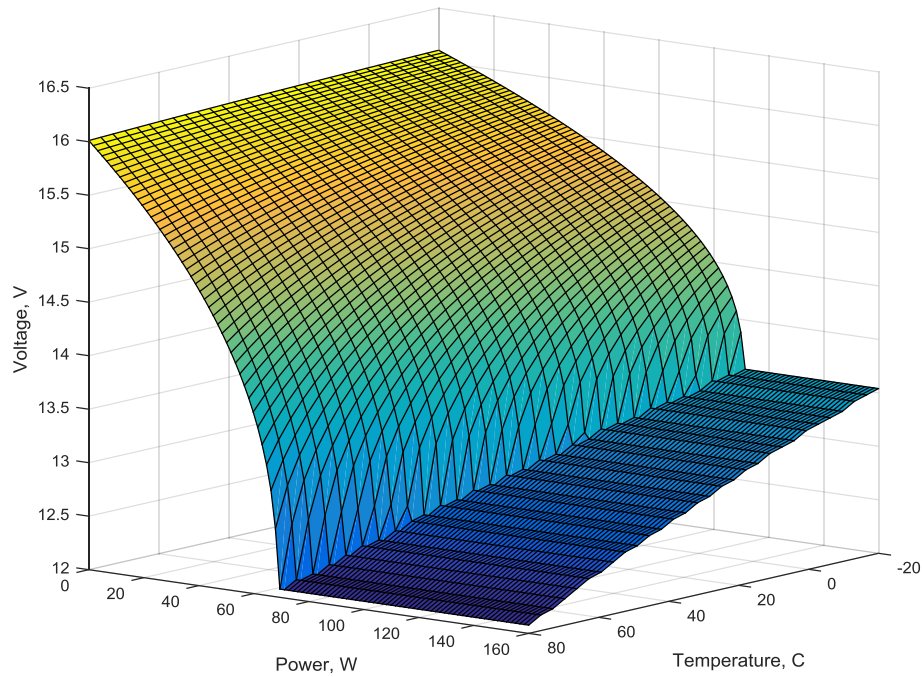
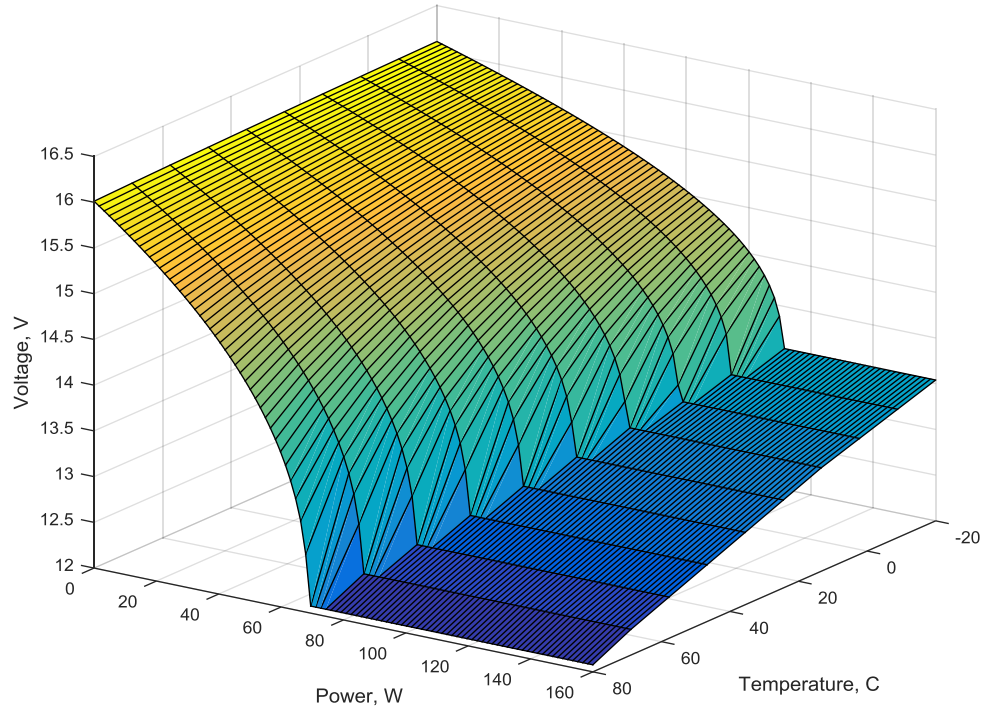


Figure 30. Selecting $V_{PV}(P_{PV}, G, T)$ LUT resolution in temperature dimension. The top plot includes 10 temperature data points, and the bottom plot contains 30. Both are plotted a constant irradiance of 843 W/m^2 .

An overview of the proposed control is shown in Figure 31, and the next section presents an experimental validation of RAPC and MPPE.

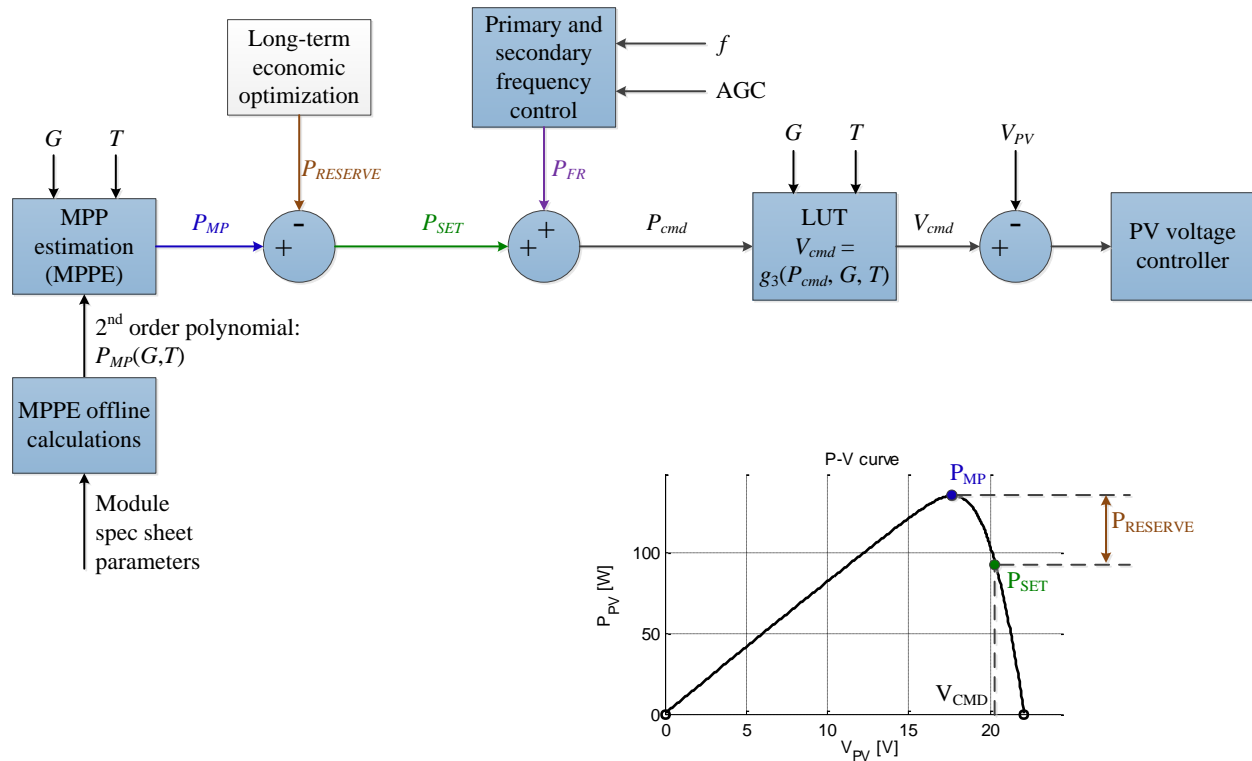


Figure 31. Control overview showing MPPE and lookup table for rapid active power control.

4.3 Experimental demonstration of MPPE and rapid APC

A prototype inverter with MPPE and a LUT for rapid APC was used to validate the RAPC method. The test setup diagram was the same as that used for MPPE validation and is repeated in Figure 32 for the convenience of the reader. The grid simulator in the test setup was programmed to produce a variety frequency events and the inverter's response was recorded using a Yokogawa

PZ4000 power analyzer. The PZ4000 recorded voltage and current waveforms, and the waveform data was post-processed to calculate frequency, real power, and other quantities. The sbRIO controller also recorded its internal control signals during the tests. The data files were synchronized so that control signals and measured signals could be plotted on the same time axes. Examples of responses to three frequency events are presented here.

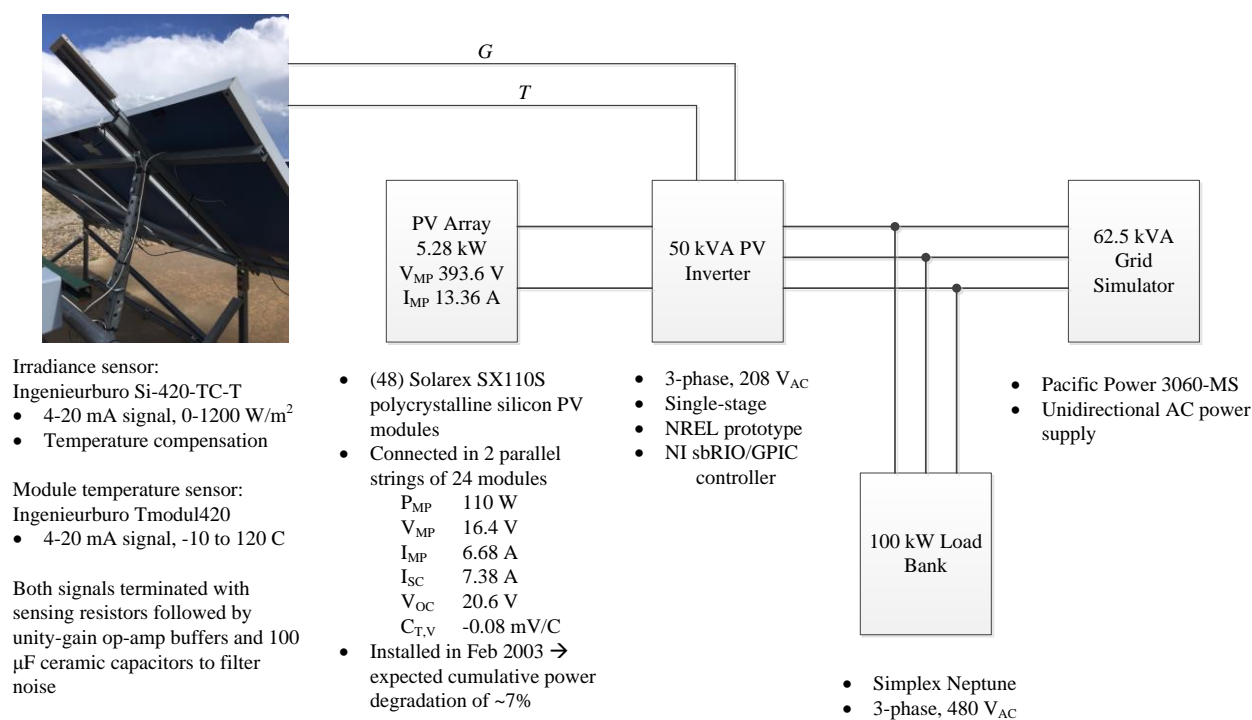


Figure 32. Rapid active power control experimental setup.

To ensure that the prototype inverter could respond to realistic frequency events, the programmed events were designed to mimic the magnitude and rate of change of frequency (ROCOF, or df/dt) that may be seen on real power systems. Current draft of IEEE Standard P1547 are considering requiring DERs to remain connected during frequency events with a ROCOF of 1 to 3 Hz per second,

depending on the type of DER [83]. Smaller interconnected AC power systems tend to have more severe frequency events, both in magnitude and in ROCOF. For example, in studies that simulated a separation of the Ireland and Northern Ireland electrical systems a ROCOF of over 1 Hz per second was observed in Ireland, and a ROCOF of over 2 Hz/s was observed in Northern Ireland [95]. In terms of magnitude, a frequency event with a minimum frequency (nadir) of 59 Hz would be considered a very large event in the continental U.S., but on the most populous Hawaiian island of Oahu, such events occur more than once per year in recent years. Overfrequency events tend to be less severe in terms of both magnitude and ROCOF. The frequency events used in the tests below were designed with these considerations in mind.

Figure 33 shows the prototype inverter's response to a frequency event with a nadir of 59 Hz and a ROCOF of 2 Hz/s, faster than what would be seen on a large interconnected power system but possible for a system such as Ireland's. The inverter was operating in MPPE mode with 0.8 kW of power in reserve and a 5% droop slope (meaning that a frequency change equal to 5% of the nominal frequency, or 3 Hz, will result in a change of 100% of the inverter's nominal power). A 5% droop slope is a common value used in synchronous machines providing primary frequency regulation, though the machine response is orders of magnitude slower than the inverter response shown here. The programmed droop slope did not contain a deadband, as is common with conventional generators, but it could easily be modified to incorporate a deadband. The PZ4000 frequency trace and the inverter's internal frequency measurement (labeled "NI data" in the frequency plot) were used to synchronize the test data from the two recording devices. The inverter begins responding to the frequency event almost immediately. Both the measured DC voltage V_{PV} and the measured AC power P_{AC} track closely their respective

commanded values, V_{cmd} and P_{cmd} . The AC power of course does not exceed the estimated maximum power available, P_{MPPE} , providing further validation of the MPPE method. The high frequency component of the DC voltage measurement is a combination of measurement noise, switching frequency ripple, and DC voltage ripple at a multiple of the line frequency (likely due to a slight imbalance between phases). Figure 34 zooms in on the initial part of the frequency event to show that the measured power lags the commanded power by less than 20 ms.

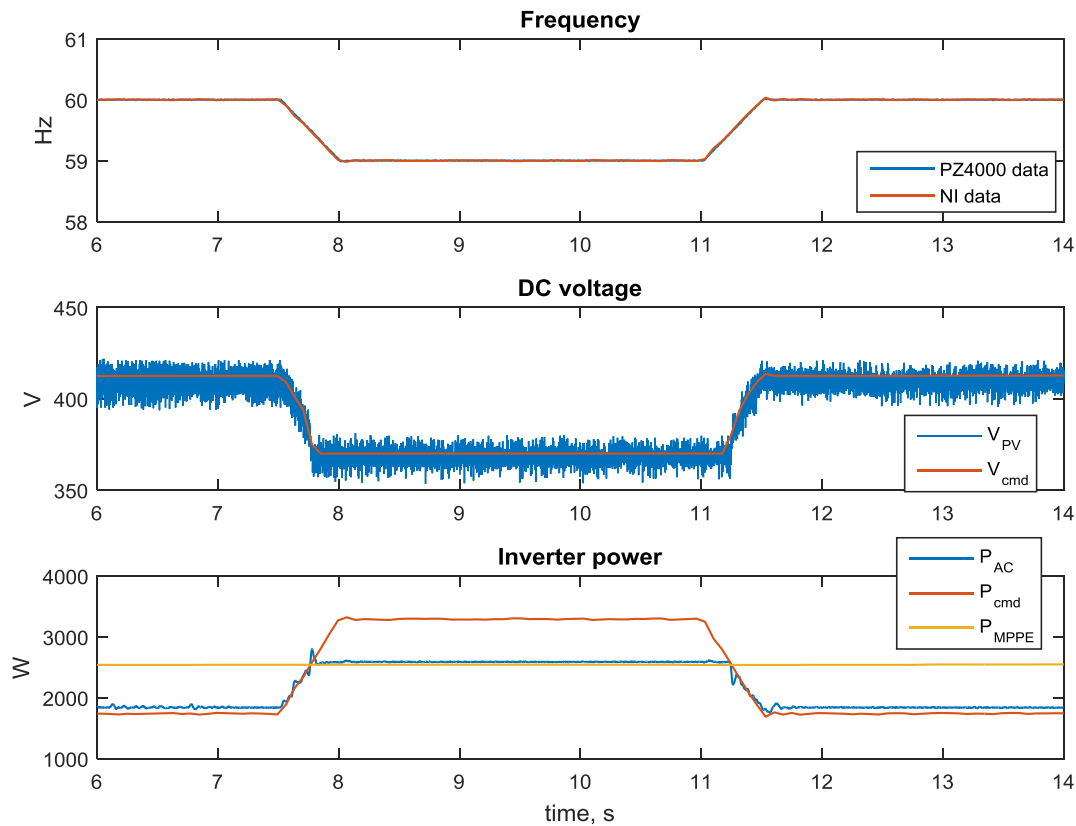


Figure 33. Response of the prototype inverter to a frequency event with a nadir of 59 Hz and a 2 Hz/s ROCOF.

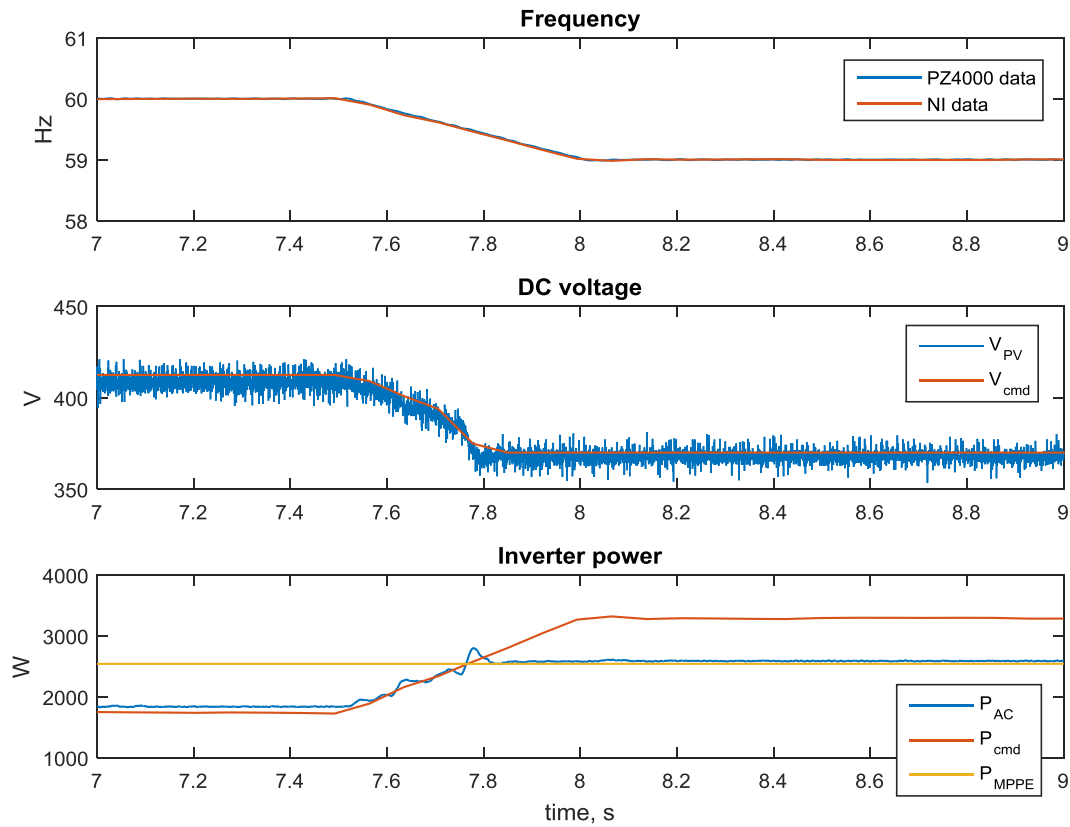


Figure 34. Zoomed in response of the prototype inverter to a frequency event with a nadir of 59 Hz and a 2 Hz/s ROCOF.

The inverter's response to an overfrequency event is shown in Figure 35, and Figure 36 shows a zoomed in view of the initial part of the same event. The inverter was programmed with 1 kW of power reserve and a 5% droop slope with no deadband. The inverter's response again tracks the commanded values well with little delay, as desired.

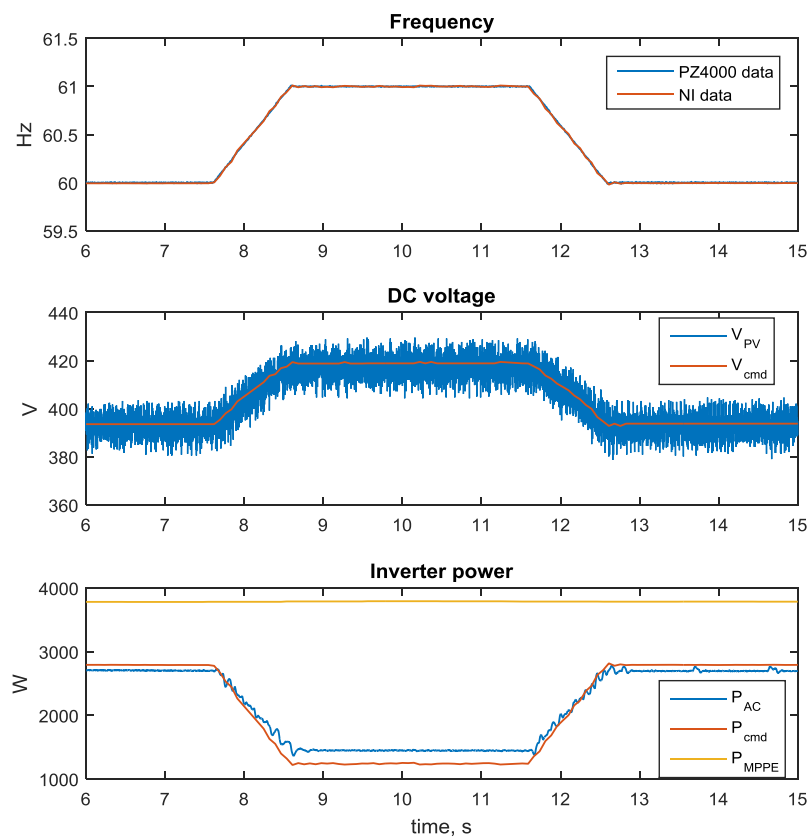


Figure 35. Response of the prototype inverter to an overfrequency event peaking at 61 Hz with a 2 Hz/s ROCOF.

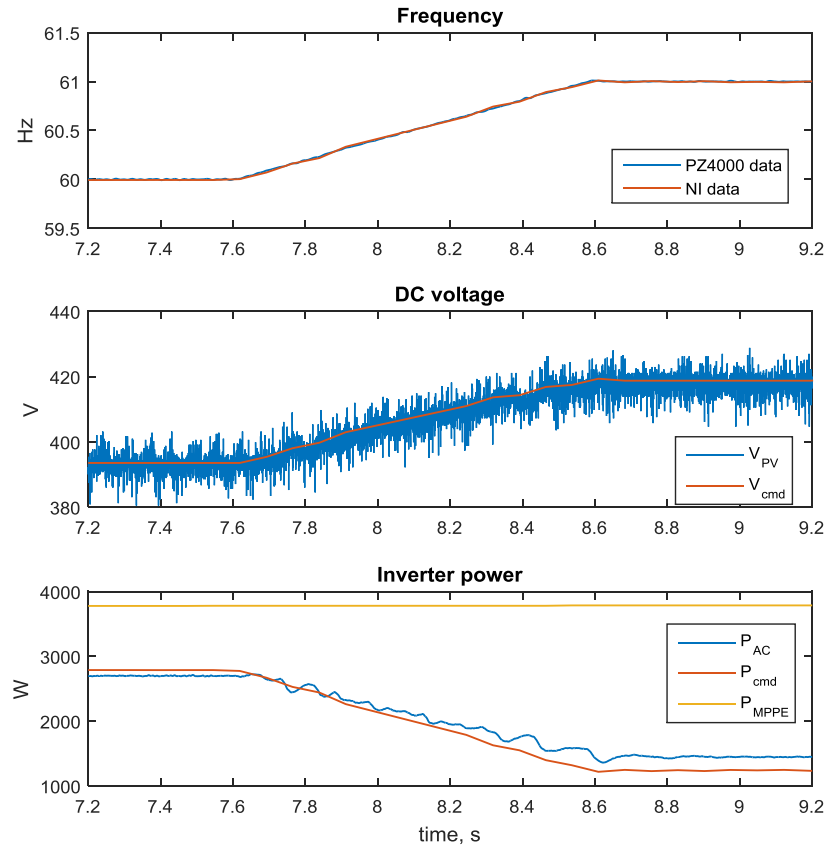


Figure 36. Zoomed in response of the prototype inverter to an overfrequency event peaking at 61 Hz with a 2 Hz/s ROCOF.

The inverter's response to an underfrequency event with a very fast ROCOF of 6 Hz/s is shown in Figure 37, with the initial part of the event magnified in Figure 38. The inverter was again programmed with a 5% droop slope, and a reserve power of 0.8 kW. The inverter responds well. However, the limitations of the inverter's response become evident in the magnified figure. There is visible overshoot and some ringing in P_{AC} . The oscillations die out quickly and are not large in magnitude relative to the response, so it is expected that such a response would still be effective in mitigating frequency events, but they do indicate that this high-ROCOF event is near the edge of the inverter's response capability. However,

it will likely be possible to improve the bandwidth of this early prototype without compromising stability, as discussed in Section 8.2.

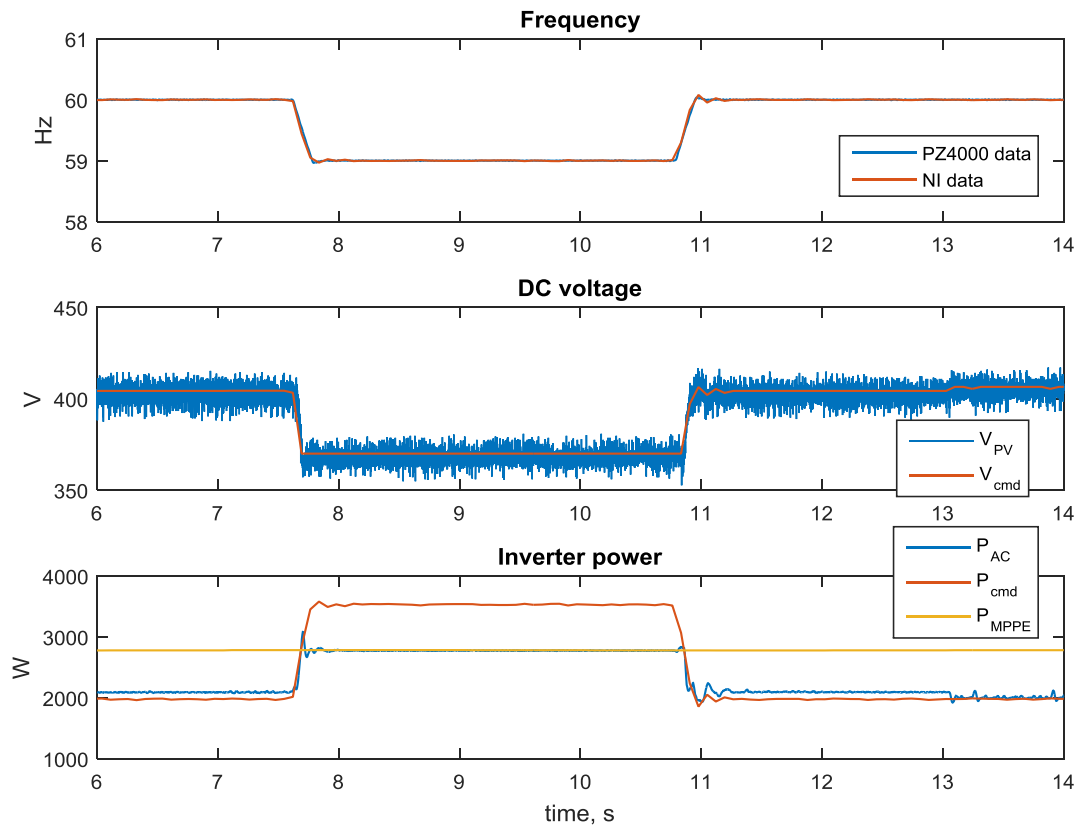


Figure 37. Response of the prototype inverter to a frequency event with a nadir of 59 Hz and a 6 Hz/s ROCOF.

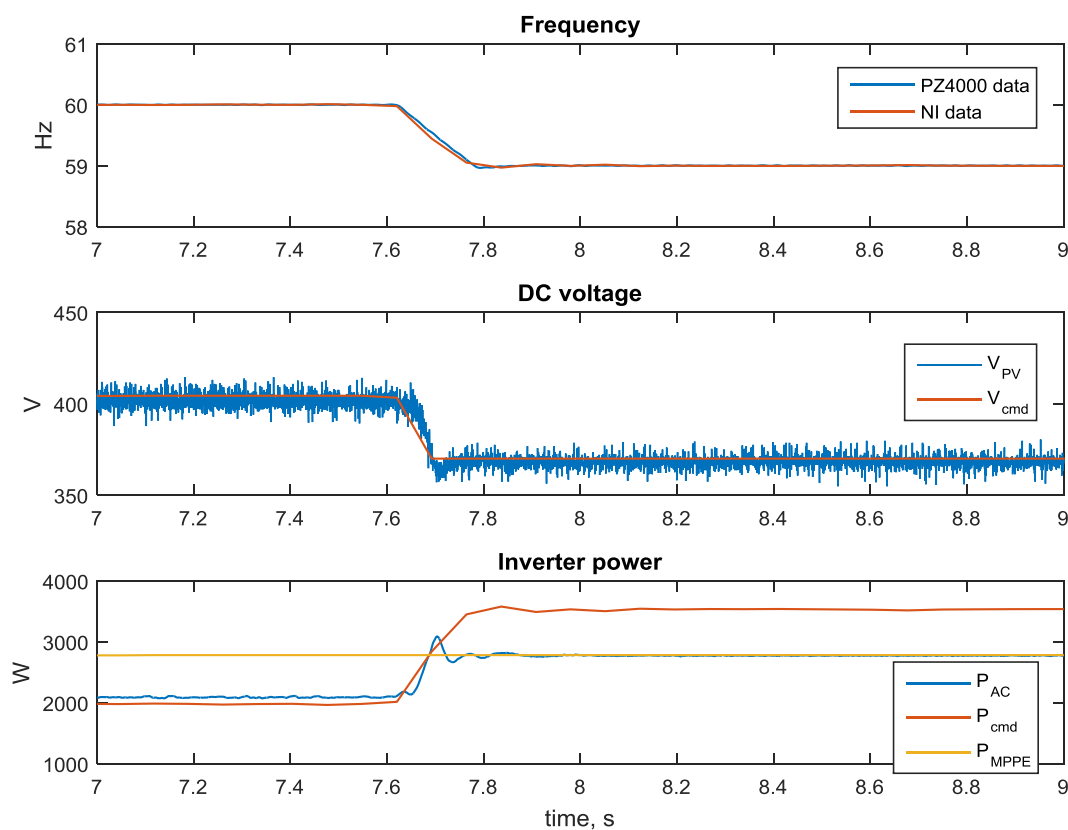


Figure 38. Zoomed in response of the prototype inverter to a frequency event with a nadir of 59 Hz and a very fast 6 Hz/s ROCOF.

Some power systems see frequency events that are larger in magnitude than those shown above. For example, some contingency events on Oahu have had nadirs below 58.5 Hz. These events have typically had ROCOFs around or just below 1 Hz/s. The response of the inverter to a test representing such an event is shown in Figure 39, and a magnified view of the beginning of the event is shown in Figure 40. The inverter had a reserve power of 1.2 kW and a more aggressive droop slope of 3%, representing the steeper end of the range of droop slopes typically used in synchronous machines. Recall that droop slope is defined as the percentage

change in frequency that leads to a change in generator power of 100% of the unit's rating, so smaller droop slopes lead to a more aggressive response. Again the inverter's response is fast and accurate. Note that due to the steepness of the droop slope and the size of the event, the power command goes much higher than the inverter's rating. Thus the effect of the higher droop slope in this case is to deploy the PV system's reserves faster, rather than to change the maximum power reached.

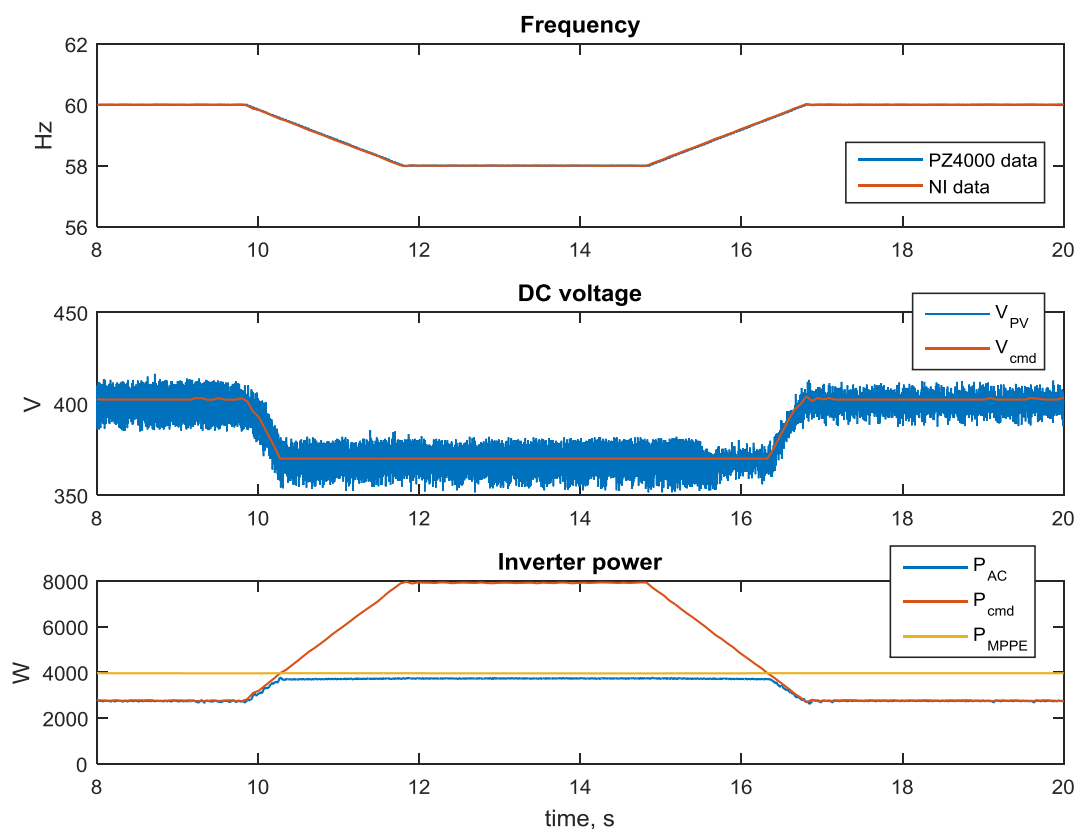


Figure 39. Response of the prototype inverter to a frequency event with a lower nadir of 58 Hz and a 1 Hz/s ROCOF.

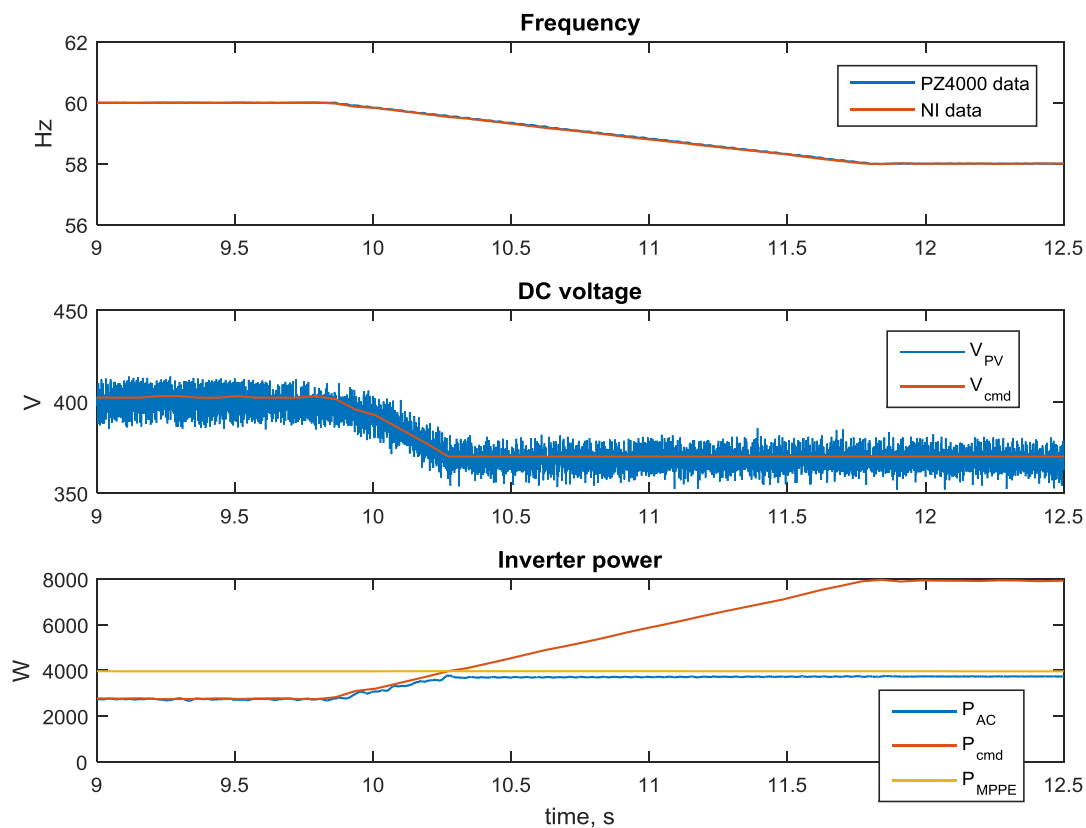


Figure 40. Zoomed in response of the prototype inverter to a frequency event with a lower nadir of 58 Hz and a 1 Hz/s ROCOF.

Based on the tests presented above and other similar tests, it was concluded that the rapid active power control method proposed here provides a fast and accurate response that is expected to be effective in mitigating frequency events. Typical events on the U.S. bulk power system are much less severe (e.g. ROCOF of 0.25 Hz/s), so the prototype inverter would be quite capable of providing a fast, accurate, and stable response. Combined with the maximum power point estimation method presented here, RAPC is expected to enable a suite of fast frequency support services from PV systems. The examples shown above have used

droop response, but both MPPE and RAPC can be used to enable any number of methods of fast frequency support, such as synthetic inertia or “fast frequency response”. This concludes Part I of this thesis on active power control of PV systems. A summary of contributions and some proposed next directions in APC of PV systems are described in Section 8.2, which follows Part II: Degradation-aware electric vehicle charge optimization.

**Part II: Degradation-aware electric vehicle
charge optimization**

5 Overview of degradation-aware charging (DAC) of electric vehicle batteries

As electric vehicles (EVs) and plug-in hybrid electric vehicles (PHEVs) are commercialized, interest has grown in predicting the effect such vehicles will have on electric power system infrastructure, and mitigating any negative effects [49], [96], [97]. A proposed method of reducing stresses on grid infrastructure due to EV charging involves encouraging vehicles to charge at off-peak times through time-based electricity pricing [96], [98]–[101]. For a vehicle to respond to price signals, some degree of intelligent charge control is required. Such charge control could, for example, be implemented as part of an on-board vehicle charger or electric vehicle supply equipment (EVSE), provided that the algorithms involved are not prohibitively complex for embedded processing. Chapter 6 presents a relatively simple method of charge power control that optimizes not just the cost of energy, but also the equivalent estimated cost of battery degradation, as shown conceptually in Figure 41. This degradation-aware charging (DAC) method was first introduced in [30] and was elaborated upon in [102]. Several additional works by other authors mentioned below have since proposed similar and related methods.

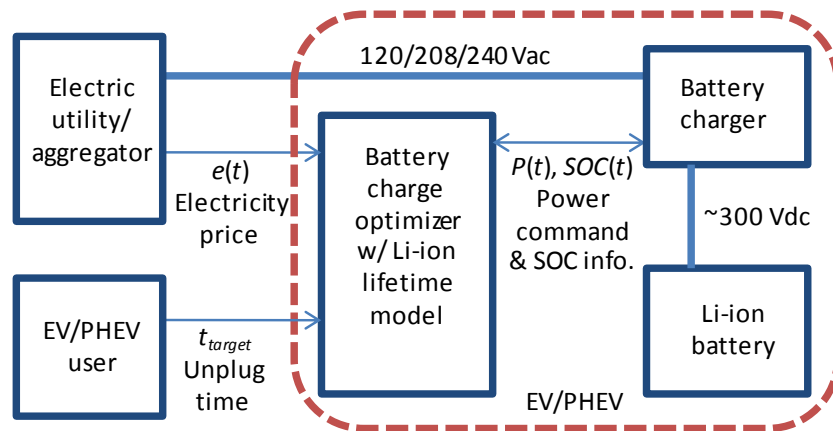


Figure 41. EV/PHEV charge optimization diagram. The charge optimization algorithm can be implemented on the controller of the on-board EVSE.

Accounting for battery degradation during charge optimization is important because lithium-ion (Li-ion) batteries represent a major component of vehicle cost [103]–[107]. Finding the minimum battery size that meets vehicle energy capacity and power output requirements presents an opportunity to reduce vehicle cost significantly. Here, energy capacity is defined as the maximum energy available from a fully charged battery, and is often referred to simply as “capacity.” The temperatures at which a battery is charged and the state of charge (SOC) as a function of time have significant effects on battery life [106], [108]–[113]. Therefore, an intelligent charge algorithm capable of estimating and minimizing these effects can potentially extend battery life. A vehicle equipped with a charger that minimizes the effects of charging on battery life can potentially be equipped with a smaller, less expensive battery while still meeting battery capacity and power requirements over a specified vehicle lifetime.

Optimized charging will require communication of electricity price forecasts to the battery charger. Under the SAE J1772 standard [114] this can be

accomplished through optional communication pins or through power line communications using standard connectors. A collection of existing and in-progress SAE standards—J2836, J2847, and J2931—establish use cases, protocols, and recommended practices for communications between vehicles, EVSEs, the electric grid, and internet-connected devices [115]. An intelligent controller embedded in the vehicle charger may therefore access pricing information in order to generate optimized power commands. The charger then uses lower-level battery charging controls such as those described in [116]–[119] to create optimized voltage and current commands.

Several existing works address PHEV charge profile optimization without attempting to simultaneously minimize battery degradation, e.g. [99]–[101], [120]–[124]. Other works have developed battery models that estimate long-term Li-ion battery degradation [108], [109], [111]–[113], [125]–[127].

Previous works that simultaneously optimize charging cost and battery life include [30], [102], [111], [125], [126]. In [125], an electrochemistry-based battery model is used in a genetic algorithm to find a Pareto front of optimal energy cost and battery resistance growth rather than a single actionable charge profile. In contrast, the intelligent DAC algorithm presented here minimizes the total cost of charging, defined as the cost of energy plus the equivalent monetary cost of battery degradation. The model described in [126] estimates battery degradation in monetary terms. Recognizing that lifetime data is difficult to obtain for most commercial batteries, it derives a lifetime model from achievable cycle count (ACC) versus depth of discharge (DOD) data, which is more widely available. However, this type of data neglects important temperature related effects and, for low DOD, is typically taken only at high state of charge (SOC), leading to a degradation model that unduly favors early charging. In [111], model predictive control is used to

optimize charging for a grid battery energy storage system, including a battery degradation cost function. This cost function accounts for SOC-related degradation, power-related degradation, and cycling-related degradation. Sample optimization results show the battery frequently turning on and off to avoid what the model perceives as high-DOD cycling.

To facilitate iterative, numerical minimization of total cost, this thesis describes a simple model for estimating the cost of battery degradation first presented in [30], [102]. This model is not intended to advance the science of Li-ion battery life estimation, but only to efficiently capture the dominant effects present in advanced battery lifetime models. The simple model presented here has been verified through comparison of its results to those of a detailed model developed at the NREL for Li-ion batteries with nickel-cobalt-aluminum (NCA) cathode and graphite anode [106], [128], [129]. NREL's model has in turn been shown to agree well with experimental data. The NCA Li-ion chemistry was chosen for degradation modeling due to the public availability of aging data for a wide variety of temperature and duty-cycle operating conditions. It should be noted that cathode materials such as nickel-manganese-cobalt, manganese-spinel, and iron-phosphate may be preferred for present PHEV and EV designs due to their safety characteristics. It has not been established how well the NCA model will represent other Li-ion chemistries, but it is anticipated that other chemistries with similar degradation mechanisms could be modeled in a similar fashion after adjustment of model parameters [109], [112].

6 Degradation-aware charging method

6.1 Simple battery degradation model

6.1.1 Overview

In order to simultaneously optimize battery life and energy cost, estimated equivalent costs of battery degradation are defined here in terms of battery lifetime reduction. The cost of battery degradation, c_{bd} , due to a charge cycle is defined as

$$c_{bd} = c_{bat} * \frac{\Delta L}{L} \quad (12)$$

Here c_{bat} is the cost to purchase the battery pack, ΔL is the lifetime degradation due to the charge cycle being evaluated per unit time, and L is the total battery lifetime if the charge cycle under evaluation were repeated until the battery's end of life (EOL). Estimating $\Delta L/L$, the *fractional lifetime degradation* resulting from a battery charge profile, allows formulation of a cost function for that charge profile. By minimizing c_{bd} , we are maximizing battery life.

EOL for a vehicle drive battery is defined as the time when either the battery's energy capacity or its available power drops below a specified minimum. Typically, the EOL energy capacity Q_{EOL} is designed to be about 80% of the initial capacity Q_0 in order to provide the desired energy storage over the vehicle's design life at minimal cost: $Q_{EOL} = 0.8Q_0$ [130]. Battery power is typically oversized relative to the minimum design EOL power for economic reasons; additional power makes more energy accessible at low SOC without requiring addition of expensive active material [131]. To reflect this, EOL power is defined here as $P_{EOL} = 0.7P_0$, where P_0 is the initial maximum power, in agreement with [132].

The normalized maximum power available from the battery, P_{fade} , diminishes over time as a result of internal resistance growth [106]. $P_{fade}(t)$ is defined as $P_{max}(t)/P_0$ and is equal to $R_0/R(t)$, where P_{max} is as defined in [133], R_0 is the initial internal resistance, and $R(t)$ is the internal resistance at time t . This relationship is derived in Appendix A of [30].

This work models battery lifetime dependencies for the majority of vehicles with batteries that operate and degrade normally. The very small portion (< 10 ppm expected) of cells that fail abruptly due to defects is not considered here.

Over a daily battery cycle, significant factors that influence power fade and capacity fade are temperature $T(t)$, open circuit voltage $V_{oc}(t)$, and charge cycling (DOD) [109], [110], [134]. The simple battery model proposed here makes two approximations: 1) Each of these effects is independent of the others, and 2) The effects themselves are independent of battery age and state of health. Approximation 1 allows the model to be simple enough to be evaluated quickly and allows it to be tuned to fit available data sets that often only consider one of the three factors. The degree of validity of this approximation is a complex question requiring further research [109]. Approximation 2 allows the simple battery model to be time-invariant over battery life. As can be seen by comparing the slope of the curved relative capacity $Q(t)$ line in Figure 42 to its average slope, this approximation is very good, but not perfect, over most of the battery lifetime. Finally, we note that V_{oc} maps directly to SOC , so voltage-related degradation can also be considered SOC -related degradation.

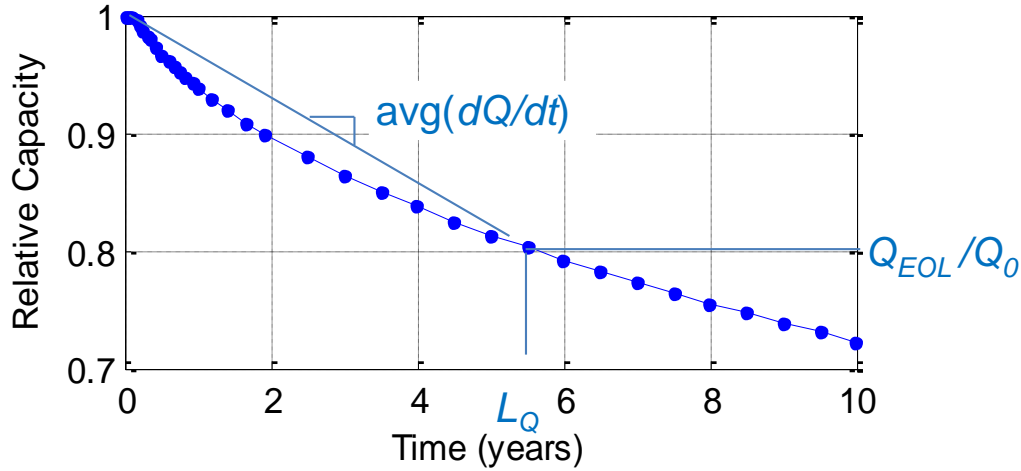


Figure 42. Finding energy capacity lifetime, L_Q , from NREL's model.

Using these approximations to consider the effects of $T(t)$, $SOC(t)$, and DOD on capacity lifetime and power lifetime, the cost of battery degradation is

$$c_{bd} = \max\left((c_{Q,T} + c_{Q,SOC} + c_{Q,DOD}), (c_{P,T} + c_{P,SOC} + c_{P,DOD})\right) \quad (13)$$

where $c_{Q,T}$, $c_{Q,SOC}$, and $c_{Q,DOD}$ are the costs associated with capacity fade and $c_{P,T}$, $c_{P,SOC}$, and $c_{P,DOD}$ are the costs associated with power fade due to temperature, SOC, and DOD, respectively. The battery model presented here models all three capacity-related costs, as well as the cost of power fade due to temperature, $c_{P,T}$. Based on [134], the costs $c_{P,SOC}$ and $c_{P,DOD}$ are assumed to be negligible in comparison to the other costs and hence are not modeled. The next three subsections describe how these costs are approximated in the simplified battery model.

6.1.2 Temperature-related degradation: $c_{Q,T}$ and $c_{P,T}$

Estimates of the two temperature-related costs, $c_{Q,T}$ and $c_{P,T}$, are based on the Arrhenius relationship: $r = A * e^{-E/kT}$, where r is the rate of the reaction assumed to be behind the battery degradation, E is the activation energy of the reaction, k is

Boltzmann's constant, T is battery temperature, and A is a proportionality constant [106]. Lifetime $L(T)$ is inversely proportional to r , so that $L(T) = ae^{b/T}$, where the parameters a and b are described below. Because temperature affects power fade and capacity fade differently, we define power lifetime $L_P(T) = a_P e^{b_P/T}$ and capacity lifetime $L_Q(T) = a_Q e^{b_Q/T}$. The a and b parameters in these equations are determined by fitting $L(T)$ to NREL model data as described in [30]. A method for automatically tuning a and b is also described in [30].

The temperature change produced by a given charge profile is approximated as a linear function of charge power so that $T(P) = T_{amb} + R_{th} * P_{avg}$, where R_{th} is the thermal resistance of the battery pack (including any active cooling if present), T_{amb} is the ambient temperature, and P_{avg} is the average of the absolute value of temperature over a preceding time window. This approximation is good as long as the battery system's thermal time constant is short compared to the time spent at each power set point. The absolute value of P is used so that $T(P)$ is valid for charging, driving, and vehicle-to-grid (V2G) power exportation.

The tuned lifetime estimation functions, $L_P(T)$ and $L_Q(T)$, inevitably include non-charging-related degradation effects as well. To account for this, only the difference in fractional degradation relative to a baseline is included. Charging at the minimum power, P_{min} , required to fully charge the battery in the available time window, t_{max} , serves as the baseline against which other charge profiles are evaluated. This reasoning leads to equation (14) for $c_{P,T}$ and $c_{Q,T}$, with detailed derivation shown in Appendix C of [30]:

$$c_{x,T} = c_{bat} \cdot \left(\underbrace{\int_{t_{ch}} \frac{1}{8760 \cdot L_x(T_{amb} + R_{th} \cdot |P(t)|)} dt}_{\Delta L/L \text{ due to charging}} + \underbrace{\frac{t_{max} - t_{ch}}{8760 \cdot L_x(T_{amb})}}_{\Delta L/L \text{ while plugged in but not charging}} - \underbrace{\frac{t_{max}}{8760 \cdot L_x(P_{min} \cdot R_{th} + T_{amb})}}_{\text{Baseline } \Delta L/L \text{ that would be expended by slow charging}} \right) \quad (14)$$

In (14), the placeholder subscript x becomes P when evaluating $c_{P,T}$, and it becomes Q when evaluating $c_{Q,T}$. The constant 8760 is the number of hours in a year, and $\Delta L/L$ is battery life expended over the interval in question as a fraction of total lifetime, as defined previously.

6.1.3 SOC-related degradation: $c_{Q,SOC}$

The cost $c_{Q,SOC}$, which accounts for capacity fade attributable to $SOC(t)$, is calculated using a linear fit formula based on 15-year capacity versus average SOC data from [130]. The linear fit parameters have been tuned to fit more recent NREL model data points. We use the approximation of time-invariance explained above and the further approximation that, when accounting only for SOC-related degradation, a time period during which the SOC varies around an average of SOC_{avg} has the same effect on battery life as simply staying at SOC_{avg} for the same time period. The accuracy of this approximation varies by situation, but the approximation is necessary to arrive at a simple model that does not require high time-resolution SOC data. The cost of one hour during which the average SOC is SOC_{avg} is then

$$c_{Q,SOC} = c_{bat} \cdot \frac{m \cdot SOC_{avg} - d}{CF_{max} \cdot 15 \cdot 8760}. \quad (15)$$

Here CF_{max} is the capacity fade at EOL, which we have taken above to be 100% - $Q_{EOL}/Q_0 = 20\%$, and m and d are linear fit parameters. The states of charge in question are presumed to be limited by the vehicle's battery protection controls to a manufacturer-specified range, e.g., $20\% < SOC < 90\%$ [135].

6.1.4 *Depth of discharge related degradation: $c_{Q,DOD}$*

The cost $c_{Q,DOD}$ accounts for capacity fade resulting from daily SOC swing ΔSOC , defined as the maximum daily SOC minus the minimum, also referred to as DOD. Effects of low amplitude, high frequency cycling, as would occur when a V2G-capable vehicle provides an ancillary service such as frequency regulation, are not captured in $c_{Q,DOD}$. This type of cycling does result in temperature changes, so temperature-related degradation due to ancillary services is captured in $c_{Q,T}$ and $c_{P,T}$ if the model uses sufficient time resolution. The calculation of $c_{Q,DOD}$ used here is based on data from [136] showing the effects of ΔSOC on battery lifetime in cycles, N :

$$N(\Delta SOC) = \left(\frac{\Delta SOC}{145.71} \right)^{-0.6844} \quad (16)$$

We make the approximation that n cycles at a given ΔSOC have the same effect as n cycles whose average SOC swing is equal to ΔSOC . It is difficult to determine the degree of validity of this approximation from the available data, but again the approximation is necessary to facilitate a simple model.

To estimate the cost associated with a cycle at ΔSOC_i , we employ the concept of *energy throughput* [137]. We define E_{TL} as the lifetime energy throughput, $E_{T,used}$ as the total change in the remaining energy throughput due to a cycle, and $E_{T,base}$ as the minimum energy throughput required to recharge the battery. The cost $c_{Q,DOD}$ is then

$$c_{Q,DOD} = c_{bat} \cdot \frac{(E_{T,used} - E_{T,base})}{E_{TL}} \quad (17)$$

Details on the calculation of each energy throughput are included in Appendix D of [30].

6.1.5 Model tuning and verification

Despite the approximations made in estimating battery lifetime, the model can be quickly tuned so that its results agree well with NREL's model, which has been shown to agree well with physical data in [106], [128], [129]. Details of the tuning process can be found in [30]. The correlation between the simple battery model and NREL's model is further evident from the simulated results presented in Chapter 7.

6.2 Charge optimization algorithm

The total cost to charge an EV or PHEV, c_{tot} , is defined here as the sum of the cost of electrical energy, c_{kWh} , and the estimated cost of battery degradation, c_{bd} :

$$c_{tot} = c_{kWh} + c_{bd}. \quad (18)$$

Mathematically, $c_{kWh} = \int_{t_{ch}} e(t)P(t)dt$, where $e(t)$ is the electricity cost, $P(t)$ is the charge power, and t_{ch} is the time spent charging. Note that $P(t)$ may be negative for certain t , indicating V2G power exportation. The signal $e(t)$ is provided externally by a utility, aggregator, or other entity. Also note that the electricity cost $e(t)$ can be constant or variable, and if variable, can be dynamic or static. In the case of a dynamic $e(t)$, each vehicle's charge profile is re-optimized upon a change in forecast $e(t)$. For a given charging opportunity, the optimal charge profile is determined by numerically minimizing c_{tot} over the entire time the vehicle is plugged in. Specifically, charging power, $P(t)$, and electricity cost, $e(t)$, are discretized onto intervals \mathbf{k} of lengths $\mathbf{D} = d(k)$ to facilitate numerical optimization, becoming $\mathbf{P} = P(k)$ and $\mathbf{e} = e(k)$. The objective of the optimization is to find the

power profile $\mathbf{P}_{opt} = P_{opt}(k)$ that minimizes the total cost to charge the battery, c_{tot} , which is the sum of the cost of electricity, $c_{kWh} = e(k)P(k)d(k)$, and the estimated costs of battery degradation during each interval, $c_{bd}(k)$. Hence the objective function is:

$$\mathbf{P}_{opt} = \arg \min_{\mathbf{P}} \sum_k (e(k)P(k)d(k) + c_{bd}(k)) \quad (19)$$

The constraints on the charge optimization algorithm given by battery energy capacity Q , initial SOC SOC_0 , plug-in time t_p , and target time for full charge t_t (where full charge may be <100% SOC to avoid accelerated battery degradation at high SOC). If V2G is allowed, a minimum allowed SOC should also be provided. The target time for full charge should typically be an hour or so before the vehicle will be driven, both in case the vehicle is needed earlier than expected, and to give the battery sufficient time to cool before driving begins [138]. The time by which the vehicle must be charged may be supplied by the user or generated by a machine learning algorithm that predicts future behavior from past patterns, as suggested in [138]. The constraint that the battery be fully charged at the end of the window is expressed as

$$SOC_0 + \frac{1}{Q} \sum_k P(k)d(k) = SOC_{max} \quad (20)$$

The constraint that SOC remain within its bounds at all times can be expressed as

$$SOC_{min} \leq SOC_0 + \frac{1}{Q} \sum_{k_i=1}^k P(k)d(k) \leq SOC_{max} \quad \forall k \quad (21)$$

Meanwhile the battery power must remain within the limits imposed by the charger capabilities, P_{min} and P_{max} :

$$P_{min} \leq P(k) \leq P_{max} \quad \forall k \quad (22)$$

The output of the optimization algorithm is a charge profile \mathbf{P}_{opt} that meets these constraints and minimizes total cost c_{tot} .

The charge optimization algorithm presented here optimizes charge power only. The charge current and voltage are to be managed separately by lower-level controls in the vehicle charger, for example as in [116]–[118].

The charge optimization is implemented in MATLAB using the built-in nonlinear constrained optimization function, `fmincon()`. To avoid local minima in c_{tot} , `fmincon` is seeded with various starting charge profiles and the result with the lowest cost c_{tot} is selected; this approach solves the problem faster than other optimization methods without significant susceptibility to local minima. The optimization runs in about 5 seconds per vehicle on a 2.8 GHz Windows 7 machine. For comparison, NREL’s accurate model runs in 5 to 10 seconds per iteration on the same machine; several thousand iterations would be required to find the minimum cost c_{tot} , so optimization using NREL’s model directly would require many minutes.

To implement a charge optimization algorithm in practice, it would be desirable to use more economical embedded computing within an on-board charger or EVSE, making the simplicity and speed of the model proposed here advantageous. If it is only desired to use the optimization under conditions of constant electricity cost, it would be possible to implement it using look-up tables, so a very low-cost microcontroller would be sufficient. However, to take full advantage of the algorithm’s ability to simultaneously account for time-varying electricity cost and battery degradation, it will need to be implemented on a more capable microprocessor; despite its relative simplicity, the algorithm does require numerical optimization. As currently implemented in MATLAB, the algorithm uses

a function that cannot be directly compiled into machine-executable code. One easier-to-implement option is to use a Linux-capable microprocessor such as Intel's Atom as done for a home energy management system in [139], which could run the MATLAB algorithm directly as compiled using MATLAB Compiler. A lower-cost alternative would be to translate the algorithm into C or C++ using one of the available optimization libraries, allowing the use of a standard microprocessor without a desktop-strength operating system. Finally, since the optimization algorithm needs to run relatively infrequently, a low-cost microcontroller in combination with a cloud-based optimization would be another practical option [140].

7 Degradation-aware charging results

This chapter presents simulated examples of the use of the degradation-aware charge optimization algorithm under different electricity cost profiles. It also presents a comparison of the estimated lifetime of vehicles charged using DAC optimization to vehicles charged using other methods.

7.1 Optimized charge profiles

The charge optimization algorithm was run simultaneously for three vehicles with different plug-in times, initial SOC, and target times for full charge. Each vehicle had a 30-kWh battery pack with a minimum SOC of 20% and a maximum SOC of 90%. The thermal resistance R_{th} of the battery was taken to be 0.002 °C/W, and the ambient temperature was 25 °C. The maximum charge and discharge powers were both 6.6 kW (SAE Level 2). Figure 43 through Figure 46 show optimized charge profiles under four different price profiles. Colored arrows at the

top of each figure indicate the user-supplied times when the vehicles plug-in in the evening and unplug in the morning. In each of these four examples, the three EVs plug in with 30%, 50%, and 60% SOC, respectively, unless otherwise indicated.

In Figure 43, the cost of electricity is a constant \$0.12/kWh. The three charge profiles all show a compromise between charging late in the available window and spreading of charge over time. The tendency to charge later is the dominant trend, and is due to $c_{Q,SOC}$, which discourages spending time at high SOC (i.e., high V_{OC}). Engineers accustomed to other battery chemistries may find it unexpected that lower SOC is preferable from the perspective of battery health; however, this finding does agree with the literature [138], [141]. The spreading of charge over time is due to $c_{Q,T}$ and $c_{P,T}$, which discourage high power (i.e., high temperature) charging.

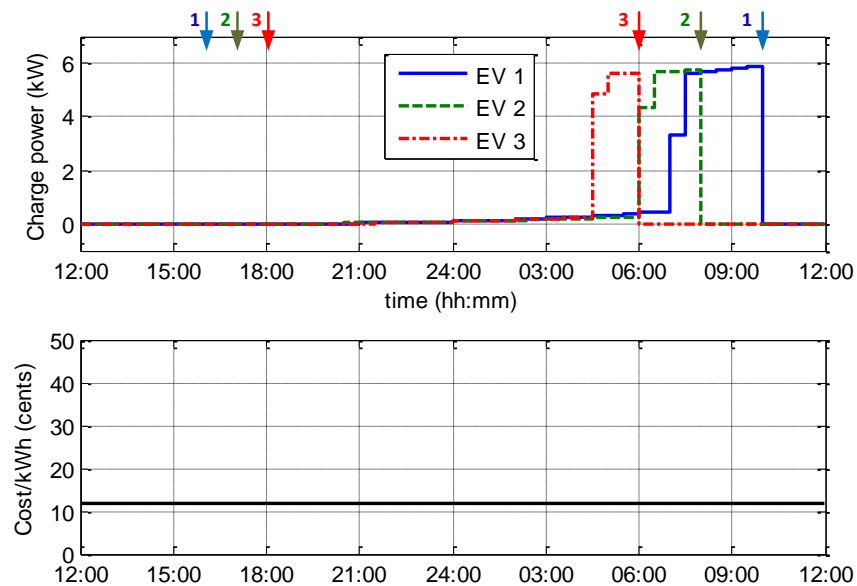


Figure 43. Optimized charging with constant energy cost.

In Figure 44, a simple two-level cost structure is used, such as might be implemented by grid operators to encourage charging at off-peak times. The vehicles now do a significant portion of their charging during the 23:00 to 05:30 low-cost interval, and the spike in charging power in early morning is reduced. The two competing trends seen in Figure 43 (spreading out charge and charging late in the available window) are present in Figure 44 as well.

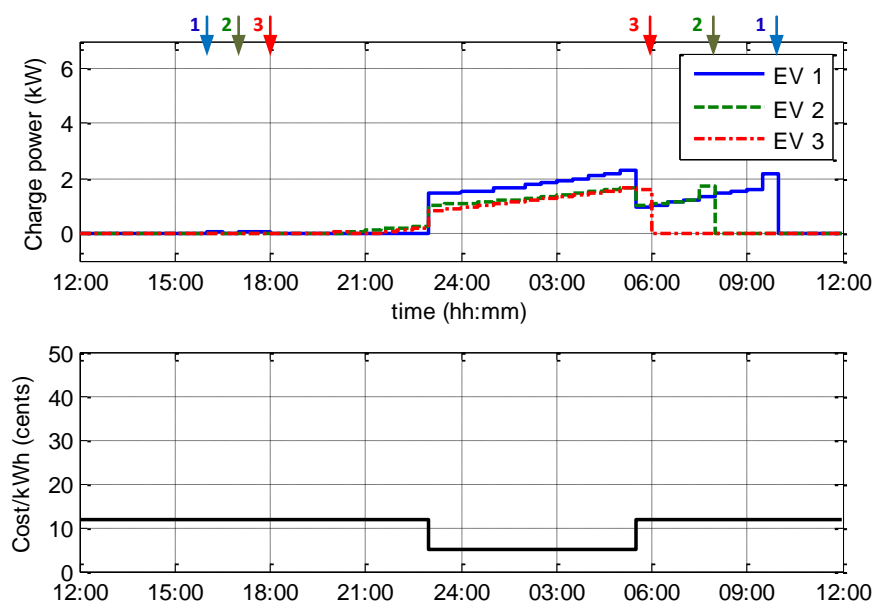


Figure 44. Optimized charging simple two-level energy cost.

Figure 45 uses historical hourly average Mid-Columbia (MIDC) wholesale electricity price data [142] for July 1, 2011. Prices that day were fairly typical for the Pacific Northwest region of the U.S. during summer. The vehicles show little preference for charging in the lowest-cost interval. This is because the price difference between that interval and other nearby intervals is small, so battery

health preservation is the dominant effect. Also note that no charging is performed during the highest cost intervals.

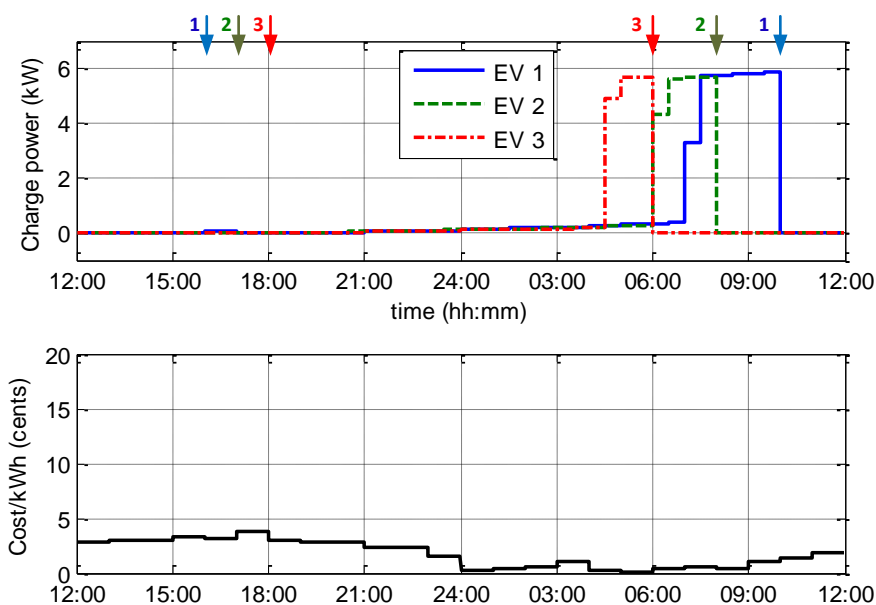


Figure 45. Optimized charging with historical MIDC price on a typical day.

Figure 46 also uses MIDC price data, but for July 6, 2011. This day included a rare, order-of-magnitude price spike from 15:00 to 17:00. Plug-in times were moved to 14:00 and starting SOC_s were raised to 50%, 60%, and 70% respectively to give the vehicles ample opportunity to perform V2G power arbitrage. Note that despite the high price differential, the vehicles do not perform V2G because it is still not economical given the increased battery degradation. This is partially because any energy exported must subsequently be imported back, leading to additional temperature-related degradation. While this result indicates that a very high price differential is required to make V2G energy arbitrage economical, it should be noted

that low amplitude, high-frequency V2G associated with frequency regulation or PV intermittency mitigation may be practically viable [42] but is not modeled here.

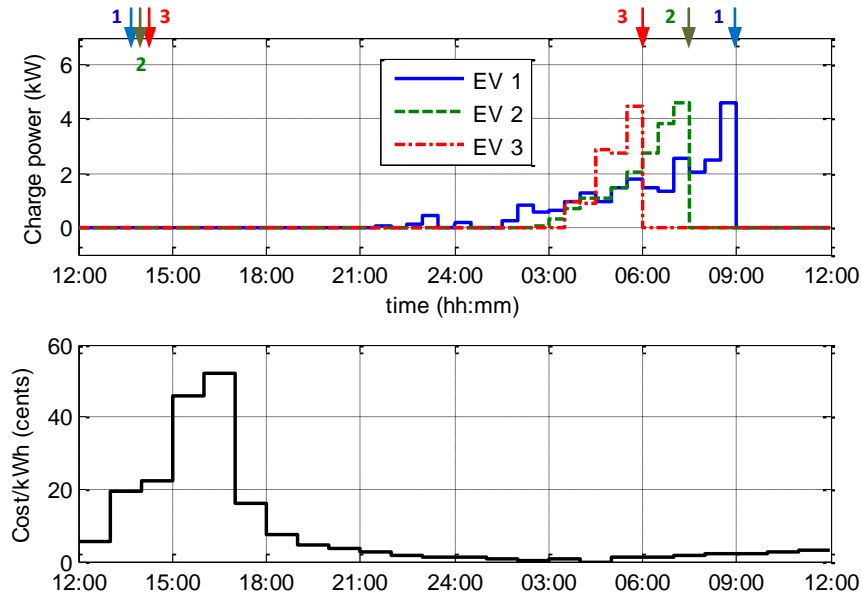


Figure 46. Optimized charging with historical MIDC price showing an unusual spike.

Because the cost of battery degradation due to V2G is partially due to temperature-related costs, effective thermal management could make V2G economical at lower power prices. This is demonstrated in Figure 47, where R_{th} has been lowered to $0.0001^{\circ}\text{C}/\text{W}$, $0.0005^{\circ}\text{C}/\text{W}$, and $0.001^{\circ}\text{C}/\text{W}$ for the three vehicles, respectively. Initial SOC for the three vehicles has been set at 60%. Vehicle 1, with the lowest thermal resistance and hence the least sensitivity to temperature-related battery degradation, performs a small amount of V2G energy arbitrage, and the other vehicles perform none due to their higher R_{th} values. From this brief analysis it appears that very high price differentials and/or very effective thermal management may be required to make V2G energy arbitrage economical.

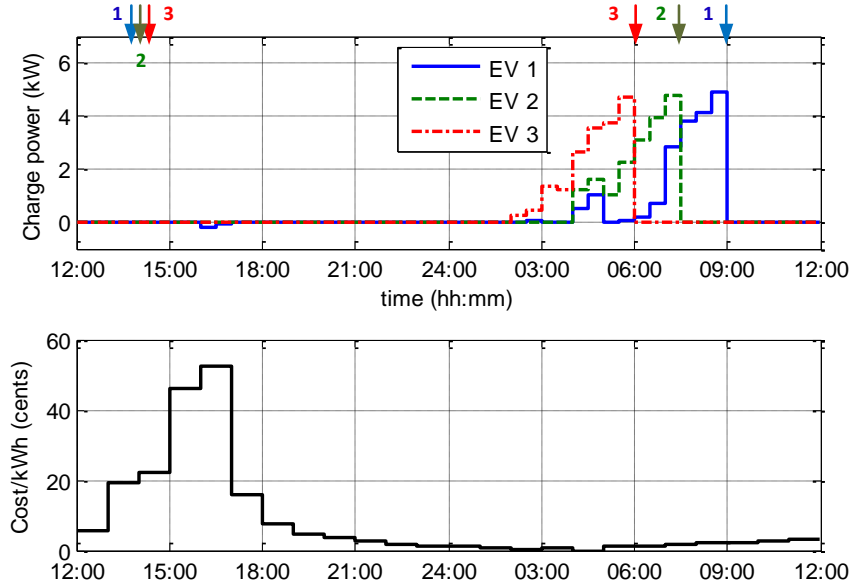


Figure 47. Optimized charging showing a small amount of V2G.

7.2 Battery lifetime comparisons

To confirm that the charge optimization method presented here actually reduces battery degradation, experimental driving data from a large scale usage study of Toyota Prius PHEVs [143] was combined with several simulated charge profiles described below. A typical driving week was selected involving five days of commuting 26-40 km (16-25 miles) round-trip, one longer trip of 65 km (40 miles), and one day on which the vehicle was not used. These data provided the driving SOC profiles, time windows available for charging, and initial SOC values for each charge. Simulations were performed for three battery sizes: the 3.5 kWh battery in the Prius, a 19 kWh battery, and a larger 35 kWh battery. Hypothetical simulated SOC profiles were generated for the larger batteries by scaling the Prius data.

Six charging scenarios, summarized in Table 5, were imposed upon each experimental driving SOC profile. Figure 48 shows weekly SOC profiles for all

three batteries under each charge scenario. The charge scheme labeled “Optimized” uses the DAC optimization method described here, with flat cost of electricity so that battery life is maximized. The two “Early” schemes begin charging 5 minutes after the vehicle is plugged in. The two “Late” schemes reach full charge 30 minutes before the vehicle leaves. The “Late 24 kW” scheme would require a DC fast charger.

Table 5. Charge profile descriptions

Name	Description
Optimized	Optimized using degradation-aware charging
Early 3.3 kW	Charge upon plug-in at 3.3 kW
Early 6.6 kW	Charge upon plug-in at 6.6 kW*
12am 6.6 kW	Charge at midnight at 6.6 kW*
Late 6.6 kW	Charge as late as possible at 6.6 kW*
Late 24 kW	Charge as late as possible at 24 kW

* SAE Level II maximum

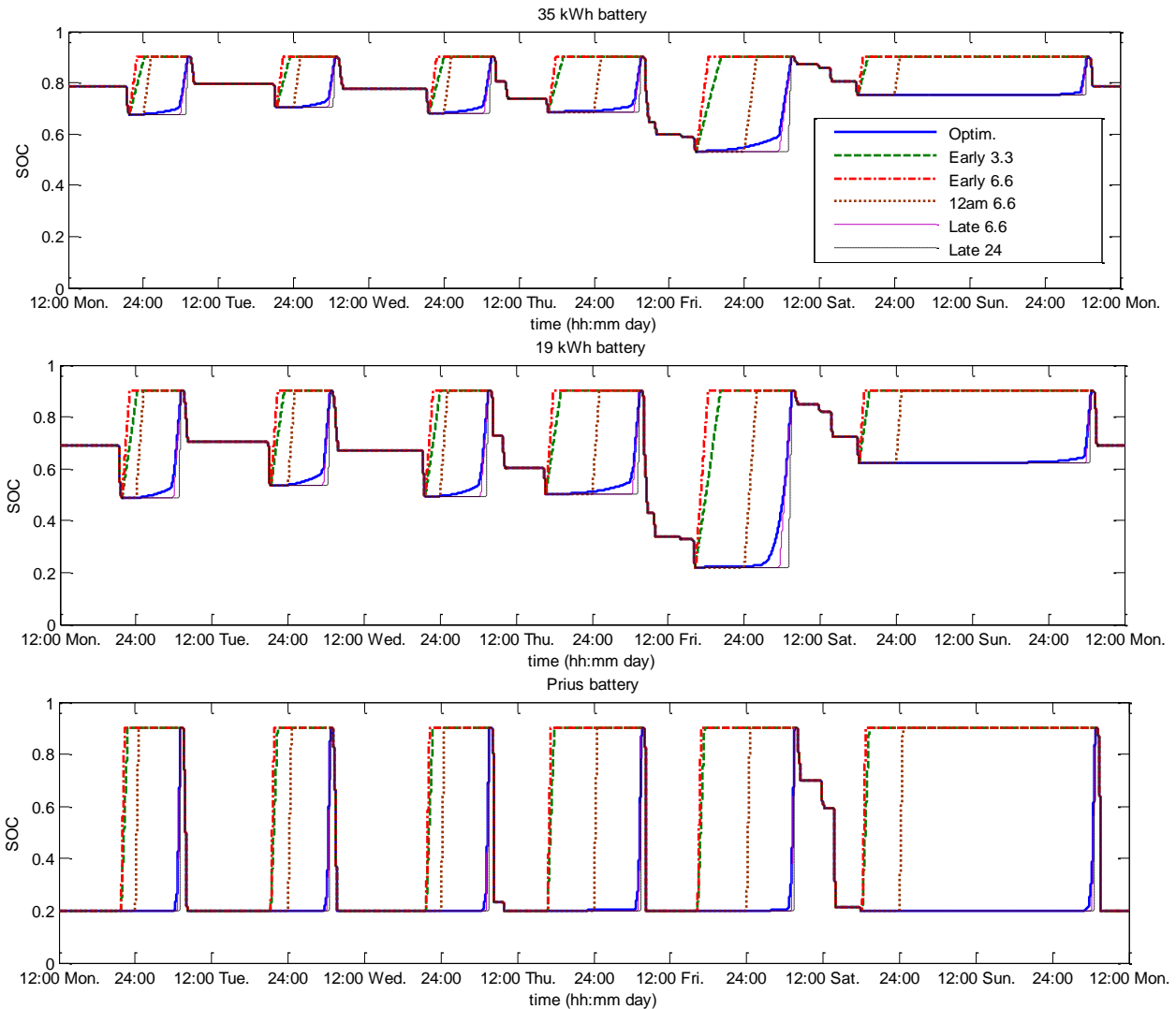


Figure 48. Weekly SOC profiles for three battery sizes under various charging scenarios.

The charge optimization method proposed in [126] states that immediate charging minimizes battery degradation and hence would presumably select a charge profile similar to one of the two early charging scenarios. The optimization method described in [125] selects for charging late in the available window and hence is most similar to the two late charging scenarios.

The charge profile data shown in Figure 48 was fed into NREL's battery lifetime predictive model to compute the estimated battery lifetime for each scenario, assuming the charge cycle is repeated weekly. Figure 49, Figure 50, and Figure 51 show battery lifetime for each scenario for the three different battery types considered. Both capacity life and power life are shown for each charge profile; the actual battery life is the lesser of the two, which is the capacity lifetime in all cases, as expected.

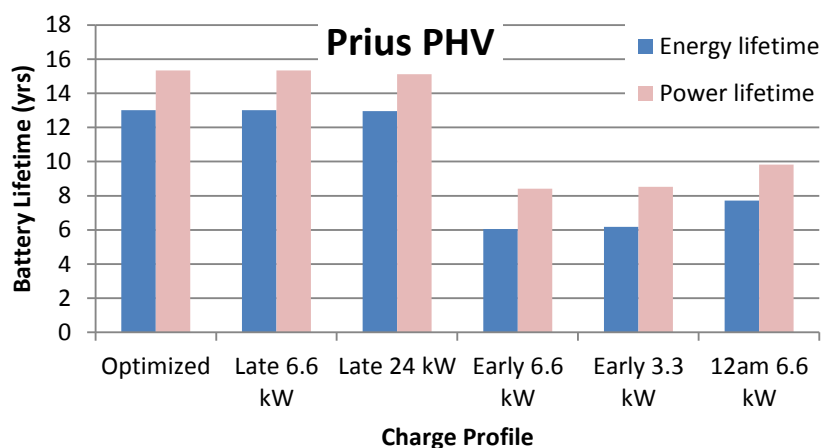


Figure 49. Prius battery lifetime under various charge scenarios.

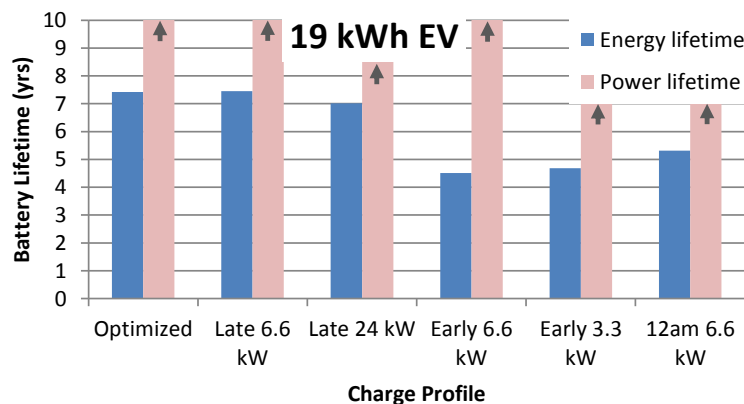


Figure 50. Nineteen kWh battery lifetime under various charge scenarios. Power lifetimes truncated as indicated by arrows.

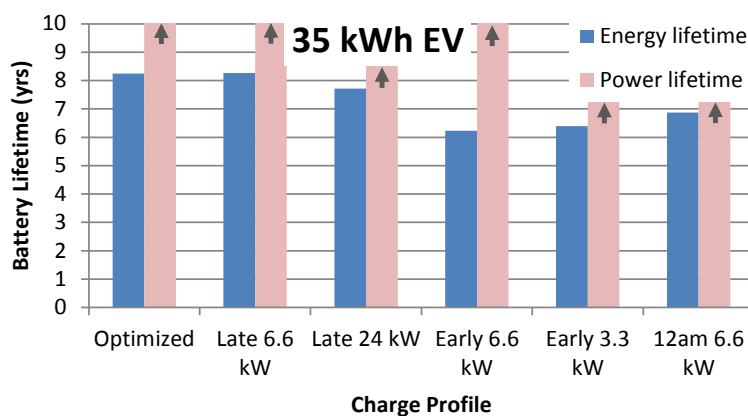


Figure 51. Thirty-five kWh battery lifetime under various charge scenarios. Power lifetimes truncated as indicated by arrows.

For all three battery sizes, the optimized charge results in longer battery life than all but the “Late 6.6 kW” scenario, which results in essentially the same battery life (within the accuracy of the model). Simply charging at the end of the available window appears to have equal benefits to optimized charging when electricity cost is constant (though optimized charging carries clear benefits when electricity cost varies). The estimated lifetime under optimized charging is between

1% and 115% longer than the lifetime under the other scenarios considered. The gains in lifetime from optimized charging are largest for the smallest battery.

Table 6 compares the relative merits of the various charging methods considered above in addition to minimization of electricity cost alone. Of the methods considered, the optimization method presented here is the only method that provides a single charge profile that optimizes both charging cost and battery health simultaneously and effectively.

Table 6. Comparison of charge optimization methods

Charging method	Accounts for time-based electricity cost	Minimizes battery degradation	Gives single, actionable charge profile
DAC co-optimization presented here	Yes	Yes	Yes
Co-optimization presented in [126]	Yes	No	Yes
Multi-objective optimization, e.g. [125]	Yes	Yes	No
Minimization of electricity cost	Yes	No	Yes
Charge on plug-in	No	No	Yes
Delayed charge (e.g. midnight)	No	No	Yes
Late charge	No	Yes	Yes

The benefits of charging late in the available window must of course be balanced with the utility of the vehicle: having the vehicle unavailable for unexpected late-night trips may be unacceptable to some drivers. This consideration is most important for EVs and may not be a concern for PHEV drivers.

In summary, Part II of this thesis has presented a method for minimizing the cost of EV or PHEV charging given variable electricity costs while also accounting for estimated costs of battery degradation using a simplified Li-ion battery lifetime model. The concept of *fractional lifetime degradation* ($\Delta L/L$) described here allows battery wear-related costs to be calculated and compared directly to energy costs. It has been shown that batteries charged using the proposed optimization algorithm, which includes simple modeling of the costs of battery degradation, are predicted to live longer than batteries charged using other charging methods. This result has been confirmed using NREL's more accurate battery lifetime model, which in turn has been shown to agree with physical data.

The charge optimization method presented here results in charge profiles that follow four competing trends: 1) charging during low electricity price intervals, 2) spreading of charge over time to avoid high temperatures, 3) charging near the end of the available charge time to avoid high SOC, and 4) suppression of high-power V2G. Trends 1 and 2 should tend to reduce stress on utility transformers by encouraging low-power charging at off-peak times. The possibility that trend 3 could overload transformers in the early morning can be mitigated by intelligent management of electricity price schedules, as demonstrated conceptually in Figure 44. These trends have been shown to hold for a range of battery sizes, from relatively small PHEV batteries to larger EV batteries.

One of the key insights of degradation-aware charging is that Li-ion battery life is extended by spending more time at low SOC, in contrast to lead-acid batteries. This leads to the possibility of significantly extending battery life by charging only as much as needed for the next day's usage or the next trip. This of course would require some way of predicting the amount of charge needed. In [138], it was proposed that DAC be combined with machine learning to predict the next

day's energy needs and charge a battery as needed in a manner that optimizes battery life. This combination of predictive SOC minimization and DAC optimization was shown in simulations using NREL's detailed battery life model to increase battery life by up to 150% over un-optimized charging in certain scenarios [138].

As battery lifetime models are refined, it is expected that the details of the charge optimization results presented here will change but that the general principle of balancing the estimated costs of battery degradation against the cost of electricity will remain useful. In addition, it is expected that the four trends identified will persist, although the relative weight given to each will likely change.

8 Conclusions

This chapter summarizes the contributions of this thesis and describes some possible directions for future work.

8.1 Contributions

This work makes two noteworthy contributions in the area of active power control of PV systems and one noteworthy contribution to the field of Li-ion battery charge optimization.

The first contribution of this work to PV active power control is a fast, accurate, and experimentally validated method of PV maximum power point estimation (MPPE) [65], as described in Chapter 3. This method starts with standard PV module data sheet parameters and employs numerical modeling and linear regression to develop a second-order polynomial that predicts the maximum power point of a PV system based on measured irradiance and PV module temperature. The coefficients of the polynomial are computed once offline and stored in the PV inverter's controller, allowing the controller to estimate the maximum power point of the PV array in real time. Once the maximum power point is known, the PV inverter can operate with a commanded power reserve, allowing active power to be modulated to provide any of a number of grid support functions or ancillary services including primary and secondary frequency regulation, synthetic inertia, fast frequency response (FFR), and other services [1].

This MPPE method was implemented on a prototype PV inverter connected to a PV array. The prototype PV inverter was then operated in MPPE mode while a second PV inverter connected to an identical PV array was operated in conventional

MPPT mode, as described in Section 3.4. Comparison of the output power profiles of the two inverters demonstrated the accuracy and reliability of the MPPE method across a wide range of irradiance and temperature conditions.

The second contribution related to active power control, described in Chapter 4, consists of a predictive method of controlling the DC voltage of a PV array to achieve a desired output power within a few AC line cycles [92]. Typical methods of controlling the output power of a PV array operate more slowly and thus are not as appropriate for responding to grid frequency contingency events, where speed of response is critical. The rapid active power control (RAPC) method proposed here stores a three-dimensional lookup table of the PV array voltage needed to provide a given output power at a given irradiance and PV module temperature. This lookup table can be stored in a PV inverter's controller and interpolated to convert power commands into DC voltage commands using measured irradiance and temperature. As with the MPPE method, the RAPC lookup table is generated offline from PV module data sheet parameters. A variety of other methods of controlling active power were considered; the RAPC method proposed here was chosen for its feasibility and speed.

The RAPC method was also implemented and validated on the prototype PV inverter. The inverter used MPPE mode to provide a power reserve, a power-frequency droop response was programmed into the inverter, and RAPC was used to command the inverter's DC voltage control loop. A grid simulator was used to create underfrequency and overfrequency events that emulated the range of measured frequency events that occur on bulk power systems and island power systems. The inverter responded very quickly, within a few line cycles, to both overfrequency and underfrequency events, as shown in Section 4.3.

The third contribution, introduced in Chapter 5 and presented in detail in Chapter 6, is a method of electric vehicle charge optimization considering both a time-varying cost of electricity charging and the impacts of the charge profile on the life of the Li-ion battery [30], [102]. A simplified battery degradation model captures the impacts of state-of-charge profile, depth of discharge, and battery temperature profile on the life of the battery. This model is based on more detailed battery life predictive models [128] and data. The model is used to estimate the battery degradation from a proposed charge profile, and that degradation is converted into estimated dollar terms, allowing the cost of battery degradation and the cost of charging to be numerically co-optimized using an iterative method. Crucially, the simplified battery degradation model runs orders of magnitude faster than existing detailed models, allowing it to be computed iteratively on an embedded processor such as might be present in an electric vehicle or electric vehicle service equipment.

The degradation-aware charging (DAC) method was simulated using experimental PHEV usage data to generate weekly charge profiles. The results, presented in Chapter 7, were compared to other proposed charging methods in a scenario with constant cost of power. A detailed battery life predictive model developed at NREL [128] was then used to estimate the battery lifetime under each charging method if the weekly charge profile were repeated for a number of years. The DAC method was found to improve battery life relative to other typical charging methods. It was shown to be applicable to both EV batteries and PHEV batteries. Several competing trends were noted in the charge profiles produced by DAC optimization. Some were intuitive: charging during lower cost times was preferred, and high power charging was discouraged due to the associated high temperatures. Other trends were less intuitive: V2G operation was not found to be

economical even at times of very high electricity price, and spending time at low SOC was preferred, in sharp contrast to lead acid batteries. Some of these trends may change as battery technology evolves and prices fall. The DAC charging method presented here was the first known published method for computing an optimal charge profile considering both battery life and time-varying electricity cost [30].

8.2 Future work

8.2.1 *Active power control of PV*

Both the MPPE method and the RAPC method presented here could be improved upon in various ways. Both could be automatically tuned in the field based on operational data using a machine learning technique such as an artificial neural network. For example, it appeared from experimental data presented here that the MPPE algorithm may be less accurate at lower power levels. This may be due to lower inverter efficiency at lower power levels. One could conceivably model losses a priori as a function of power level, operating temperature, and other factors, and adjust the MPPE calculation accordingly. Alternatively, a machine learning algorithm could be incorporated into the inverter controller to adjust the MPPE output empirically, perhaps based on inverter temperature, operating power, and other factors.

The RAPC method currently uses feed-forward control to achieve a very fast response, but any inaccuracies in that response could be mitigated by adding a slower power control loop. This outer loop could be adapted from conventional MPPT techniques such as “perturb and observe”, adjusting DC bus voltage slightly

to reduce the steady-state error in the inverter's output power without compromising the speed of the initial response.

In addition, it is likely possible to further optimize the size of the lookup table used for RAPC, allowing a less costly embedded processor to implement it. One strategy would be to use a smaller lookup table, sacrificing some accuracy of the initial power response to a frequency event, but mitigate the error using "perturb and observe" or a similar method. Another strategy would be to reformat the lookup table data itself, which currently uses double precision floating point numbers, to a smaller data type. However, a variety of modern embedded processors are available that can accommodate the approximately 1-megabyte lookup table used here.

The experimental demonstration of RAPC presented here took advantage of the lower-level controls already present in the prototype inverter. It may be possible to further improve the speed of the inverter's response to frequency events by tuning or modifying those lower-level controls. Specifically, the speed of the inverter's response to frequency events is limited by the bandwidth and stability of both the phase-locked loop (PLL) and the DC voltage controller. Optimizing the PLL for RAPC applications may enable it to detect frequency changes more quickly while maintaining stability. Similarly, it may be possible to tune or modify the DC voltage control loop to provide faster response while ensuring stability.

For economic reasons related to the recently-reduced cost of PV modules, many PV systems today are designed with a high DC:AC power ratio, meaning that the power rating of the PV array is significantly larger than the power rating of the inverter(s). Typical DC:AC ratios are often over 1.2 and sometimes over 1.5, based on the author's communications with PV industry engineers. Thus for some time

during the middle of a sunny day, up to several hours, the PV array has significantly more power available than the inverter can export. Notably, those midday hours are often exactly when the portion of power coming from inverter-based sources is at its highest, so the need for APC may also peak at this time. This has two implications for APC of PV. First, providing power reserve for up-regulation during peak PV production hours requires only a higher-capacity inverter, not a higher-capacity PV array. Second, because large contingency events are relatively rare (Figure 52), it may be possible to overdrive PV inverters on these occasions without causing failure of switches or other components. Preliminary results based on switching and conduction loss analyses and detailed thermal simulation of a SiC MOSFET-based storage inverter providing grid frequency support suggested that the SiC devices may survive such events, though additional analysis would be needed to determine the impact of those events on inverter lifetime [144]. While SiC devices are known to have a higher tolerance for overcurrent due to their high temperature operation, it may be possible to show that even conventional Silicon IGBTs can tolerate some level of infrequent overdriving, enabling PV systems to provide some frequency event mitigation at certain times without curtailing PV or oversizing the inverter. However, this would represent a very substantial change from the way PV inverters are currently operated.

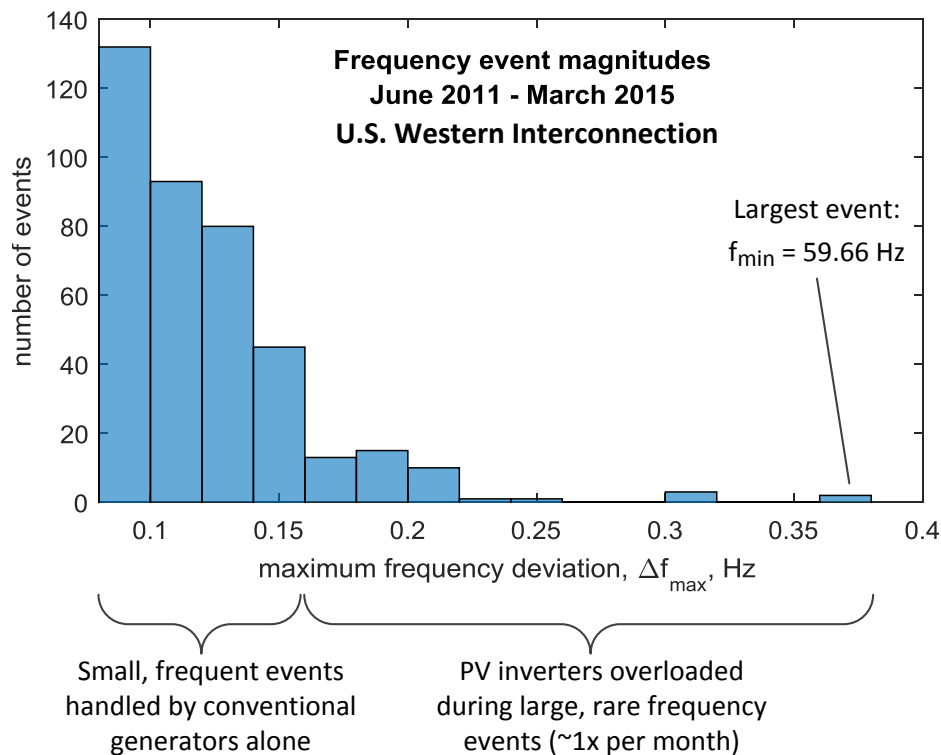


Figure 52. Histogram of recent frequency events in the U.S. Western Interconnection. While small events are common, larger events become increasingly rare. Annotations on the figure show one possible strategy for providing PV-based frequency event response.

The combination of MPPE and RAPC enables a suite of PV grid support functions and ancillary services from PV plants. Some interconnected utility grids are anticipating (or experiencing) degraded frequency stability due to a decrease in system inertia caused by a rise in inverter-coupled generation. Some utilities serving such regions are thus showing an increasing interest in very fast frequency support from DERs, including PV. However, it is an open question what the optimal type of inverter-based response to frequency events is. Because of the emphasis on speed of response, autonomous controls will likely play a large role in the eventual solution. Candidates include, but are not limited to, fast power-frequency droop control (as demonstrated here), inertia emulation, and fast frequency response (FFR), in which all of a resource's reserve is released when on a

frequency (or df/dt) threshold is crossed. Within each of these categories of response, control parameters need to be selected to best mitigate frequency events. Selection of control method(s) and parameters will require a combination of analysis, simulation, and lab testing. A recently-started NREL research project led by the author and titled “Grid Frequency Support from Distributed Inverter-based Resources in Hawaii” intends to address these questions, focusing on the Oahu island power system. In partnership with the Hawaiian Electric Companies, Sandia National Laboratories, two PV inverter manufacturers, and other stakeholders, NREL researchers will develop and simulate inverter APC methods and test those methods in the lab and in the field. Because most PV on Oahu is connected to the distribution system, RAPC will need to be integrated with fast reactive power controls to mitigate the inevitable voltage rise that will occur when larger numbers of PV inverters simultaneously surge active power, to avoid causing the inverters to trip due to overvoltage. The project will include dynamic co-simulation of Oahu’s bulk transmission system and selected distribution circuits, to capture both frequency and voltage effects. This simulation platform will be adapted for real-time simulation and power hardware-in-the-loop (PHIL) techniques [87] will be used to dynamically integrate hardware inverters, including the prototype developed here, to the real-time simulation. This will allow the prototype inverter’s performance to be validated in an environment that emulates the dynamics of the Oahu power system. Additional simulated inverters will be included in the real-time model, allowing the effectiveness of fleets of inverters in mitigating frequency events using various APC control techniques to be evaluated.

For APC of PV inverters to be deployed on a large scale, research will be needed into how to select the amount of reserve power available at any given time. This opportunity cost of providing reserve power will need to be evaluated against

the costs of alternative methods of stabilizing bulk power systems including storage-based solutions and conventional generation-based solutions. This research will need to integrate engineering with analysis of markets and economics. It will also become part of the larger question of how best to operate an electric grid with very high levels of renewable energy not just on the time scale of frequency contingency events, but across all time scales.

8.2.2 Degradation-aware battery charging

Chapters 5 through 7 of this work focus on charging vehicle traction batteries. A similar degradation-aware charging technique can of course also be applied to stationary batteries for various applications. Grid-connected stationary batteries are currently seeing increased deployment due to falling prices, policy decisions, and the emergence of markets for certain applications. One such application is the frequency regulation market: in portions of the electric grid under the control of the independent system operator (ISO) PJM, fast-responding frequency regulation is incentivized through market mechanisms, so Li-ion battery systems are being deployed to bid into the resulting frequency regulation market. Another emerging application serves commercial and industrial utility customers whose electricity bills contain substantial peak demand charges. Peak demand charges are calculated based on the highest electricity demand from a given utility customer over the course of a month. A battery energy storage system installed on the customer's premises can reduce the peak demand by monitoring the facility's electricity usage and supplying energy during peak times. A third application of energy storage is to form microgrids, which can operate either connected to the utility grid or independently. In each of these three applications, system economics could potentially be improved by incorporating battery degradation models in the

system controls. And as additional applications for battery energy storage emerge, engineers may consider adapting degradation-aware charging into system controls.

In addition, the battery lifetime model developed here was tuned for one specific Li-ion chemistry. To be applied to any given application, it should be re-tuned for the chemistry being employed. The model should also be updated as more data and updated models of Li-ion battery lifetime become available. It is also probably possible to improve the simplified model itself or the optimization algorithm it is used with to better ensure convergence across a wide range of input variables.

References

- [1] A. Hoke and D. Maksimovic, "Active power control of photovoltaic power systems," in *2013 1st IEEE Conference on Technologies for Sustainability (SusTech)*, 2013, pp. 70–77.
- [2] A. Hoke and P. Komor, "Maximizing the benefits of distributed photovoltaics," *Electr. J.*, vol. 25, no. 3, pp. 55–67, 2012.
- [3] "Electricity Storage Technology Brief," International Energy Agency Energy Technology Systems Analysis Programme (IEA-ETSAP) and International Renewable Energy Agency (IRENA), Apr. 2012.
- [4] Stetz, T., Yan, W., and Braun, M., "Voltage Control in Distribution Systems with High Level PV-Penetration -Improving Absorption Capacity for PV Systems by Reactive Power Supply-," in *25th European Photovoltaic Solar Energy Conference and Exhibition / 5th World Conference on Photovoltaic Energy Conversion*, Valencia, Spain, 2010.
- [5] P. M. S. Carvalho, P. F. Correia, and L. A. F. M. Ferreira, "Distributed Reactive Power Generation Control for Voltage Rise Mitigation in Distribution Networks," *IEEE Trans. Power Syst.*, vol. 23, no. 2, pp. 766–772, May 2008.
- [6] "Technische Richtlinie Erzeugungsanlagen am Mittelspannungsnetz – Richtlinie für Anschluss und Parallelbetrieb von Erzeugungsanlagen am Mittelspannungsnetz." Bundesverband der Energie und Wasserwirtschaft e.V. (BDEW), 2008.
- [7] E. Troester, "New German Grid Codes for Connecting PV Systems to the Medium Voltage Power Grid," in *2nd International Workshop on Concentrating Photovoltaic Power Plants: Optical Design, Production, Grid Connection*, Darmstadt, Germany, 2009.
- [8] "Wind Farm Transmission Grid Code Provisions: A Direction by the Commission for Energy Regulation." Commission for Energy Regulation, 2004.
- [9] "Wind Turbines Connected to Grids with Voltages Above 100kV: Technical regulation for the properties and the regulation for wind turbines." Elkraft System and Eltra, Erritsø, Denmark, 2003.
- [10] "Technical Requirements for the Connection of Generation Facilities to the Hydro-Quebec Transmission System: Supplementary Requirements for Wind Generation." Hydro-Quebec, Montreal, Quebec, Canada, 2005.
- [11] "Technical Requirements for Wind Power and Photovoltaic Installations and Any Generating Facilities Whose Technology Does Not Consist of a Synchronous Generator Directly Connected to the Grid." Red Electrica, Madrid, Spain, 2008.
- [12] I. Margaris, "Power system requirements for high wind penetration." Project UpWind, Roskilde, Denmark, 2007.
- [13] "FERC Order No. 819: Third-Party Provision of Primary Frequency Response Service." Federal Energy Regulatory Commission, 20-Nov-2015.
- [14] "FERC Order No. 755: Frequency Regulation Compensation in the Organized Wholesale Power Markets." U.S. Federal Energy Regulatory Commission (FERC), Oct-2011.
- [15] H. Asano, K. Yajima, and Y. Kaya, "Influence of photovoltaic power generation on required capacity for load frequency control," *Energy Convers. IEEE Trans. On*, vol. 11, no. 1, pp. 188–193, 1996.
- [16] H. Bevrani, A. Ghosh, and G. Ledwich, "Renewable energy sources and frequency regulation: survey and new perspectives," *Renew. Power Gener. IET*, vol. 4, no. 5, pp. 438–457, 2010.

- [17] J. H. Eto, "Use of frequency response metrics to assess the planning and operating requirements for reliable integration of variable renewable generation," LBNL-4142E, 2011.
- [18] Y. G. Rebours, D. S. Kirschen, M. Trotignon, and S. Rossignol, "A survey of frequency and voltage control ancillary services—part II: economic features," *Power Syst. IEEE Trans. On*, vol. 22, no. 1, pp. 358–366, 2007.
- [19] E. Ela, M. Milligan, and B. Kirby, "Operating reserves and variable generation," Technical Report NREL/TP-5500-51978, Aug. 2011.
- [20] J. Aho, A. Buckspan, J. Laks, P. Fleming, Y. Jeong, F. Dunne, M. Churchfield, L. Pao, and K. Johnson, "A tutorial of wind turbine control for supporting grid frequency through active power control," in *American Control Conference (ACC), 2012*, 2012, pp. 3120–3131.
- [21] H. T. Ma and B. H. Chowdhury, "Working towards frequency regulation with wind plants: Combined control approaches," *IET Renew. Power Gener.*, vol. 4, no. 4, pp. 308–316, Jul. 2010.
- [22] M. C. Chandorkar, D. M. Divan, and R. Adapa, "Control of parallel connected inverters in standalone ac supply systems," *Ind. Appl. IEEE Trans. On*, vol. 29, no. 1, pp. 136–143, 1993.
- [23] P. Piagi and R. H. Lasseter, "Autonomous control of microgrids," in *Power Engineering Society General Meeting, 2006. IEEE, 2006*, p. 8–pp.
- [24] A. Brissette, A. Hoke, D. Maksimovic, and A. Pratt, "A microgrid modeling and simulation platform for system evaluation on a range of time scales," in *2011 IEEE Energy Conversion Congress and Exposition (ECCE)*, 2011, pp. 968–976.
- [25] EPRI, "Common Functions for Smart Inverters, Version 3," EPRI, Palo Alto, CA, 1023059, Feb. 2014.
- [26] M. Datta, T. Senjyu, A. Yona, T. Funabashi, and C.-H. Kim, "A Frequency-Control Approach by Photovoltaic Generator in a PV #x2013;Diesel Hybrid Power System," *IEEE Trans. Energy Convers.*, vol. 26, no. 2, pp. 559–571, 2011.
- [27] K. Eber and D. Corbus, "Hawaii Solar Integration Study: Executive Summary," National Renewable Energy Laboratory, 2013.
- [28] "Minimum Technical Requirements for Photovoltaic Generation (PV) Projects," Puerto Rico Electric Power Authority, Nov. 2011.
- [29] A. Burger, "Puerto Rico Solar Power Plant Built to Withstand Hurricanes, Deliver Power Reliably in All Types of Weather," *CleanTechnica*, Oct-2012. [Online]. Available: <http://cleantechnica.com/2012/10/03/puerto-rico-solar-power-plant-built-to-withstand-hurricanes-deliver-power-reliably-in-all-types-of-weather/>. [Accessed: 18-Jun-2016].
- [30] A. Hoke, A. Brissette, K. Smith, A. Pratt, and D. Maksimovic, "Electric vehicle charge optimization including effects of lithium-ion battery degradation," in *Vehicle Power and Propulsion Conference (VPPC), 2011 IEEE*, 2011, pp. 1–8.
- [31] F. Iov, A. D. Hansen, P. E. Sørensen, and N. A. Cutululis, "Mapping of grid faults and grid codes," Risø National Laboratory, Denmark, 2007.
- [32] M. Hand, S. Baldwin, E. DeMeo, J. Reilly, T. Mai, D. Arent, G. Porro, M. Meshek, and D. Sandor, "Renewable Electricity Futures Study," National Renewable Energy Laboratory, Golden, CO, NREL/TP-6A20-52409, 2012.
- [33] L. F. Casey, C. Schauder, J. Cleary, and M. Ropp, "Advanced inverters facilitate high penetration of renewable generation on medium voltage feeders - impact and benefits for

- the utility,” in *2010 IEEE Conference on Innovative Technologies for an Efficient and Reliable Electricity Supply (CITRES)*, 2010, pp. 86–93.
- [34] M. Li and J. D. McCalley, “Influence of renewable integration on frequency dynamics,” in *2012 IEEE Power and Energy Society General Meeting*, 2012, pp. 1–7.
- [35] R. Nelson, “Active Power Control in Siemens Wind Turbines,” National Renewable Energy Laboratory, Golden, CO, 2011.
- [36] A. Ellis, “Interconnection Standards for PV Systems: Where are we? Where are we going?,” in *UWIG Fall Meeting*, Cedar Rapids, IA, 2009.
- [37] A. Dehamna and K. Adamson, “Frequency Regulation for the Grid: Coal Power Plants, Natural Gas Power Plants, Nuclear Power Plants, and Energy Storage Systems for Delivery of Frequency Regulation Services: Global Market Analysis and Forecasts,” Pike Research, 2012.
- [38] C. Campbell, “Advanced Energy Storage: What’s the Value of Frequency Regulation?,” *Renewable Energy World*, May-2011.
- [39] B. Gibson, “Frequency Regulation Market’s Winning Combination: Low-Risk, High-Value,” *MatterNetwork*, Aug-2011.
- [40] “Electricity Data Browser,” *U.S. Energy Information Agency*. [Online]. Available: <http://www.eia.gov/beta/enerdat/>. [Accessed: 20-Oct-2012].
- [41] J. Traube, F. Lu, and D. Maksimovic, “Photovoltaic power system with integrated electric vehicle DC charger and enhanced grid support,” in *Power Electronics and Motion Control Conference (EPE/PEMC), 2012 15th International*, 2012, p. LS1d–5.
- [42] Alexander Brissette, Anderson Hoke, Joshua Traube, Fenglong Lu, and Dragan Maksimovic, “Study on the Effect of Solar Irradiance Intermittency Mitigation on Electric Vehicle Battery Lifetime,” in *IEEE Conference on Technologies for Sustainability (SusTech)*, Portland, OR, 2013.
- [43] Y. Ru, J. Kleissl, and S. Martinez, “Storage Size Determination for Grid-Connected Photovoltaic Systems,” *IEEE Trans. Sustain. Energy*, vol. 4, no. 1, pp. 68–81, Jan. 2013.
- [44] H. Fakham, D. Lu, and B. Francois, “Power Control Design of a Battery Charger in a Hybrid Active PV Generator for Load-Following Applications,” *IEEE Trans. Ind. Electron.*, vol. 58, no. 1, pp. 85–94, Jan. 2011.
- [45] S. Li, K. Tomsovic, and T. Hiyama, “Load following functions using distributed energy resources,” in *IEEE Power Engineering Society Summer Meeting, 2000*, 2000, vol. 3, pp. 1756–1761 vol. 3.
- [46] K. Ro and S. Rahman, “Two-loop controller for maximizing performance of a grid-connected photovoltaic-fuel cell hybrid power plant,” *IEEE Trans. Energy Convers.*, vol. 13, no. 3, pp. 276–281, Sep. 1998.
- [47] S. A. Zabalawi, G. Mandic, and A. Nasiri, “Utilizing energy storage with PV for residential and commercial use,” in *34th Annual Conference of IEEE Industrial Electronics, 2008. IECON 2008*, 2008, pp. 1045–1050.
- [48] A. Nasiri, “Integrating energy storage with renewable energy systems,” in *34th Annual Conference of IEEE Industrial Electronics, 2008. IECON 2008*, 2008, pp. 17–18.
- [49] W. Kempton and J. Tomic, “Vehicle-to-grid power fundamentals: Calculating capacity and net revenue,” *J. Power Sources*, Jun. 2005.
- [50] C. Banos, M. Aten, P. Cartwright, and T. C. Green, “Benefits and control of STATCOM with energy storage in wind power generation,” in *The 8th IEE International Conference on AC and DC Power Transmission, 2006. ACDC 2006*, 2006, pp. 230–235.

- [51] I. A. Hiskens and E. M. Fleming, "Control of inverter-connected sources in autonomous microgrids," in *2008 American Control Conference*, 2008, pp. 586–590.
- [52] T. K. A. Brekken, A. Yokochi, A. von Jouanne, Z. Z. Yen, H. M. Hapke, and D. A. Halamay, "Optimal Energy Storage Sizing and Control for Wind Power Applications," *IEEE Trans. Sustain. Energy*, vol. 2, no. 1, pp. 69–77, Jan. 2011.
- [53] M. H. Ali, B. Wu, and R. A. Dougal, "An Overview of SMES Applications in Power and Energy Systems," *IEEE Trans. Sustain. Energy*, vol. 1, no. 1, pp. 38–47, Apr. 2010.
- [54] C. Abbey, K. Strunz, and G. Joos, "A Knowledge-Based Approach for Control of Two-Level Energy Storage for Wind Energy Systems," *IEEE Trans. Energy Convers.*, vol. 24, no. 2, pp. 539–547, Jun. 2009.
- [55] F. Delfino, G. B. Denegri, M. Invernizzi, and R. Procopio, "An integrated active and reactive power control scheme for grid-connected photovoltaic production systems," in *2008 IEEE Power Electronics Specialists Conference*, 2008, pp. 1463–1468.
- [56] S. Winjnbergen, S. W. H. de Haan, and J. G. Slootweg, "A System for Dispersed Generator Participation in Voltage Control and Primary Frequency Control of the grid," in *2005 IEEE 36th Power Electronics Specialists Conference*, 2005, pp. 2918–2924.
- [57] N. Kakimoto, S. Takayama, H. Satoh, and K. Nakamura, "Power Modulation of Photovoltaic Generator for Frequency Control of Power System," *IEEE Trans. Energy Convers.*, vol. 24, no. 4, pp. 943–949, 2009.
- [58] H.-R. Seo, G.-H. Kim, S.-Y. Kim, N. Kim, H.-G. Lee, C. Hwang, M. Park, and I.-K. Yu, "Power quality control strategy for grid-connected renewable energy sources using PV array and supercapacitor," in *Electrical Machines and Systems (ICEMS), 2010 International Conference on*, 2010, pp. 437–441.
- [59] V. A. K. Pappu, B. H. Chowdhury, and R. Bhatt, "Implementing frequency regulation capability in a solar photovoltaic power plant," in *North American Power Symposium (NAPS), 2010*, 2010, pp. 1–6.
- [60] L. D. Watson and J. W. Kimball, "Frequency regulation of a microgrid using solar power," in *2011 Twenty-Sixth Annual IEEE Applied Power Electronics Conference and Exposition (APEC)*, 2011, pp. 321–326.
- [61] A. F. Okou, O. Akhri, R. Beguenane, and M. Tarbouchi, "Nonlinear control strategy insuring contribution of PV generator to voltage and frequency regulation," in *6th IET International Conference on Power Electronics, Machines and Drives (PEMD 2012)*, 2012, pp. 1–5.
- [62] P. P. Zarina, S. Mishra, and P. C. Sekhar, "Deriving inertial response from a non-inertial PV system for frequency regulation," in *2012 IEEE International Conference on Power Electronics, Drives and Energy Systems (PEDES)*, 2012, pp. 1–5.
- [63] P. P. Zarina, S. Mishra, and P. C. Sekhar, "Photovoltaic system based transient mitigation and frequency regulation," in *2012 Annual IEEE India Conference (INDICON)*, 2012, pp. 1245–1249.
- [64] V. Gevorgian and B. O'Neill, "Advanced Grid-Friendly Controls Demonstration Project for Utility-Scale PV Power Plants," NREL, NREL/TP-5D00-65368, Jan. 2016.
- [65] A. Hoke, E. Muljadi, and D. Maksimovic, "Real-time photovoltaic plant maximum power point estimation for use in grid frequency stabilization," in *2015 IEEE 16th Workshop on Control and Modeling for Power Electronics (COMPEL)*, 2015, pp. 1–7.
- [66] A. Hoke, V. Gevorgian, E. Muljadi, and D. Maksimovic, "Managing Photovoltaic Power for use in Grid Stabilization," 62/344,013, Provisional.

- [67] B. Subudhi and R. Pradhan, "A comparative study on solar array parameter extraction methods," *Int. J. Renew. Energy Technol.*, vol. 3, no. 3, pp. 295–315, 2012.
- [68] T. Hiyama and K. Kitabayashi, "Neural network based estimation of maximum power generation from PV module using environmental information," *Energy Convers. IEEE Trans. On*, vol. 12, no. 3, pp. 241–247, 1997.
- [69] M. Taherbaneh and K. Faez, "Maximum power point estimation for photovoltaic systems using neural networks," in *Control and Automation, 2007. ICCA 2007. IEEE International Conference on*, 2007, pp. 1614–1619.
- [70] J.-C. Wang, Y.-L. Su, J.-C. Shieh, and J.-A. Jiang, "High-accuracy maximum power point estimation for photovoltaic arrays," *Sol. Energy Mater. Sol. Cells*, vol. 95, no. 3, pp. 843–851, 2011.
- [71] A. Garrigós, J. M. Blanes, J. A. Carrasco, and J. B. Ejea, "Real time estimation of photovoltaic modules characteristics and its application to maximum power point operation," *Renew. Energy*, vol. 32, no. 6, pp. 1059–1076, 2007.
- [72] J. Ma, K. L. Man, T. O. Ting, N. Zhang, S.-U. Guan, and P. W. Wong, "Dem: direct estimation method for photovoltaic maximum power point tracking," *Procedia Comput. Sci.*, vol. 17, pp. 537–544, 2013.
- [73] G. Kumar and A. K. Panchal, "Geometrical prediction of maximum power point for photovoltaics," *Appl. Energy*, vol. 119, pp. 237–245, 2014.
- [74] C. Carrero, D. Ramírez, J. Rodríguez, and C. A. Platero, "Accurate and fast convergence method for parameter estimation of PV generators based on three main points of the I–V curve," *Renew. Energy*, vol. 36, no. 11, pp. 2972–2977, 2011.
- [75] M. G. Villalva and J. R. Gazoli, "Comprehensive approach to modeling and simulation of photovoltaic arrays," *Power Electron. IEEE Trans. On*, vol. 24, no. 5, pp. 1198–1208, 2009.
- [76] C. R. Osterwald, J. Adelstein, J. A. del Cueto, B. Kroposki, D. Trudell, and T. Moriarty, "Comparison of Degradation Rates of Individual Modules Held at Maximum Power," in *Conference Record of the 2006 IEEE 4th World Conference on Photovoltaic Energy Conversion*, 2006, vol. 2, pp. 2085–2088.
- [77] J. Kleissl, M. Lave, M. Jamaly, and J. Bosch, "Aggregate solar variability," in *2012 IEEE Power and Energy Society General Meeting*, 2012, pp. 1–3.
- [78] A. D. Mills and R. H. Wiser, "Implications of geographic diversity for short-term variability and predictability of solar power," in *2011 IEEE Power and Energy Society General Meeting*, 2011, pp. 1–9.
- [79] J. Marcos, L. Marroyo, E. Lorenzo, D. Alvira, and E. Izco, "From irradiance to output power fluctuations: the PV plant as a low pass filter," *Prog. Photovolt. Res. Appl.*, vol. 19, no. 5, pp. 505–510, Aug. 2011.
- [80] Joshua Traube, "Predicting the Effects of Short-Term Photovoltaic Variability on Power System Frequency for Systems with Integrated Energy Storage," PhD Thesis, University of Colorado, Boulder, CO, 2013.
- [81] "IEEE Standard 1547: Standard for Interconnecting Distributed Resources with Electric Power Systems," IEEE, 2003.
- [82] "IEEE Standard 1547a - Standard for Interconnecting Distributed Resources with Electric Power Systems - Amendment 1," IEEE, 2014.
- [83] "IEEE P1547 Draft Standard for Interconnection and Interoperability of Distributed Energy Resources with Associated Electric Power Systems Interfaces," IEEE, 2016.

- [84] California Energy Commission, “Rule 21 Smart Inverter Working Group Technical Reference Materials,” *California Energy Commission*, 2014. [Online]. Available: http://www.energy.ca.gov/electricity_analysis/rule21/. [Accessed: 18-Jun-2014].
- [85] “Rule No. 14: Service Connections and Facilities on Customer’s Premises.” Hawaiian Electric Company, Inc., 21-Oct-2015.
- [86] E. Muljadi, M. Singh, and V. Gevorgian, “User Guide for PV Dynamic Model Simulation Written on PSCAD Platform,” NREL, TP-5D00-62053, 2014.
- [87] A. Hoke, S. Chakraborty, and T. Basso, “A Power Hardware-in-the-loop Framework for Advanced Grid-interactive Inverter Testing,” in *IEEE Innovative Smart Grid Technologies Conference (ISGT)*, 2015.
- [88] E. Ela, V. Gevorgian, A. Tuohy, B. Kirby, M. Milligan, and M. O’Malley, “Market Designs for the Primary Frequency Response Ancillary Service - Part II: Case Studies,” *IEEE Trans. Power Syst.*, vol. 29, no. 1, pp. 432–440, Jan. 2014.
- [89] P. Kundur, *Power system stability and control*. McGraw-Hill New York, 1994.
- [90] W. Kramer, S. Chakraborty, M. Shirazi, B. Lundstrom, and K. Harrison, “Advanced Power Electronics Interface Initiative: Smart Grid and Advanced Power Electronics Research and Development,” California Energy Commission, CEC-500-2014-006, Jun. 2012.
- [91] M. Shirazi, S. Chakraborty, and W. Kramer, “Software Record: Three-phase Grid-Connected IEEE 1547 Compliant Inverter LabVIEW FPGA Control Code.” National Renewable Energy Laboratory, 14-Jun-2012.
- [92] A. Hoke, S. Chakraborty, M. Shirazi, E. Muljadi, and D. Maksimovic, “Rapid active power control of photovoltaic systems,” in preparation.
- [93] “Modeling and Simulation of Photovoltaic Arrays - Prof. Dr. Marcelo Gradella Villalva.” [Online]. Available: <https://sites.google.com/site/mvillalva/pvmodel>. [Accessed: 03-Nov-2013].
- [94] C. Altenbach, *TrilinearInterpolation.VI*. 2012.
- [95] “Rate of Change of Frequency (ROCOF): Review of TSO and Generator Submissions - Final Report,” PPA Energy, May 2013.
- [96] P. Denholm and W. Short, “An Evaluation of Utility System Impacts and Benefits of Optimally Dispatched Plug-In Hybrid Electric Vehicles,” NREL Technical Report NREL/TP-620-40293, 2006.
- [97] Satish Rajagopalan, “Power Electronics in Renewable Energy and Electric Transportation from a Utility Perspective,” in *IEEE Energy Conversion Congress and Expo (ECCE) 2010*, Atlanta, Georgia, 2010.
- [98] S. Shao, T. Zhang, M. Pipattanasomporn, and S. Rahman, “Impact of TOU rates on distribution load shapes in a smart grid with PHEV penetration,” in *Transmission and Distribution Conference and Exposition, 2010 IEEE PES*, 2010, pp. 1–6.
- [99] Y. Cao, S. Tang, C. Li, P. Zhang, Y. Tan, Z. Zhang, and J. Li, “An Optimized EV Charging Model Considering TOU Price and SOC Curve,” *IEEE Trans. Smart Grid*, vol. 3, no. 1, pp. 388–393, 2012.
- [100] S. Bashash and H. K. Fathy, “Optimizing demand response of plug-in hybrid electric vehicles using quadratic programming,” in *American Control Conference (ACC), 2013*, 2013, pp. 716–721.
- [101] C. Jin, J. Tang, and P. Ghosh, “Optimizing Electric Vehicle Charging: A Customer’s Perspective,” *Veh. Technol. IEEE Trans. On*, vol. 62, no. 7, Sep. 2013.

- [102] Anderson Hoke, Alexander Brissette, Kandler Smith, Annabelle Pratt, and Dragan Maksimovic, "Accounting for Lithium-Ion Battery Degradation in Electric Vehicle Charging Optimization," *IEEE J. Emerg. Sel. Top. Power Electron.*, vol. 2, no. 3, pp. 691–700, Sep. 2014.
- [103] M. Ehsani, Y. Gao, and A. Emadi, *Modern Electric, Hybrid Electric, and Fuel Cell Vehicles: Fundamentals, Theory, and Design, Second Edition*. CRC Press, 2009.
- [104] S. M. Lukic, J. Cao, R. C. Bansal, F. Rodriguez, and A. Emadi, "Energy Storage Systems for Automotive Applications," *IEEE Trans. Ind. Electron.*, vol. 55, no. 6, pp. 2258–2267, 2008.
- [105] A. Khaligh and Z. Li, "Battery, Ultracapacitor, Fuel Cell, and Hybrid Energy Storage Systems for Electric, Hybrid Electric, Fuel Cell, and Plug-In Hybrid Electric Vehicles: State of the Art," *IEEE Trans. Veh. Technol.*, vol. 59, no. 6, pp. 2806–2814, 2010.
- [106] Kandler Smith, Tony Markel, Gi-Heon Kim, and Ahmad Pesaran, "Design of Electric Drive Vehicle Batteries for Long Life and Low Cost," in *IEEE 2010 Workshop on Accelerated Stress Testing and Reliability*, Denver, Colorado, 2010.
- [107] K. Rajashekara, "Present status and future trends in electric vehicle propulsion technologies," *IEEE J. Emerg. Sel. Top. Power Electron.*, vol. 1, no. 1, pp. 3–10, 2013.
- [108] S. Tong, M. P. Klein, and J. W. Park, "Comprehensive Battery Equivalent Circuit Based Model for Battery Management Applications," in *PowerTech (POWERTECH), 2013 IEEE*, 2013.
- [109] A. Barré, B. Deguilhem, S. Grolleau, M. Gérard, F. Suard, and D. Riu, "A review on lithium-ion battery ageing mechanisms and estimations for automotive applications," *J. Power Sources*, vol. 241, pp. 680–689, 2013.
- [110] J. Vetter, P. Novák, M. R. Wagner, C. Veit, K.-C. Möller, J. O. Besenhard, M. Winter, M. Wohlfahrt-Mehrens, C. Vogler, and A. Hammouche, "Ageing mechanisms in lithium-ion batteries," *J. Power Sources*, vol. 147, no. 1–2, pp. 269–281, Sep. 2005.
- [111] M. Koller, T. Borsche, A. Ulbig, and G. Andersson, "Defining a Degradation Cost Function for Optimal Control of a Battery Energy Storage System," in *PowerTech (POWERTECH), 2013 IEEE*, Grenoble, 2013.
- [112] J. Wang, P. Liu, J. Hicks-Garner, E. Sherman, S. Soukiazian, M. Verbrugge, H. Tataria, J. Musser, and P. Finamore, "Cycle-life model for graphite-LiFePO₄ cells," *J. Power Sources*, vol. 196, no. 8, pp. 3942–3948, Apr. 2011.
- [113] C. Zhou, K. Qian, M. Allan, and W. Zhou, "Modeling of the Cost of EV Battery Wear Due to V2G Application in Power Systems," *IEEE Trans. Energy Convers.*, vol. 26, no. 4, pp. 1041–1050, 2011.
- [114] C. Toepfer, "SAE Electric Vehicle Conductive Charge Coupler, SAE J1772," *Soc. Automot. Eng.*, 2009.
- [115] "Society of Automotive Engineers: Vehicle Electrification Standards." [Online]. Available: <http://www.sae.org/standardsdev/vehicleelectrification.htm>. [Accessed: 01-Oct-2013].
- [116] D. C. Erb, O. C. Onar, and A. Khaligh, "Bi-directional charging topologies for plug-in hybrid electric vehicles," in *2010 Twenty-Fifth Annual IEEE Applied Power Electronics Conference and Exposition (APEC)*, 2010, pp. 2066–2072.
- [117] B. Bilgin, A. Emadi, and M. Krishnamurthy, "Design considerations for a universal input battery charger circuit for PHEV applications," in *2010 IEEE International Symposium on Industrial Electronics (ISIE)*, 2010, pp. 3407–3412.

- [118] A. Shafiei and S. S. Williamson, "Plug-in hybrid electric vehicle charging: Current issues and future challenges," in *2010 IEEE Vehicle Power and Propulsion Conference (VPPC)*, 2010, pp. 1–8.
- [119] M. Yilmaz and P. T. Krein, "Review of battery charger topologies, charging power levels, and infrastructure for plug-in electric and hybrid vehicles," *Power Electron. IEEE Trans. On*, vol. 28, no. 5, pp. 2151–2169, 2013.
- [120] O. Sundstrom and C. Binding, "Flexible charging optimization for electric vehicles considering distribution grid constraints," *Smart Grid IEEE Trans. On*, vol. 3, no. 1, pp. 26–37, 2012.
- [121] E. Sortomme and M. A. El-Sharkawi, "Optimal Power Flow for a System of Microgrids with Controllable Loads and Battery Storage," in *Power Systems Conference and Exposition, 2009. PSCE '09. IEEE/PES*, 2009, pp. 1–5.
- [122] M. Singh, I. Kar, and P. Kumar, "Influence of EV on grid power quality and optimizing the charging schedule to mitigate voltage imbalance and reduce power loss," in *Power Electronics and Motion Control Conference (EPE/PEMC), 2010 14th International*, 2010, pp. T2–196.
- [123] R. Freire, J. Delgado, J. M. Santos, and A. T. De Almeida, "Integration of renewable energy generation with EV charging strategies to optimize grid load balancing," in *Intelligent Transportation Systems (ITSC), 2010 13th International IEEE Conference on*, 2010, pp. 392–396.
- [124] R. J. Bessa, M. A. Matos, F. J. Soares, and J. A. P. Lopes, "Optimized bidding of a EV aggregation agent in the electricity market," *Smart Grid IEEE Trans. On*, vol. 3, no. 1, pp. 443–452, 2012.
- [125] S. Bashash, S. J. Moura, J. C. Forman, and H. K. Fathy, "Plug-in hybrid electric vehicle charge pattern optimization for energy cost and battery longevity," *J. Power Sources*, vol. 196, no. 1, pp. 541–549, Jan. 2011.
- [126] S. Han, S. Han, and H. Aki, "A practical battery wear model for electric vehicle charging applications," *Appl. Energy*, vol. 113, pp. 1100–1108, Jan. 2014.
- [127] L. Lam and P. Bauer, "Practical Capacity Fading Model for Li-Ion Battery Cells in Electric Vehicles," *IEEE Trans. Power Electron.*, vol. 28, no. 12, pp. 5910–5918, 2013.
- [128] K. Smith, M. Earleywine, E. Wood, and A. Pesaran, "Battery Wear from Disparate Duty-Cycles: Opportunities for Electric-Drive Vehicle Battery Health Management," in *American Control Conference 2012*, 2012.
- [129] K. Smith, M. Earleywine, E. Wood, J. Neubauer, and A. Pesaran, "Comparison of plug-in hybrid electric vehicle battery life across geographies and drive cycles," in *SAE Technical Paper*, 2012.
- [130] T. Markel, K. Smith, and A. A. Pesaran, "Improving petroleum displacement potential of PHEVs using enhanced charging scenarios," *Electr. Hybrid Veh. Power Sources Models Sustain. Infrastruct. Mark.*, 2009.
- [131] Kandler Smith, "Battery Life Trade-Off Studies." NREL Fiscal Year 2010 Annual Progress Report, 2010.
- [132] A. A. Pesaran, T. Markel, H. S. Tataria, and D. Howell, "Battery Requirements for Plug-in Hybrid Electric Vehicles—analysis and Rationale," in *EVS-23 International Electric Vehicle Symposium*, Anaheim, CA, 2007.
- [133] J. R. Belt, "Battery Test Manual for Plug-In Hybrid Electric Vehicles," Idaho National Laboratory, INL/EXT-07-12536, Dec. 2010.

- [134] J. Hall, A. Schoen, P. Allen, P. Liu, and K. Kirby, "Resistance Growth in Lithium Ion Satellite Cells. I. Non Destructive Data Analyses," in *Meeting Abstracts*, Los Angeles, CA, 2005, vol. MA2005-02, pp. 242–242.
- [135] Steven L. Clark, "Optimization of Battery Thermal Management, and Impact on Life," presented at the EV Battery Tech USA, Troy, Michigan, 22-Sep-2010.
- [136] C. Rosenkranz, "Deep-Cycle Batteries for Plug-In Hybrid Application," in *EVS-20 International Electric Vehicle Symposium and Exhibition*, Long Beach, CA, 2003.
- [137] V. Marano, S. Onori, Y. Guezennec, G. Rizzoni, and N. Madella, "Lithium-ion batteries life estimation for plug-in hybrid electric vehicles," in *IEEE Vehicle Power and Propulsion Conference, 2009. VPPC '09*, 2009, pp. 536–543.
- [138] A. Hoke, A. Brissette, D. Maksimovic, D. Kelly, D. Boundy, and A. Pratt, "Maximizing lithium ion vehicle battery life through optimized partial charging," in *Innovative Smart Grid Technologies (ISGT), 2013 IEEE PES*, 2013, pp. 1–5.
- [139] Shiraz Saleem, Annabelle Pratt, Rana Pratap, and Somnath Shahapurkar, "Technology and analytics for local and autonomous control of residential heating, ventilation, and air-conditioning (HVAC)," *Intel Technol. J.*, vol. 16, no. 1, 2012.
- [140] X. Fang, D. Yang, and G. Xue, "Evolving Smart Grid Information Management Cloudward: A Cloud Optimization Perspective," *IEEE Trans. Smart Grid*, vol. 4, no. 1, pp. 111–119, Mar. 2013.
- [141] S. S. Choi and H. S. Lim, "Factors that affect cycle-life and possible degradation mechanisms of a Li-ion cell based on LiCoO₂," *J. Power Sources*, vol. 111, no. 1, pp. 130–136, Sep. 2002.
- [142] "Dow Jones Hourly Mid-Columbia Prices." Dow Jones Transaction Based Indices, Jul-2011.
- [143] F. Lu, L. Shang, D. Maksimovic, and Q. Lv, "A large-scale study of PHEV charging," in *Power System Technology (POWERCON), 2012 IEEE International Conference on*, 2012, pp. 1–6.
- [144] A. Hoke, K. Bennion, V. Gevorgian, S. Chakraborty, and E. Muljadi, "Sizing SiC storage inverters for fast grid frequency support," in *2015 IEEE 3rd Workshop on Wide Bandgap Power Devices and Applications (WiPDA)*, 2015, pp. 328–333.